14

Observations of Mercury's Exosphere: Composition and Structure

WILLIAM E. MCCLINTOCK, TIMOTHY A. CASSIDY, AIMEE W. MERKEL, ROSEMARY M. KILLEN, MATTHEW H. BURGER, AND RONALD J. VERVACK, JR.

14.1 INTRODUCTION

Mercury is surrounded by a tenuous exosphere in which particles travel on ballistic trajectories under the influence of a combination of gravity and solar radiation pressure. The densities are so small that the surface forms the exobase and particles in the exosphere are more likely to collide with it rather than with each other. For a planet with a more substantial collision-dominated atmosphere, a population of particles that enters from below the exobase supplies the exosphere. In contrast, Mercury's exosphere is supplied both by incoming sources, including the solar wind (hydrogen and helium), micrometeoroids (dust) and meteoroids, and comets and by particles released from the surface through a variety of processes that include sputtering by solar wind ions, desorption by solar photons and electrons, impacts by micrometeoroids, and thermal desorption of surface materials. These source processes are balanced by loss processes, which include impact with and sticking to the surface, Jeans (or thermal) escape, ionization followed by transport along magnetic field lines, and acceleration by solar radiation pressure to escape velocity.

Ground-based attempts to detect an atmosphere around Mercury before Mariner 10 first visited the planet in 1974 were unsuccessful and led only to increasingly tight upper limits, culminating in a limiting value for surface atmospheric pressure of 0.015 Pascal (Pa) determined by Fink et al. (1974).

During the three flybys of Mercury by Mariner 10 between March 1974 and March 1975, the spacecraft's Ultraviolet Spectrometer made robust measurements of hydrogen and helium and made a tentative detection of oxygen that was described as "unconfirmed" (Broadfoot et al., 1976). These observations were followed a decade later by discoveries with Earth-based telescopes of exospheric sodium and potassium (Potter and Morgan, 1985, 1986). Subsequently, Bida et al. (2000) reported the discovery of exospheric calcium from observations with the High Resolution Echelle Spectrometer (HIRES) at the Keck I telescope.

During the three flybys of Mercury by the MESSENGER spacecraft, measurements by the Mercury Atmospheric and Surface Composition Spectrometer (MASCS) instrument (McClintock and Lankton, 2007) yielded detections of exospheric magnesium (McClintock et al., 2009) and ionized calcium (Vervack et al., 2010). Other exospheric species have been reported from both ground-based observers and

additional MESSENGER measurements. Doressoundiram et al. (2009) made a provisional detection of aluminum. Bida and Killen (2016) reported measurements of aluminum and iron (three-standard-deviation detections). Most recently, Vervack et al. (2016) reported the discovery of manganese and definitive measurements of aluminum and ionized calcium from MASCS data. Thus, the total inventory of confirmed exospheric neutral species now includes H, He, Na, K, Ca, Mg, Al, Fe, and Mn.

Since its discovery in 1985, sodium has been the most studied species from both ground-based observatories and from space. As described in Section 14.3.2, several groups have imaged emission from the sodium exosphere around the planet and in an extended anti-sunward tail (Potter et al., 2002a; Baumgardner et al., 2008). These studies provide insight into the behavior of the sodium exosphere on timescales as short as a few hours (e.g., Leblanc et al., 2009). Schleicher et al. (2004) and Potter et al. (2013) also observed sodium in absorption against the Sun during Mercury solar transits. These observations are complementary to those made by MESSENGER from orbit around the planet that characterized the seasonal and annual behavior of the sodium exosphere (Cassidy et al., 2015, 2016).

Potassium has also been observed from the ground by a number of researchers (Potter et al., 2002a; Doressoundiram et al., 2010; Killen et al., 2010). Calcium is much less studied from the ground than sodium or potassium, with only one group having reported observations (Bida et al., 2000). Emissions from hydrogen, helium, and magnesium occur at ultraviolet wavelengths that are absorbed by the Earth's atmosphere, so only space-based instruments can observe these constituents.

This chapter summarizes both ground-based and space-based observations that have been made of Mercury's exosphere, from its initial discovery by Mariner 10 through the MESSENGER mission, focusing on work published after the pre-MESSENGER reviews by Killen et al. (2007) and Domingue et al. (2007). In order to place the observations in context, the chapter begins with a brief summary of Chamberlain's theory of exospheres, which provides a framework for discussing the observations. That introduction is followed by a description of the techniques that various researchers have employed to observe Mercury's exosphere and then by a detailed discussion of the results for each of the known species. Models of source and loss processes derived from the MESSENGER observations are discussed in Chapter 15.

14.2 CHAMBERLAIN'S THEORY

The theory of exospheres developed by Chamberlain (1963) is often used to describe the composition and temperature of Mercury's exosphere. Chamberlain's formulation begins with the assumption that the collisonless exosphere is supplied from the lower collisional atmosphere through a boundary layer, termed the exobase, by gas that has a Maxwellian velocity distribution at a single temperature. In contrast, Mercury's surface is the lower boundary of its exosphere, which is populated by many components with different velocity distributions. Surface sticking, ionization followed by transport along magnetic field lines, Jeans escape, and acceleration by solar radiation pressure are known to deplete Mercury's exosphere, whereas the only loss process in Chamberlain's original formulation was Jeans escape. Solar radiation pressure was later added by Bishop and Chamberlain (1989) to extend the general formulation. Although a Chamberlain exosphere is spherically symmetric and Mercury's actual exosphere does not have such symmetry, a Chamberlain model nonetheless provides a simple, analytic description that is routinely used to provide insight into the exospheric processes at work on Mercury.

A classical Chamberlain exosphere contains three populations of particles: those that travel on ballistic orbits that reenter the atmosphere through the exobase, those that are in quasi-trapped satellite orbits, and those that are escaping. Because there is no atmospheric reservoir below its exobase, a surface-bounded exosphere such as Mercury's has only the ballistic and escaping components, and its density, n, as a function of the radial distance from the center of the planet, r, is approximated by

$$n = \zeta n_0 e^{-(U-U_0)/kT}, \tag{14.1}$$

$$U = -GMm/r. \tag{14.2}$$

In equations (14.1) and (14.2), n_0 is the surface density, U is the gravitational potential energy of a particle of mass m, U_0 is the potential energy at the surface, k is Boltzmann's constant, T is the absolute temperature, G is the gravitational constant, and M is the mass of Mercury. The factor ζ (Chamberlain, 1963) accounts for the fraction of the initial isotropic Maxwellian distribution that is actually present at a given altitude. A value of $\zeta = 1$, which is appropriate for a cool gas deep within a gravitational well (Chamberlain and Hunten, 1987), is an appropriate assumption for particles that are on ballistic orbits that intersect the exobase (or the surface, in the case of Mercury). This approximation begins to fail, however, as particles reach escape energy.

Equations (14.1) and (14.2) are valid for an exosphere in which only gravity acts on the particles. However, some atoms in Mercury's exosphere are accelerated by non-negligible solar radiation pressure. When an atom absorbs a photon, it is accelerated in the direction of the photon because photons possess both energy and momentum. An atom that emits a photon is also accelerated, but in a direction opposite to that of the emitted photon. Because sunlight incident on Mercury's exosphere is nearly unidirectional, and reemission is nearly isotropic, the effect of many absorption–emission events is a net anti-sunward acceleration. This effect can be included in the model by modifying U to include a combination of both gravity and radiation pressure (Bishop and Chamberlain, 1989):

$$U = -GMm/r + mbr \cos \theta. \tag{14.3}$$

Here b is the net acceleration by photon pressure, and θ is the solar zenith angle (the angle between the Mercury–Sun line and the local radius vector from the planet center).

14.3 OBSERVATIONAL TECHNIQUES

Although the Fast Imaging Plasma Spectrometer (FIPS) component of the Energetic Particle and Plasma Spectrometer instrument on the MESSENGER spacecraft (Andrews et al., 2007) measured concentrations of sodium and oxygen ions around Mercury in situ (Raines et al., 2013), the neutral exosphere has been studied from Earth and space only with telescopes, either to sense remotely the intensity of sunlight resonantly scattered by its constituents or to observe sunlight absorbed by the exosphere as the planet passes in front of the Sun during a transit.

14.3.1 Remote Sensing Observations

Resonant scattering occurs when an atom (or molecule) in its lowest energy state absorbs a photon and transitions to an excited state. The atom promptly returns to the ground state by emitting a photon of equal energy. In the case of solar radiation that is resonantly scattered in an exosphere in which densities are vanishingly small, most of the photons that are absorbed are removed from the incident beam and are reemitted isotropically. Small asymmetries that arise for some transitions (Chamberlain, 1961) are usually neglected. For an optically thin medium, the resonantly scattered radiance (the term "emission" is used interchangeably in this Chapter), I, measured in photons cm^{-2} steradian^{-1} s^{-1}, is related to the total number of emitters along a line of sight by

$$4\pi I = gN. \tag{14.4}$$

In equation (14.4), g (often referred to as the g-value) is the photon scattering coefficient in photons atom^{-1} s^{-1}, and N is the line-of-sight column density in atoms cm^{-2} (Hunten et al., 1956). The value of g is proportional to the absorption cross section of the atomic transition in cm^2 and to the solar irradiance incident on the exosphere at the rest wavelength of the transition in photons cm^{-2} s^{-1}. Atmospheric scientists often express radiance in rayleighs, where 1 rayleigh (R) is 10^6 photons emitted into 4π steradians in 1 s:

$$4\pi R = gN/10^6. \tag{14.5}$$

Solar radiation reflected from the planet's surface also illuminates the exosphere, but its contribution to the observed exospheric intensity is small and is usually neglected except for the case of multiple scattering (Killen, 2006). In principle, electron-impact excitation can also contribute to the observed emission,
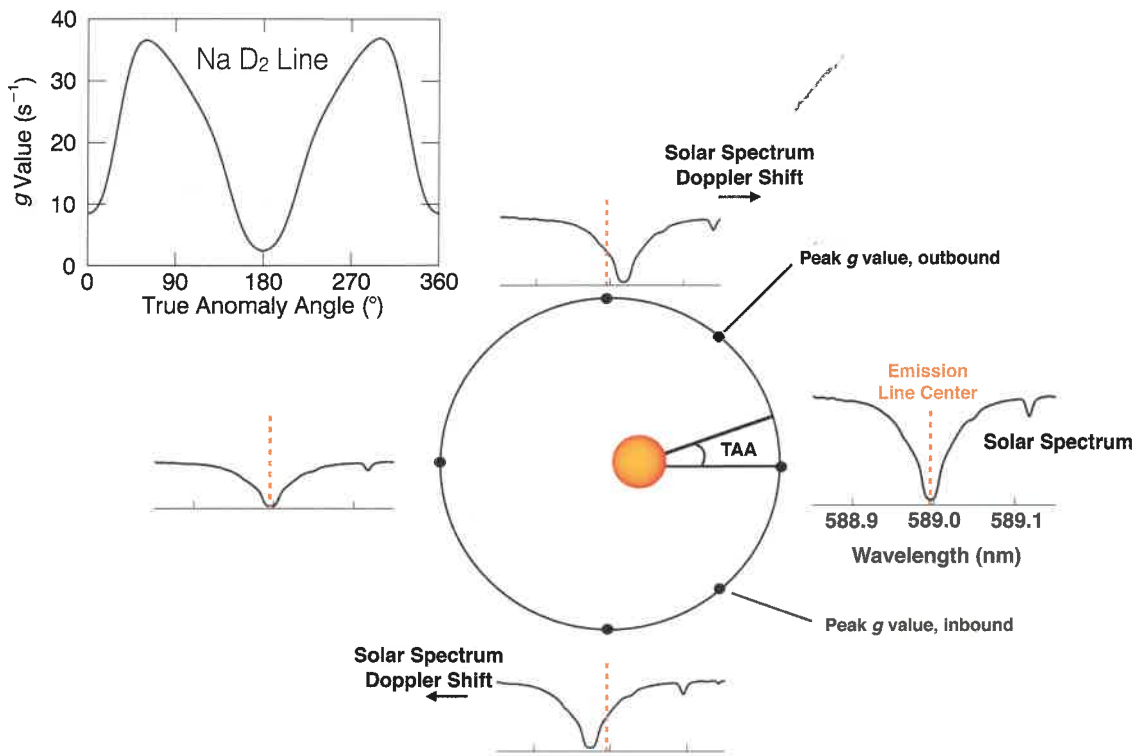
Figure 14.1. Mercury's distance from the Sun traces out an ellipse (central figure) when plotted as a function of true anomaly angle (TAA), the counterclockwise angular distance from perihelion when viewed from the Sun's north celestial pole. The solar spectrum around the sodium D_2 resonance transition is shown at the right. It exhibits a deep photospheric absorption feature (Fraunhofer line) near the center (rest wavelength) of the transition (dashed yellow line). This spectrum impinges upon atoms in Mercury's exosphere at perihelion, where the heliocentric radial velocity of the planet is zero. As Mercury orbits the Sun on the outbound leg of its orbit, its radial component of velocity begins to increase, causing the solar spectrum to shift to longer wavelengths. The shift reaches a maximum near TAA = 90° and then declines to zero at aphelion. On the inbound leg of Mercury's orbit the solar spectrum is shifted to shorter wavelengths, reaching a maximum shift near TAA = 270°. In addition to being Doppler-shifted, the magnitude of the solar irradiance varies with distance from the Sun, such that the magnitude of the solar irradiance at periapsis is a factor of 2.3 greater than that at apoapsis. The variation in g-value as a function of TAA, which is shown in the upper left panel, results from both changing Doppler shift and changing solar distance.

but the electron density in Mercury's magnetosphere is too low for it to be significant. Chamberlain (1963) described a variety of approximations for integrating densities in equation (14.1) along a line of sight to obtain values of N, although in practice this integral can be performed numerically.

Owing to the eccentricity of the planet's orbit, the heliocentric radial velocity of the planet varies up to ± 10 km s^{-1} during a Mercury year, causing the solar spectrum to be Doppler shifted relative to the exosphere. This shift results in substantial variation in g-values, because the solar spectrum in the vicinity of resonance transitions of important exospheric species is modulated by the presence of absorption features, known as Fraunhofer lines, that form in the Sun's relatively cool photosphere. This effect is illustrated in Figure 14.1 for one of the resonance lines of sodium (D_2, see Section 14.3.2), which has a rest wavelength of 588.995 nm in air. Changes in g-value cause the observed sodium intensity emitted by the exosphere to vary with an annual cycle, brighter near Mercury true anomaly angles (TAA) 65° and 295° but fainter near TAA = 0° and TAA = 180°. Larger g-values also lead to larger average radiation forces, so that atoms are more strongly accelerated anti-sunward near TAA = 65° and TAA = 295° than at other times during the Mercury year. The g-value, which depends linearly on the incident solar irradiance, is also modulated by Mercury's changing distance from the Sun.

When a planet passes between the Sun and Earth, atmospheric constituents above its limb scatter the solar radiation away from its original path, creating an absorption feature in the solar spectrum. The area of an absorption feature is related to the line-of-sight column density by

$$wE_{\text{Sun}} = gN, \tag{14.6}$$

where w is the equivalent width of the absorption feature measured in nm and E_{Sun} is the solar irradiance at the wavelength of the feature, measured in photons cm^{-2} nm^{-1} s^{-1} (Potter et al., 2013). The "equivalent width" is the width the absorption feature would have if it were completely absorbing.

14.3.2 Ground-Based Techniques

Most ground-based observers employ high-resolution spectrographs to measure Mercury's spectrum. High resolution is necessary to remove backgrounds from the exospheric signal that arise from sunlight reflected by the surface of the planet and from sunlight scattered by Earth's atmosphere. The right half of
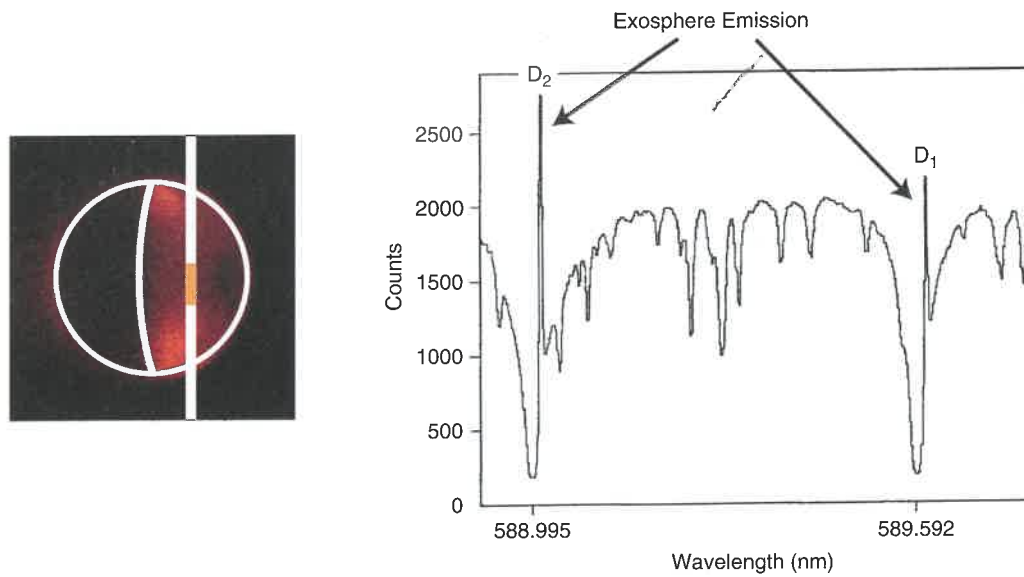
Figure 14.2. Ground-based observers employ telescopes equipped with high-resolution spectrographs to separate exosphere emission from sunlight reflected from Mercury's surface. As shown here, the telescope images the planet onto the spectrograph entrance slit (left). The spectrograph disperses the light into a spectral-spatial image that is projected onto a two-dimensional detector in which the spectrum on each row originates from a unique location along the slit. (As an illustration, the spectrum on the right originates from the center of the orange band along the slit). Exosphere sodium emission appears at narrow peaks above the continuous reflected spectrum and is extracted from each row to construct a slice of the full disk image. The entire image is built up by slewing the telescope to scan the slit across the disk. In a second approach, a telescope is used to image the planet onto the input of an image slicer. The slicer reformats the two-dimensional image and projects it onto the entrance slit of a spectrograph as a one-dimensional line image. This technique produces an image without the need to slew the telescope.

Figure 14.2 illustrates a typical high-resolution spectrum (Sprague et al., 1997) of the surface exosphere that covers wavelengths near the resonance lines of sodium, which are located at air wavelengths of 588.995 nm and 589.592 nm and are historically referred to as D_2 and D_1, respectively. At a resolving power of $\lambda/\Delta\lambda \sim 160,000$, where λ is wavelength and $\Delta\lambda$ is the spectral resolution, the exospheric components are clearly evident as a pair of discrete, narrow peaks superimposed on the broad, continuous light reflected from the surface. Equation (14.4) relates the emission in these peaks to the total column density, in atoms cm^{-2}, along the line of sight from the observer to the planet's surface.

Two approaches are commonly used to produce images from high-resolution spectra. In the first, as illustrated in Figure 14.2, the telescope images Mercury directly onto the entrance slit of the spectrograph, and the resulting spectra are analyzed to extract the exosphere intensities along the slit. A two-dimensional image is built up by slewing the telescope to move the target image across the slit in a series of discrete steps and recording a line image at each step. This process is sometimes referred to as "push-broom" imaging. The second employs an optical image slicer (Pierce, 1965). In this approach, the telescope forms an image of Mercury on the slicer, which rearranges the image to fit in the narrow entrance slit of an imaging spectrograph. As a result, two-dimensional areas much wider than the slit can be observed instantaneously. The advantage of this approach is that spectra from multiple points over most (or in some cases all) of Mercury's disk can be obtained simultaneously and without the need to stitch multiple line images together (e.g., Potter and Morgan, 1990). Fiber optic bundles can also be used instead of image slicers to rearrange a two-dimensional target image and project it

onto the slit of an imaging spectrograph (Doressoundiram et al., 2010). Typical integration times required to obtain a high-quality image are instrument dependent and are in the range of several minutes to an hour (e.g., Leblanc et al., 2009).

Two additional techniques have been used to study Mercury's exosphere from Earth. First, a small telescope equipped with a narrow interference filter and an occulting disk that blocks the direct image of the planet's surface has been used to measure resonantly scattered sunlight from sodium atoms that are sufficiently far from the planet that reflected sunlight from the disk is negligible (Baumgardner et al., 2008; Schmidt et al., 2012). Second, two groups (Schleicher et al., 2004; Potter et al., 2013) have used telescopes equipped with high-spectral-resolution Fabry–Perot interferometers to measure the absorption of sunlight by sodium atoms in Mercury's exosphere during solar transit. During these observations Mercury appears as a dark disk superimposed on the image of the Sun. Whereas the disk of the planet completely blocks sunlight, sodium in the exosphere surrounding the disk only partly absorbs it. Rather than appearing as excess emission superimposed on a solar continuum, these spectra exhibit excess absorption in the nominal solar photospheric profile resulting from the partial extinction of sunlight passing through the exosphere.

14.3.3 Space-Based Techniques

Two spacecraft equipped with small telescope spectrometers have visited Mercury. These were Mariner 10 with its Ultraviolet Spectrometer (UVS) (Broadfoot et al., 1974 and 1976) and MESSENGER with its MASCS Ultraviolet and
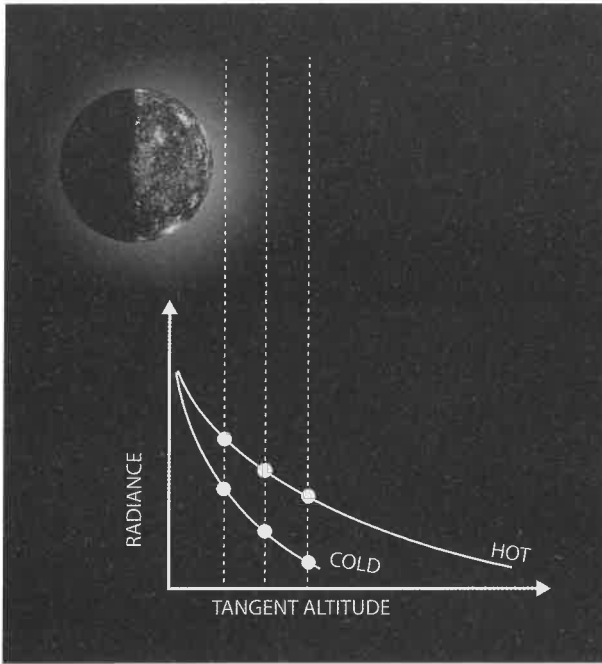
Figure 14.3. Small telescope spectrometers on spacecraft near Mercury use limb-scan viewing to study the exosphere. In this approach, the telescope images the exosphere, which is shown as a faint gray glow surrounding the planet, onto the spectrometer entrance in order to view lines of sight that are tangent to the limb of the planet. Different lines of sight probe different altitudes, enabling the measurement of exospheric column density as a function of altitude. The slope of the radiance profile is indicative of its temperature, with a warmer exosphere producing a shallower slope.

Visible Spectrometer (UVVS) (McClintock and Lankton, 2007). The spectral passbands of these instruments were approximately 0.5–1 nm. This bandwidth was too large for these instruments to detect the exosphere while viewing the sunlit surface of the planet because the intensity of continuous reflected sunlight integrated over a ~1 nm passband is much larger than that of exospheric emission lines, which have full widths that are typically 0.005 nm or less. Instead they relied on limb-scan viewing, in which a telescope views the exosphere with the entrance slit of a spectrograph along a line of sight that passes above the surface at a given altitude. Figure 14.3 illustrates the technique for two exospheres with identical surface densities at two different temperatures. These are sampled along three lines of sight through Mercury's exosphere. For each line of sight, there is a vector from the center of the planet that is perpendicular to it. The point at which that vector intersects the surface is referred to as the tangent point, and the distance from the surface to the line of sight along that vector is referred to as the minimum ray height or tangent altitude. Limb emission profiles, which are plots of radiance versus tangent altitude, are assembled from the line-of-sight radiances. (The terms limb scan and limb profile are often used interchangeably. In this chapter, we use "limb scan" to identify the observation – the motion of the telescope field of view – and "limb profile" to identify the measured geophysical quantity as a function of tangent altitude.)
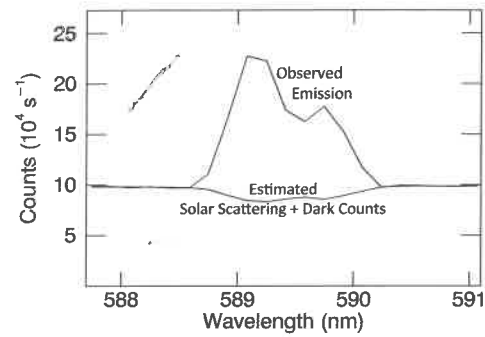

Figure 14.4. A sodium emission spectrum observed at 100 km tangent altitude near the subsolar point by the MESSENGER UVVS, which had a spectral resolution of ~0.6 nm. The graph shows the total observed counts per second recorded by one of the instrument's photomultiplier tubes as a function of wavelength. The background due to the combination of sunlight reflected from the surface and scattered into the telescope and detector dark counts is subtracted to extract the exospheric D_1 and D_2 emission lines at 589.0 and 589.6 nm, respectively. These lines appear as two broad profiles that have an approximate 2:1 intensity ratio.

Equation (14.4) relates the spectrograph signal to the total column density, in atoms cm^{-2}, along the line of sight from the observer through the exosphere. If a Chamberlain exosphere is assumed, the vertical column density, N, is related to the exosphere density at the tangent point, n_h, and the distance from the center of the planet, r, by

$$N = n_h \sqrt{2\pi r/H},\tag{14.7}$$

$$H = n \Big/ \left(\frac{dn}{dr}\right) = kT/(GMm/r^2 + mb\cos\theta),\tag{14.8}$$

where H is the scale height, or the e-folding distance, and is defined as the ratio of density to the rate of density change at altitude h. Although an exosphere is not hydrostatic, the definition of H for an exosphere with $b = 0$ is analogous to that for a plane-parallel hydrostatic atmosphere in which H is the kinetic energy of a particle divided by the gravitational force acting on it.

Space-based observations provide altitude information that is not available from Earth, because they do not include backgrounds caused by light from the bright atmosphere above the illuminated disk that is scattered along the slit by the telescope and spectrograph optics. A typical dayside sodium spectrum acquired by the MESSENGER UVVS is shown in Figure 14.4. It covers the same emission lines as those shown in Figure 14.2 but at much lower spectral resolution. The total emission (measured in either R or kR) is obtained by subtracting the estimated background (dark counts and surface reflectance), integrating the resulting signal, and multiplying by a laboratory-measured calibration factor (McClintock and Lankton, 2007). The removal of surface-reflected sunlight from the MESSENGER calcium and magnesium emissions, which are less intense than those from sodium, was described by Burger et al. (2010) and Merkel et al. (2017), respectively.

14.3.3.1 Flyby Observations

Both the Mariner 10 UVS and the MESSENGER UVVS observed Mercury's exosphere during flybys of the planet. The
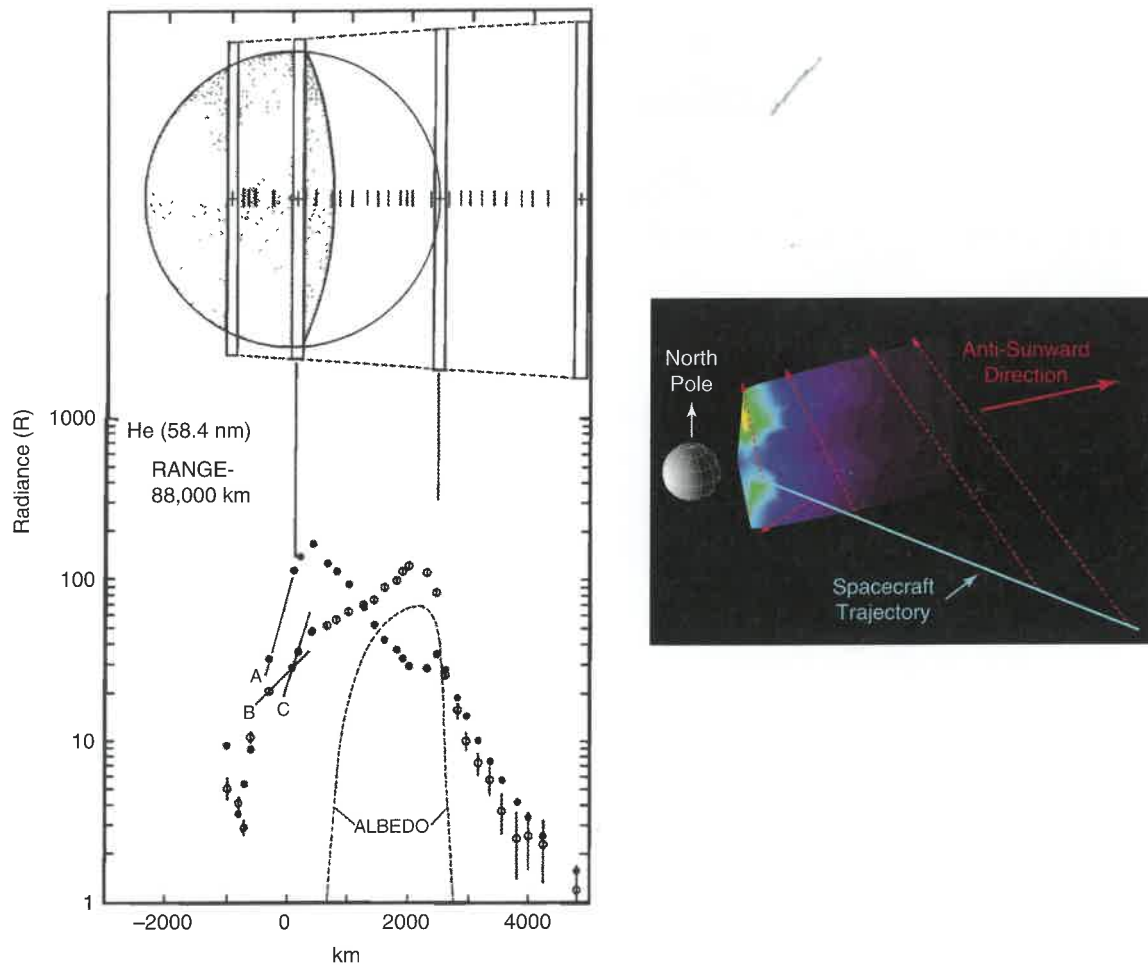
Figure 14.5. (Left) The Mariner 10 UVS observing geometry and a profile of helium (58.4 nm) emission versus altitude obtained at a distance of 88,000 km, during the third encounter of the spacecraft with the planet on 16 March 1975. Open circles with vertical errors represent the observed radiance, which includes emission from the exosphere and reflection from the surface (albedo). Filled circles are radiance computed from a model. Lines labeled A and C illustrate model scale heights at their respective locations. The line labeled B represents the observed scale height at its location. There are significant differences in both emission and scale height between the observations and the model. Adapted from Broadfoot et al. (1976). (Right) The UVVS observation geometry and a reconstructed image of emission from the sodium resonance lines during the first MESSENGER flyby (M1) on 14 January 2008. Adapted from McClintock et al. (2008).

left panel of Figure 14.5 illustrates the Mariner 10 UVS observing geometry and an altitude profile for the helium 58.4 nm line obtained at a distance of 88,000 km during the third encounter of the spacecraft with the planet on 16 March 1975. These observations were made by pointing the spacecraft and allowing the UVS field of view to drift across the disk and into the exosphere. In this measurement the spacecraft was oriented so that the spectrograph slit was projected north–south and swept out the entire disk as the spacecraft flew sunward past the planet. The UVS had no spatial resolution in the north–south direction, and the one-dimensional profiles were produced by summing the signal from all the light entering the spectrometer slit. From these observations and Monte Carlo models, Broadfoot et al. (1976) derived surface densities and altitude distributions for hydrogen and helium. They reported an upper limit for oxygen emission as well as upper limits on selected molecular species derived from a solar occultation experiment. Their results are discussed in further detail in Section 14.4.4.

The MESSENGER encounters were much closer to the planet than those executed by Mariner 10. The right panel in Figure 14.5 illustrates the UVVS observation geometry during the first MESSENGER flyby (M1), which took place on 14 January 2008. As the spacecraft approached the planet from its anti-sunward dusk side, it oriented the UVVS slit approximately perpendicular to the Sun–Mercury line and executed a series of partial roll maneuvers that swept the slit north–south during approach. This geometry enabled the UVVS to construct images of the sodium radiances behind the planet. Similar tail observations were executed in order to construct images of sodium, calcium, and magnesium during the second and third flybys (M2 and M3), which occurred on 6 October 2008 and 29 September 2009, respectively (e.g., Vervack et al., 2010).

As the spacecraft entered the shadow of Mercury near closest approach to the planet during M1, it executed a 180° roll (the so-called "fantail" observations) that swept the UVVS line-of-sight from dawnward to north to duskward before
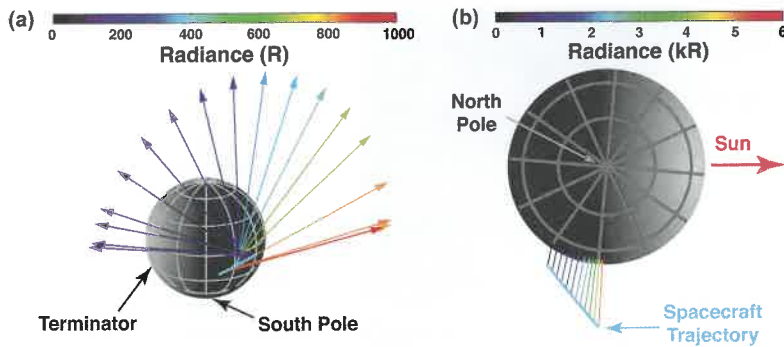
Figure 14.6. Viewing geometry and observed radiances from calcium: (a) near-tail and (b) near-terminator observations during MESSENGER's first flyby. In (a), UVVS line-of-sight vectors are color coded according to the observed radiances. In (b), line-of-sight vectors are seen as the spacecraft emerges from Mercury's shadow. The observed radiances here correspond to columns of illuminated calcium atoms between MESSENGER and Mercury's surface. Adapted from McClintock et al. (2008).
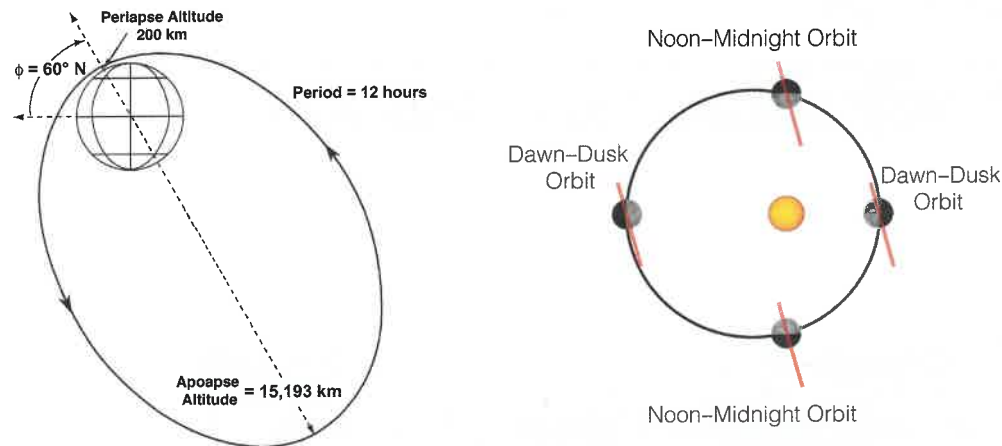

Figure 14.7. (Left) MESSENGER's initial 12-h orbit about Mercury. Most UVVS observations of the exosphere occurred near apoapsis when the instrument had the widest coverage in local time. (Right) The orbit plane of MESSENGER through one Mercury year. "Dawn–dusk" and "noon–midnight" refer to times when the MESSENGER orbit was more or less aligned with the terminator and Sun–Mercury lines, respectively. This varying orientation placed restrictions on the spacecraft attitude that limited local time coverage, particularly near TAA = 0° (perihelion) and TAA = 180° (aphelion), where observations were possible only near dawn and dusk.

exiting on the dawn side, as illustrated in Figure 14.6a. As MESSENGER emerged from shadow, the UVVS pointed toward the surface, measuring emission over the pre-dawn and dawn terminator regions (Figure 14.6b). The UVVS obtained similar observations during M2. During M3 the initial line-of-sight was pointed south, and the spacecraft rolled it through dawn toward north as part of a planned 270° maneuver. However, the spacecraft entered safe mode midway through the flyby, and data that would have been acquired during the last 90° were lost. Fantail observations were performed very infrequently during orbital operations.

14.3.3.2 Orbital Observations

MESSENGER was inserted into orbit around Mercury on 18 March 2011. The initial orbit, shown in the left panel of Figure 14.7, had a 12-h period, an inclination of 82.5°, an apoapsis of 15,200 km, and a periapsis of 200 km. After four Mercury years of operations, the MESSENGER flight team reduced apoapsis to ~10,000 km, which reduced the period to 8 h. The UVVS performed most of its exospheric observations near apoapsis, from which it could view the largest range of local times.

The right panel of Figure 14.7 shows the orientation of MESSENGER's orbital plane as a function of TAA just after orbit insertion. MESSENGER was equipped with a sunshade that shielded the spacecraft from illumination by the Sun through most of the cruise phase and the entire orbital phase of the mission, and the requirement that the normal to the sunshade's central panel remain within 12° of the Sun–Mercury line limited the local-time coverage of the dayside exosphere over the course of a Mercury year. In particular, only local times near dawn and dusk could be sampled when Mercury was near perihelion (TAA ~ 0°) and aphelion (TAA ~ 180°). During the rest of the Mercury year, covering TAA ranges 20°–160° and 225°–340°, the spacecraft could execute small scan maneuvers about axes close to the Sun–Mercury line, enabling UVVS to make observations above the dayside limb. The most complete local-time coverage was obtained when the orbit orientation aligned more or less parallel to the Sun–Mercury line near TAA 90° and 270°.

Typical viewing geometries for the two primary observation sequences executed by UVVS on a regular basis are illustrated in Figure 14.8. In the illustration the spacecraft orbital plane was close to the Sun–Mercury line, allowing UVVS to perform dayside limb scans at up to seven local times, beginning near 0600 and ending near 1800 (Figures 14.8a and 14.8b). On the nightside, the
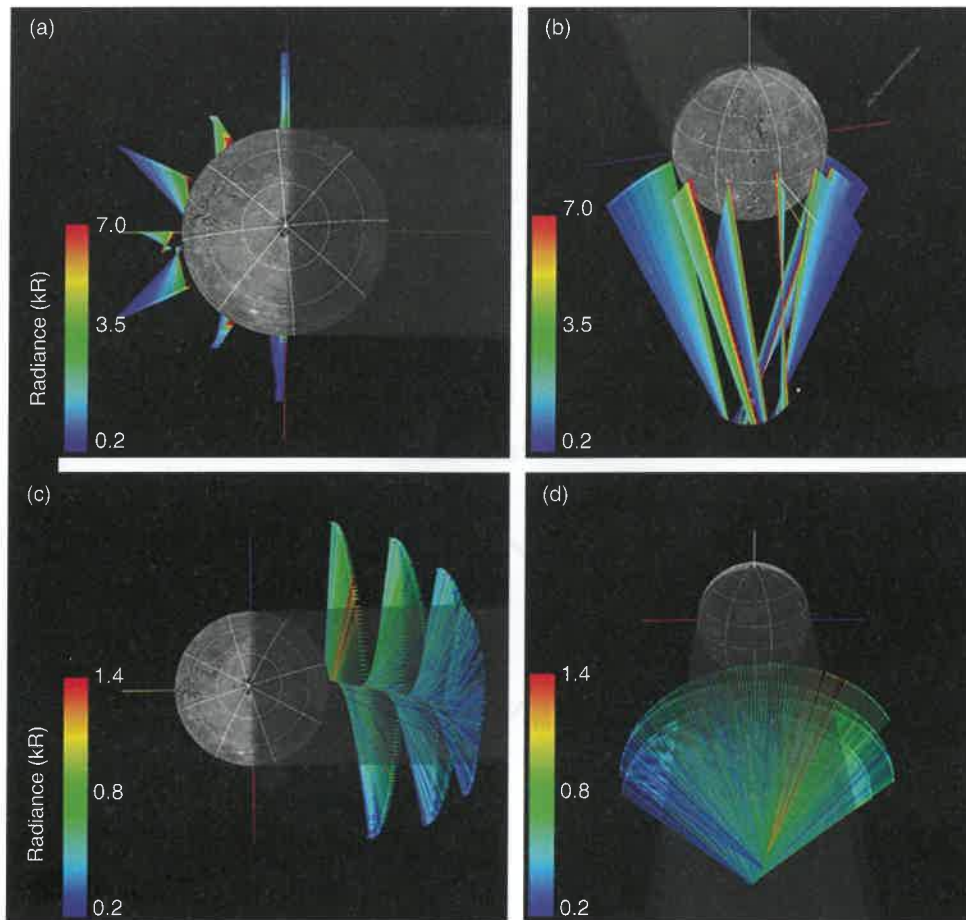
Figure 14.8. Examples of typical UVVS observing sequences used to sample the exosphere on the day and night sides of Mercury. The white, blue, red, and yellow lines radiating from the planet center represent Mercury's rotation axis, dawn and dusk terminators, and the subsolar point, respectively. In this example, the color bar represents magnesium emission in kilorayleighs, increasing linearly from blue to red. Dayside limb scans are shown (a) looking down on the north pole and (b) from a view of the dayside. Nightside tail sweeps are illustrated (c) looking down on the north pole and (d) looking toward the Sun from the nightside of the planet.
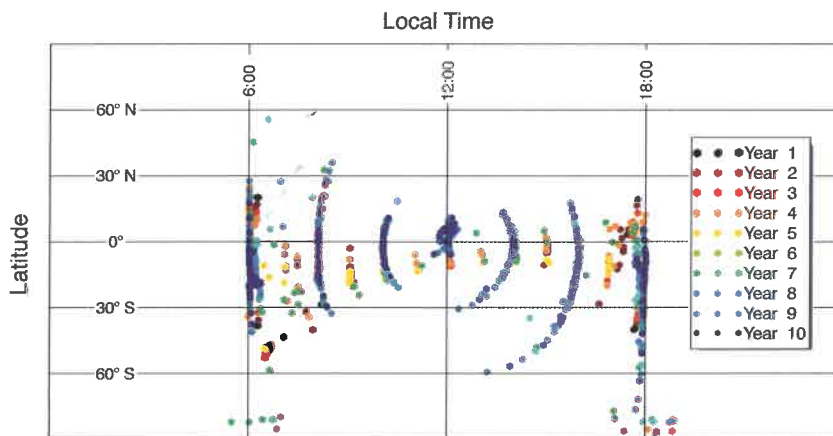

Figure 14.9. UVVS limb scan coverage. Each point indicates the local time and latitude of a limb scan's tangent point at minimum tangent altitude. Each symbol color represents a different Mercury year during MESSENGER's orbital mission. Adapted from Cassidy et al. (2015).

spacecraft executed short back-and-forth roll maneuvers (referred to as tail sweeps) to scan the field of view in the dawn–dusk direction. In this way, UVVS was able to map out the anti-sunward region of the exosphere, as shown in Figures 14.8c and 14.8d.

Although observations above the south pole were possible when the spacecraft was near TAA 0° and 180°, the tangent points of the UVVS limb scans were mostly limited to the equatorial region of Mercury, due to the combination of spacecraft orbit geometry and sunshade pointing constraints. Figure 14.9, adapted from Cassidy et al. (2015), shows the locations of the tangent points for sodium

dayside limb scans acquired during the first 10 Mercury years of the mission. No routine limb scans were made over the planet's magnetospheric cusps or above the north pole.

14.4 OBSERVATIONAL RESULTS

The known inventory of Mercury's exosphere as documented by remote observations consists of nine neutral species and one ionized species. Of these, sodium, potassium, calcium, and
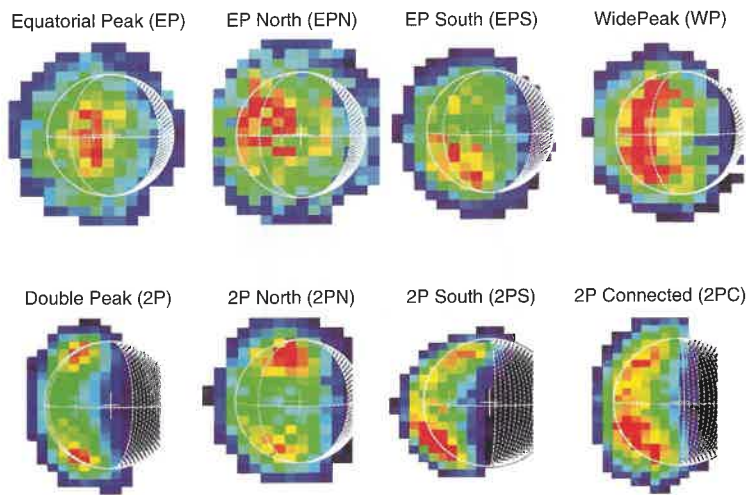
Figure 14.10. Common patterns of exospheric sodium emission seen during an extended set of images of exospheric sodium collected between 2009 and 2013 with the THEMIS telescope. Colors represent radiance on a linear rainbow scale from blue to red. Adapted from Mangano et al. (2015).

magnesium have been well studied (sodium and calcium from both the ground and space, potassium from the ground, and magnesium from space). MESSENGER observed hydrogen routinely but not systematically. Aluminum and iron have been provisionally detected from the ground on a few occasions, with three-standard-deviation upper limits reported for ionized calcium, whereas aluminum, manganese, and ionized calcium have been clearly detected by MESSENGER but over a limited range of TAA values. Only Mariner 10 observed helium, as the helium emission wavelength was outside the range of MESSENGER's instruments. MESSENGER did not confirm Mariner 10's tentative detection of oxygen, but observations of ionized oxyzen by FIPS (Raines et al., 2013) suggest that some neutral oxygen is present in the exosphere.

14.4.1 Sodium

14.4.1.1 Ground-Based Observations

Mercury's sodium exosphere was first observed by Potter and Morgan (1985), who measured the emission with a high-resolution echelle spectrograph at the McDonald Observatory. Subsequent observations have been made with a variety of techniques to measure the speed distribution, flow speed, spatial distribution, and temporal variability of the sodium exosphere. This section focuses on work published after the pre-MESSENGER literature reviews by Killen et al. (2007) and Domingue et al. (2007).

Spatial Distribution
Starting with Potter and Morgan (1990), who imaged Mercury's sodium emissions with image slicers at the McMath–Pierce Solar Telescope, a number of observers have studied the spatial distribution of sodium around Mercury. Some of the first disk-resolved observations showed high-latitude enhancements in sodium emission, leading to the hypothesis that ion bombardment at Mercury's cusps and open field lines liberates sodium atoms via a variety of processes. These include ion sputtering (McGrath et al., 1986), the ejection of neutral atoms by ion-initiated collision cascades; chemical sputtering (Potter, 1995), a chemical reaction in the regolith with incoming protons that

ejects sodium; and ion-enhanced diffusion (Killen et al., 2004; Sarantos et al., 2008), a process that aids the diffusion of sodium out of regolith grains to where other processes such as photo-desorption can eject the sodium.

Another possibility is that the high-latitude enhancements are due to an observational bias (Potter et al., 2006) that may disappear when line-of-sight effects are removed from observations (Mouawad et al., 2011). Regardless of the cause, these enhancements have been seen by many observers who used all of the methods described in Section 14.3.2. When present, the enhancement in emission is typically tens of percent greater than the emission at lower latitudes. Borland and Taylor (2007) pointed out that enhancement of this magnitude can appear more pronounced in publication figures due to the use of "rainbow" false-color scales that employ a non-linear stretch, which emphasizes small differences between values.

Mangano et al. (2015) categorized the observed emission patterns in a large data set taken by the Télescope Héliographique pour l'Etude du Magnétisme et des Instabilités Solaires (THEMIS) solar telescope with push-broom imaging by a long-slit spectrograph (Figure 14.10), as described in Section 14.3.2 and illustrated in Figure 14.2. The most common emission pattern had distinct emission peaks at high latitudes in both the northern and southern hemispheres. This is the "2P" pattern in Figure 14.10. Other common configurations included the equatorial peak ("EP"), featuring emission peaks at low latitudes near the subsolar point and several variations on the high-latitude emission pattern.

One feature of the high-latitude enhancements is their variability, documented on the timescale of days in earlier papers (Potter et al., 1999; Potter and Morgan, 1990). More recently, shorter-term (hourly) variability was reported in observations with the THEMIS telescope (Leblanc et al., 2006, 2008, 2009, 2013; Doressoundiram et al., 2010; Mangano et al., 2009, 2013, 2015). Figure 14.11a shows an example adapted from Mangano et al. (2013); from one day of observations, they reported changes in emission that they attributed to magnetospheric dynamics (Figure 14.11b). These changes were on the order of 10% at both the equator and mid-latitude cusp regions. Unlike in earlier studies of episodic variability, Mangano et al. (2013) corrected
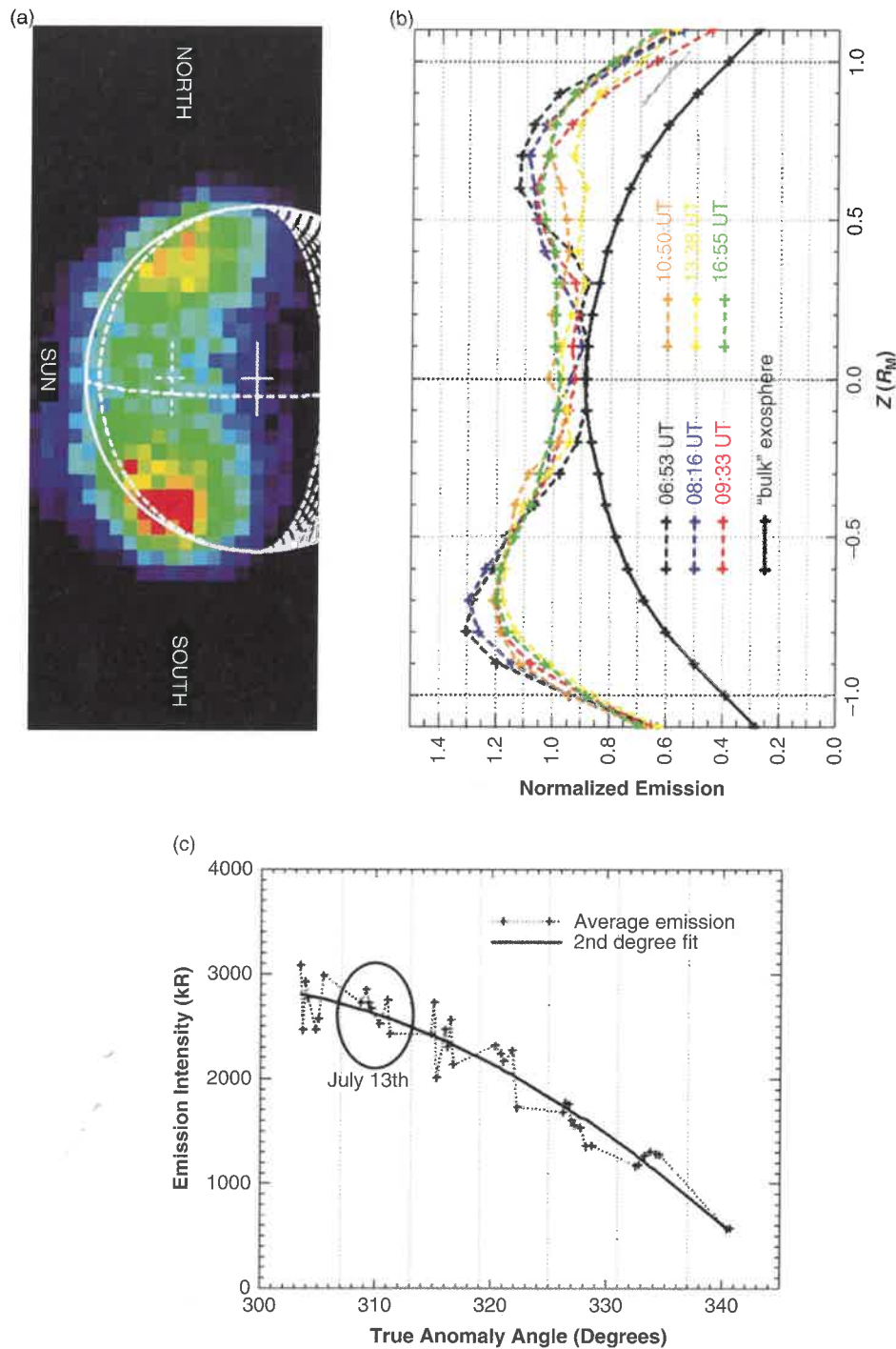
Figure 14.11. THEMIS solar telescope observations of mid-latitude enhancements in the sodium exosphere. (a) A ground-based observation of Mercury's dayside sodium exosphere. (b) Emission along the north–south axis for several observations, showing variations over the course of ~10 h. (c) Seasonal variations that were used to normalize the emissions in (b). Adapted from Mangano et al. (2013).

for longer-term seasonal changes in sodium brightnesses (Figure 14.11c) that were assumed to be independent of short-term magnetospheric activity. They did not, however, discuss the effects of atmospheric seeing and opacity, both of which can contribute to the observed variability.

Mangano et al. (2015) attempted to confirm their hypothesis that magnetospheric dynamics contribute to short-term emission variability by searching for correlations between ground-based sodium observations and interplanetary magnetic field (IMF) measurements made by MESSENGER's Magnetometer (Anderson et al., 2007). They concluded that there is a correlation between the magnitude of the IMF southward component and the presence of mid-latitude emission peaks in a subset of their observations. A southward IMF

encourages magnetic reconnection and auroral activity at Earth and so might plausibly result in higher ion fluxes to Mercury's surface (Baker et al., 2013), but the Mangano et al. (2015) conclusion is at variance with the finding from MESSENGER observations that the IMF direction is not as strong a forcer of solar wind–magnetosphere coupling as it is at Earth (DiBraccio et al., 2013).

Mangano et al. (2015) also found that southern peaks in emission were no brighter, on average, than those in the northern hemisphere. Likewise, Potter et al. (2006) applied a statistical test to show that excess emission is equally likely to be observed in the northern or southern hemisphere. This lack of north–south asymmetry is surprising in light of the MESSENGER discovery of a northward offset to the dipole magnetic field (Anderson et al., 2011), which results in the southern hemisphere receiving a factor of ~4 more solar wind ions than the northern hemisphere (Winslow et al., 2012, 2014).

Contrary to the conclusions of Mangano et al. (2015) and Potter et al. (2006), Schmidt (2013) reported that there is a larger source of sodium in the southern hemisphere on the basis of observations of Mercury's anti-sunward sodium "tail" (discussed in more detail below). Evidence for this asymmetry includes several observations showing excess northern tail emission (Baumgardner et al., 2008; Potter and Killen, 2008). With a Monte Carlo simulation, Schmidt showed that a northern enhancement can arise from a southern hemisphere source because sodium atoms switch hemispheres as they are pushed anti-sunward by radiation pressure, at least when they are ejected from the surface within a certain energy range. Schmidt concluded that a northern tail enhancement can be explained by a process in which solar wind ions impinging on the southern nightside hemisphere at low latitudes (Winslow et al., 2014) liberate sodium for later photodesorption at dawn in a manner similar to the mechanism proposed by Mura et al. (2009). Schmidt also cited an apparent asymmetry in the tail observed during the first MESSENGER flyby (McClintock et al., 2008), although Burger et al. (2010) concluded that this asymmetry was most likely an observational artifact and that sodium source rates from the two hemispheres were approximately equal during the flyby. Observations during Mercury transits of the Sun (Schleicher et al., 2004; Yoshikawa et al., 2008; Potter et al., 2013), discussed below, have shown no evidence of a large sodium source in the southern hemisphere. Schleicher et al. (2004) found approximately equal sodium column densities above the two poles, whereas Potter et al. (2013) found that the sodium column density was 50–100% larger above the north pole.

There have also been many studies of the distribution of sodium emission by local time (east–west). Several groups, including Sprague et al. (1997), reported that, on average, sodium emissions are brighter in the morning than in the afternoon. They attributed this pattern to the thermal desorption of sodium frozen on Mercury's nightside surface. Transit observations made at TAA = 149° by Schleicher et al. (2004) also exhibited larger sodium emission above the dawn than the dusk terminator, although Potter et al. (2013) found a dawn–dusk column density ratio close to 1 in their transit observation made at TAA = 328°. In contrast, Potter et al. (2009) claimed the detection of sodium desorption near the dawn terminator in one observation of line-of-sight Doppler shifts. They interpreted
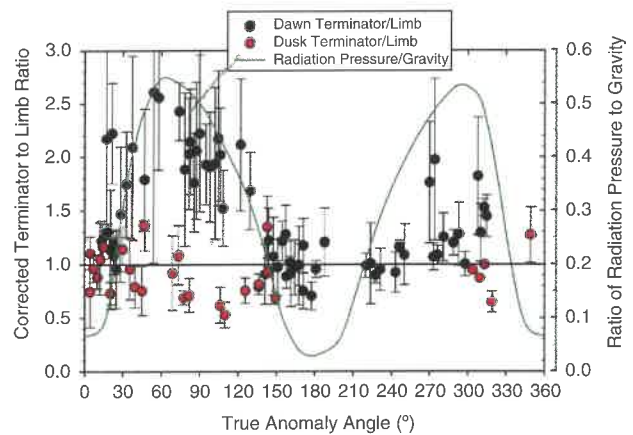

Figure 14.12. Variation with true anomaly angle of the ratio of sodium emission at Mercury's terminator to that at the limb, from observations at the McMath–Pierce Solar Telescope. For the dawn terminator data, ratio values greater than unity appear at true anomaly angles up to about 140°, and again at angles greater than about 250°. When the dusk terminator is in view, the ratio is generally less than unity, with little or no variation with true anomaly angle or radiation acceleration. The green curve is the ratio of radiation acceleration to gravitational acceleration. In these data, values of the terminator-to-limb ratio greater than unity are seen to be located in regions of maximum radiation acceleration, and the smallest values are seen to be located in regions of minimum radiation acceleration. Comparable MESSENGER observations are shown in Figure 14.24. Adapted from Potter et al. (2006).

their data as consistent with an upward flow of sodium from the surface during Mercury's early morning.

Potter et al. (2006) also surveyed the distribution of sodium emission with local time as a function of Mercury's TAA. Their results, which are summarized in Figure 14.12, indicated that emission near the dawn terminator was greater than emission from the limb (which typically corresponded to midday) during the outbound leg of Mercury's orbit, up to TAA ~ 140°, and during Mercury's inbound leg beginning near TAA ~ 250°. In contrast, their observed ratio for the dusk terminator was near unity for all observed true anomaly angles, which suggests that there is a deficit of sodium at dusk. They concluded that this apparent dawn enhancement is evidence of thermal desorption when the terminator is in motion (for much of the year the terminator is nearly motionless). At these times, sodium adsorbed on the cold nightside could be thermally desorbed. Potter et al. (2006) also pointed out that terminator-to-limb ratios greater than unity occur at times of greatest radiation pressure, whereas the smallest values occur at times of minimum pressure. They argued that radiation pressure enhances dawn emission by transporting sodium desorbed in the morning toward the terminator and into shadow.

MESSENGER observations, discussed below, also show that pre-noon local times are, on average, brighter than post-noon and that this pattern is a consequence of variations in solar radiation pressure and terminator velocity throughout the Mercury year. Those data show no evidence of thermal desorption and no sustained dawn–dusk asymmetry.

Sodium Velocity Distribution

Interest in the sodium flow arises from the early modeling work of Ip (1986) and Smyth (1986), who showed that sodium D-line

(a) Potter et al. (2009)
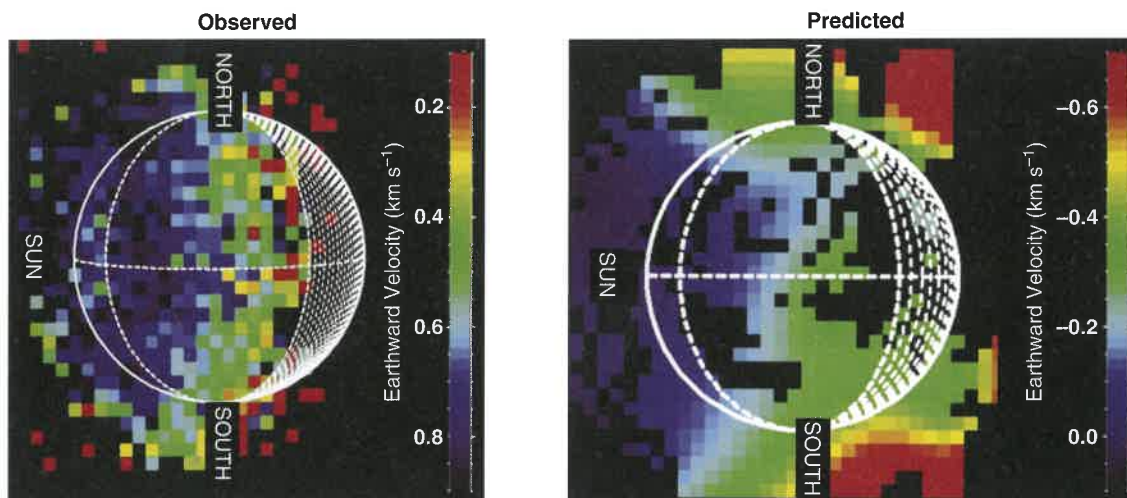

February 4, 2000
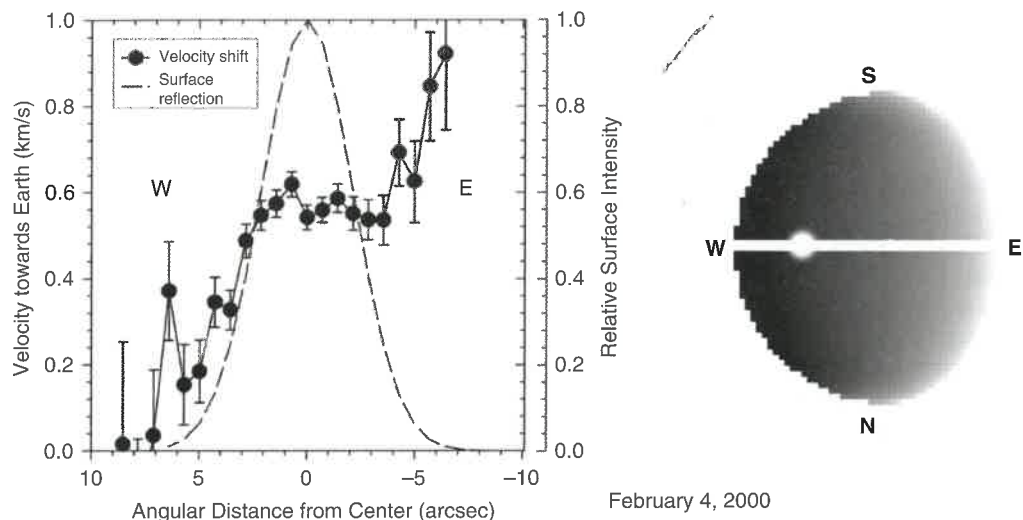
(b) Leblanc et al. (2013)

Figure 14.13. Observations of bulk sodium flow speeds in Mercury's exosphere. (a) East–west profile of Doppler shifts in sodium emission with the McMath–Pierce Solar Telescope. A zero value indicates rest with respect to Mercury's surface. The geometry of the observation is shown at right, with the subsolar point indicated by the bright circle. Adapted from Potter et al. (2009). (b) Doppler shifts with the THEMIS telescope compared with the shifts predicted by a Monte Carlo model. The observed line-of-sight velocities are comparable in magnitude with those of Potter et al., but the model-predicted Doppler shifts differ by about $1 \, \text{km s}^{-1}$. Adapted from Leblanc et al. (2013).

resonant scattering of solar photons results in radiation pressure acceleration that, during certain times of the Mercury year, is nearly as large as surface gravitational acceleration (see also Figure 14.1). Unfortunately, there are relatively few reliable measurements of the sodium bulk-flow velocity distribution on the dayside of Mercury. The Doppler shifts involved are small, typically less than $1 \, \text{km s}^{-1}$, and are difficult to measure. This flow is so small that in their discovery paper Potter and Morgan (1985) reported that the sodium exosphere was at rest with respect to Mercury.

Leblanc et al. (2008) published the first map of bulk sodium flow on Mercury's dayside, and their work was followed by that of Potter et al. (2009) and Leblanc et al. (2009, 2013). Figure 14.13 shows Doppler shift observations taken with high-resolution spectrographs from Potter et al. (2009) and Leblanc et al. (2013). Both found line-of-sight (Earthward) motion between 0 and $1 \, \text{km s}^{-1}$ relative to Mercury's surface, and both reported that the line-of-sight velocity increased away from the subsolar point. Leblanc et al. (2008) reported that the velocity continued to increase all the way to the terminator, whereas Potter et al. (2009) found that the velocity usually has a maximum between the subsolar point and the terminator.

Though the two sets of observations have many similarities, the two papers had different interpretations. Potter et al. (2009) concluded that they had observed sodium flowing from the subsolar point to the terminators as a result of acceleration by radiation pressure. Leblanc et al. (2013), in contrast, rejected that interpretation because their Monte Carlo model (Leblanc
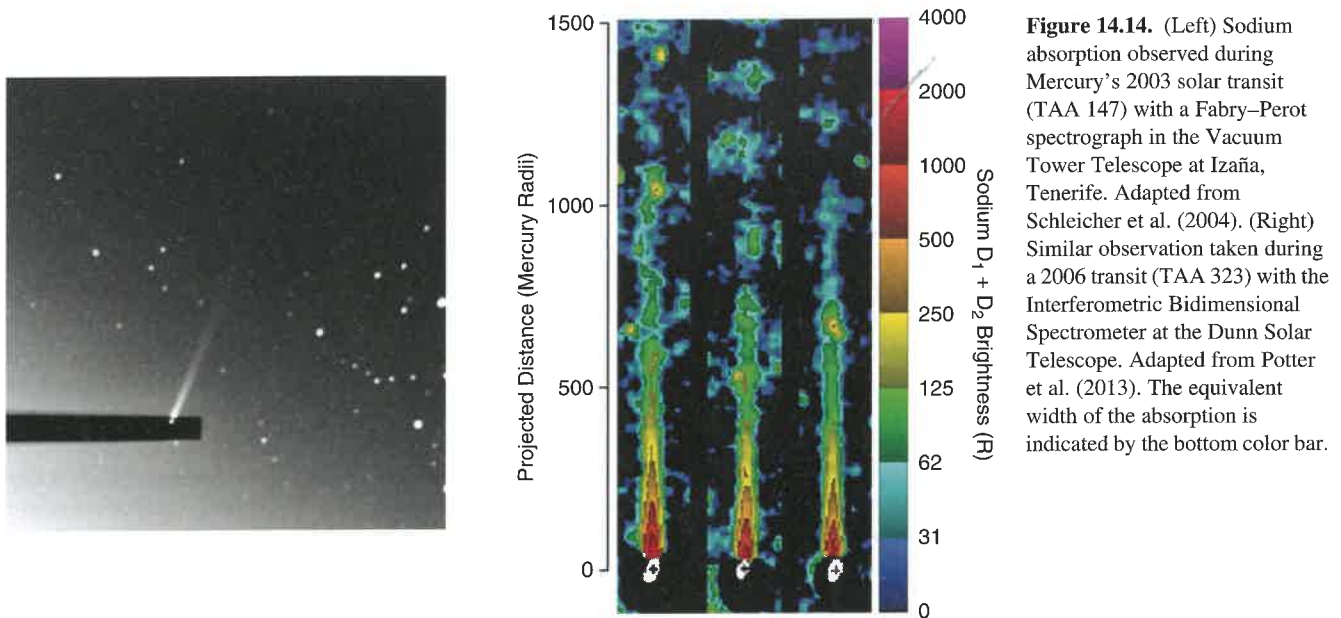
Figure 14.14. (Left) Sodium absorption observed during Mercury's 2003 solar transit (TAA 147) with a Fabry–Perot spectrograph in the Vacuum Tower Telescope at Izaña, Tenerife. Adapted from Schleicher et al. (2004). (Right) Similar observation taken during a 2006 transit (TAA 323) with the Interferometric Bidimensional Spectrometer at the Dunn Solar Telescope. Adapted from Potter et al. (2013). The equivalent width of the absorption is indicated by the bottom color bar.
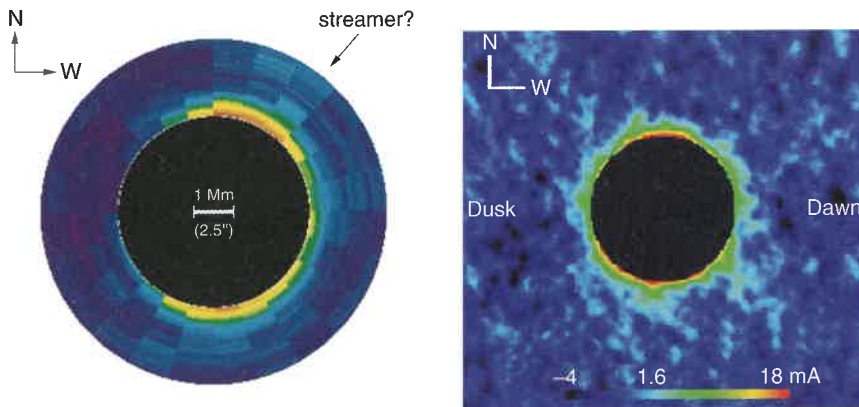

Figure 14.15. (Left) Coronagraph observation of Mercury's sodium tail taken at the Boston University station at McDonald Observatory on 30 April 2009 with a narrowband filter centered on the sodium D lines. Image adapted from Schmidt et al. (2012). (Right) Processed sodium tail observations from the same facility, taken in May–June 2007. The Sun is in the downward direction, and the white area indicates the uncertainty in Mercury's position.

and Johnson, 2010) predicted that the exosphere should be, on average, at rest with respect to Mercury. Although the patterns of flow were similar between observation and model, the magnitude of these Doppler shifts differed by about 1 km s^{-1}. Leblanc et al. (2013) concluded that their observed Doppler shifts were miscalibrated, i.e., their measurements of sodium Doppler shift over Mercury's dayside were consistently in error by about 1 km s^{-1}. The alternative is that a well-established Monte Carlo model failed to reproduce basic features of sodium transport.

Terminator Observations

Two groups (Schleicher et al., 2004; Potter et al., 2013) measured sodium absorption above Mercury's limb, as described in Section 14.3.2. These observations permitted measurements of the sodium scale height, Doppler shift, and energy distribution. Both observations are shown in Figure 14.14. Similar to the Schleicher et al. (2004) observations, Potter et al. (2013) observed enhanced absorption near the poles, but in contrast to the findings of Schleicher et al. (2004) they did not observe a

dawn–dusk asymmetry. These workers reached broadly similar conclusions about the sodium speed distribution: scale heights are consistent with a temperature on the order of 1000 K (with large variations), and the Doppler width is consistent with that temperature combined with a bulk anti-sunward flow on the order of 1 km s^{-1}.

Sodium Tail Observations

Ip (1986) and Smyth (1986) predicted that radiation pressure acceleration as a result of resonant scattering of solar photons would be sufficiently strong to accelerate sodium atoms to escape velocity and so form a long anti-sunward tail. Such a tail was first successfully observed by Potter et al. (2002a) using the McMath Pierce image slicer. Later, Baumgardner et al. (2008) and Schmidt et al. (2010) observed the tail using a narrow-band interference filter at the McDonald Observatory – a first for Mercury's exosphere and ideal for the distant sodium tail, where scattered sunlight from the surface is negligible. The Baumgardner et al. and Schmidt et al. observations were made with a wide-field coronograph that occulted Mercury's disk,

allowing long exposures that could detect sodium from ~20 to ~1000 R_M anti-sunward of Mercury (where R_M is Mercury's radius), as illustrated in Figure 14.15. Schmidt et al. (2012) modeled these observations and concluded that the tail is supplied primarily by low-energy sources such as impact vaporization (approximated in the model as a 3000 K Maxwellian distribution) and/or photon-stimulated desorption (approximated as a 1500 K Maxwellian distribution). Additionally, they concluded that there must also be a weaker, high-energy source component in order to match the observed widths of north–south cross-tail profiles. They suggested that this source is supplied by the high-energy "tail" of the energy distribution for photon-stimulated desorption observed by Johnson et al. (2002).

Potter and Killen (2008) observed the emission and Doppler shift of sodium atoms in the tail from ~4000 km to ~46,000 km anti-sunward of Mercury's center (Figure 14.16). Unlike the dayside Doppler shift observations discussed above, there is little ambiguity in estimating sodium velocity in the distant tail. The direction of the flow is known to be approximately anti-sunward, and the magnitude of the Doppler shift is many kilometers per second, much larger than the Doppler shifts on
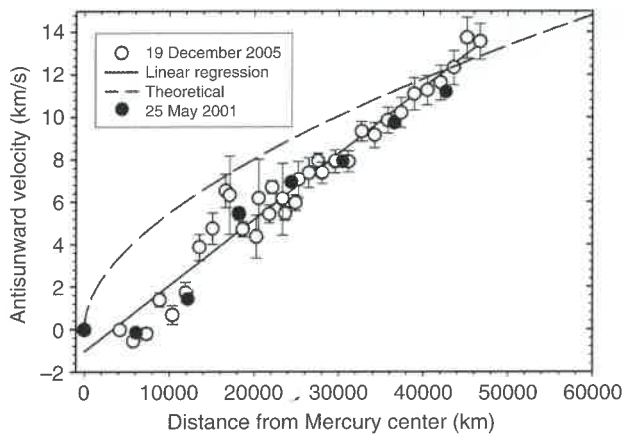

Figure 14.16. Sodium tail velocities derived from the Doppler shift observed with the high-resolution echelle stellar spectrograph at the McMath–Pierce Solar Telescope. Adapted from Potter and Killen (2008).

the dayside. From the variability of the tail with TAA, particularly the apparent disappearance of the tail below a particular threshold value of radiation acceleration, Potter and Killen concluded, contrary to the conclusion of Schmidt et al. (2012), that the distant tail is primarily supplied by a high-energy source such as sputtering.

14.4.1.2 MESSENGER Observations

During MESSENGER's Mercury flybys, the UVVS observed the sodium exosphere by obtaining profiles of the tail and performing "fantail" observations during a spacecraft roll in Mercury's shadow (McClintock et al., 2008, 2009; Vervack et al., 2010). An image constructed from the M1 observations of the sodium tail is given in Figure 14.5, and images constructed from M2 and M3 observations are shown in Figure 14.17. A key feature of these images is a brightening of the exosphere above the poles in all three observations. The weak emission during M3 (TAA = 331°) relative to that observed during M1 (TAA = 285°) and M2 (TAA = 293°) was at least partly the result of lower solar radiation pressure near perihelion (Figure 14.1).

Sodium fantail radiances for M2 and M3 are shown in Figure 14.18a along with two models of the M2 observations constructed by Burger et al. (2010). These comparisons indicate that the M2 observations are better fit by a high-latitude dayside source than a uniform source.

MESSENGER also measured limb profiles of sodium emission versus altitude above the polar regions during M3 (Vervack et al., 2010), which are displayed in Figure 14.19a. These observations revealed a two-component structure to the sodium exosphere consistent with that observed routinely during MESSENGER's orbital phase (see below). Fits to exponential functions yielded near-equal intensities for both poles and profiles with e-folding distances of ~200 km for altitudes less than 800 km and ~500 km for higher altitudes.

Coincident with the M1 flyby, observations of Mercury's dayside were obtained with the McMath Pierce image slicer. Mouawad et al. (2011) used both spacecraft and ground-based observations as constraints for a Monte Carlo exosphere model. They concluded that the primary sodium source had an energy distribution similar to a 1000 K Maxwellian, possibly with a high-energy tail, in order to match simultaneously the dayside
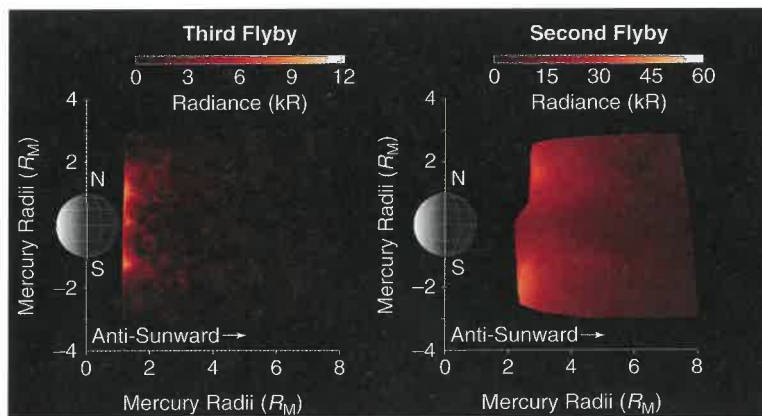

Figure 14.17. Comparison of observations from the third (left) and second (right) MESSENGER flybys of Mercury, which occurred at TAA = 331° and TAA = 293°, respectively. The markedly lower sodium tail emission during M3 is the result of relatively small solar radiation pressure during M3. The images show observed column emissions projected onto the plane containing the Sun–Mercury line and Mercury's spin axis, interpolated to fill in unobserved regions. The region (1–2) R_M anti-sunward from the planet was not sampled during M2.
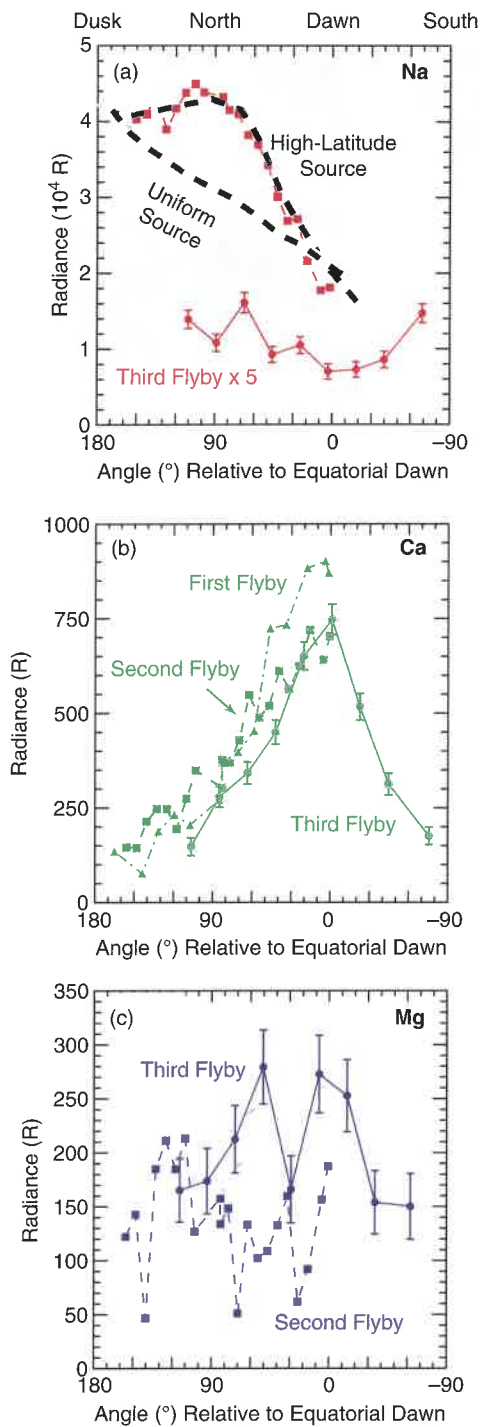
Figure 14.18. Fantail observations of (a) sodium, (b) calcium, and (c) magnesium in Mercury's tail taken during MESSENGER's Mercury flybys. Each panel shows observed radiance as a function of angle relative to equatorial dawn (0°) for the second and third flybys. Data from the third flyby are shown with one-standard-deviation uncertainties; uncertainties in the observations from the first and second flybys are slightly smaller owing to longer integration times but are omitted for clarity. Predictions of two models of the sodium observations from the second flyby, including a uniform source and a high-latitude northern-hemisphere source, are shown in (a) with black dashed lines (Burger et al., 2010). The sodium emissions during the third flyby were much lower because of the low sodium g-value at that time. By contrast, calcium observations (b) show a clear dawn–dusk asymmetry, with dawn (0°) brighter than dusk (180°). Adapted from Vervack et al. (2010) and Burger et al. (2010).

and tail data. They also obtained an upper limit on an impact vaporization source (assumed to be at 5000 K). This upper limit was consistent with the impact vapor production predicted by Morgan et al. (1988) but two orders of magnitude smaller than that of Borin et al. (2010).

Observations of Mercury's sodium exosphere from orbit were described by Cassidy et al. (2015), who focused on dayside limb scans (Figures 14.3 and 14.8) above the equatorial region (approximately 30°S to 30°N, Figure 14.9) and similar scans above the south polar terminator. Figure 14.20, taken from Cassidy et al. (2015), shows the total sodium emission as a function of tangent altitude for 1400 local time and TAA ~ 112°. These are typical sodium dayside limb profiles that illustrate features seen throughout the mission. There are two distinct temperature components (Vervack et al., 2010), a relatively dense and cold component with a small scale height (~100 km) and a tenuous hot component seen at the highest altitudes probed by the limb scans (up to 4000 km).

Cassidy et al. (2015) extracted information from limb profiles using the model of Bishop and Chamberlain (1989), which includes the effects of radiation acceleration (Section 14.2). This modeling permitted estimates of temperature and near-surface density as functions of TAA, as shown in Figure 14.21 for limb scans taken near the subsolar point. These results were obtained for the relatively cold and dense component that comprises the bulk of the exosphere. The derived temperature of this colder component is relatively constant at about 1200 K, which is warmer than the surface but much colder than predicted by many candidate source processes, suggesting that the most likely source process is photon-stimulated desorption. Cassidy et al. (2015) were not able to constrain the temperature of the hot component from limb profiles. They showed that models with temperatures in the range 5000–20,000 K fit the hot component equally well.

Ground-based observers typically use Doppler broadening to infer temperatures, which is not possible with the relatively low spectral resolution of MASCS measurements. Temperatures inferred in this way are, with one exception (Killen et al., 1999), much larger than the ~1200 K inferred by MASCS limb scan data (see summary by Cassidy et al., 2015). However measurements of the exosphere's scale height during solar transits (Schleicher et al., 2004; Potter et al., 2013) found values comparable with those measured by MASCS (Figure 14.21).

Thermalization, the thermal equilibration of atoms with a surface, is seen in laboratory experiments with sodium atoms adsorbed on a variety of substrates (e.g., Yakshinskiy and Madey, 2005) and is also a common assumption underlying Monte Carlo models of Mercury's exosphere, such as those of Smyth and Marconi (1995), Mura et al. (2009), and Leblanc and Johnson (2010). Cassidy et al. (2015) searched their data for a colder, thermalized component. Their demonstration of what limb profiles would look like with the addition of a thermalized component is given in Figure 14.22 for two different local times: early morning, during which thermal desorption might release sodium atoms adsorbed on the nightside; and at the subsolar point, where the surface is warmest. They added a surface-temperature component to the fitted model, giving it the same vertical column density as the warmer component. The surface temperature used was typical for that local time (Yan et al., 2006). The top panel of Figure 14.22 (early morning) shows that an abundant thermalized component would be
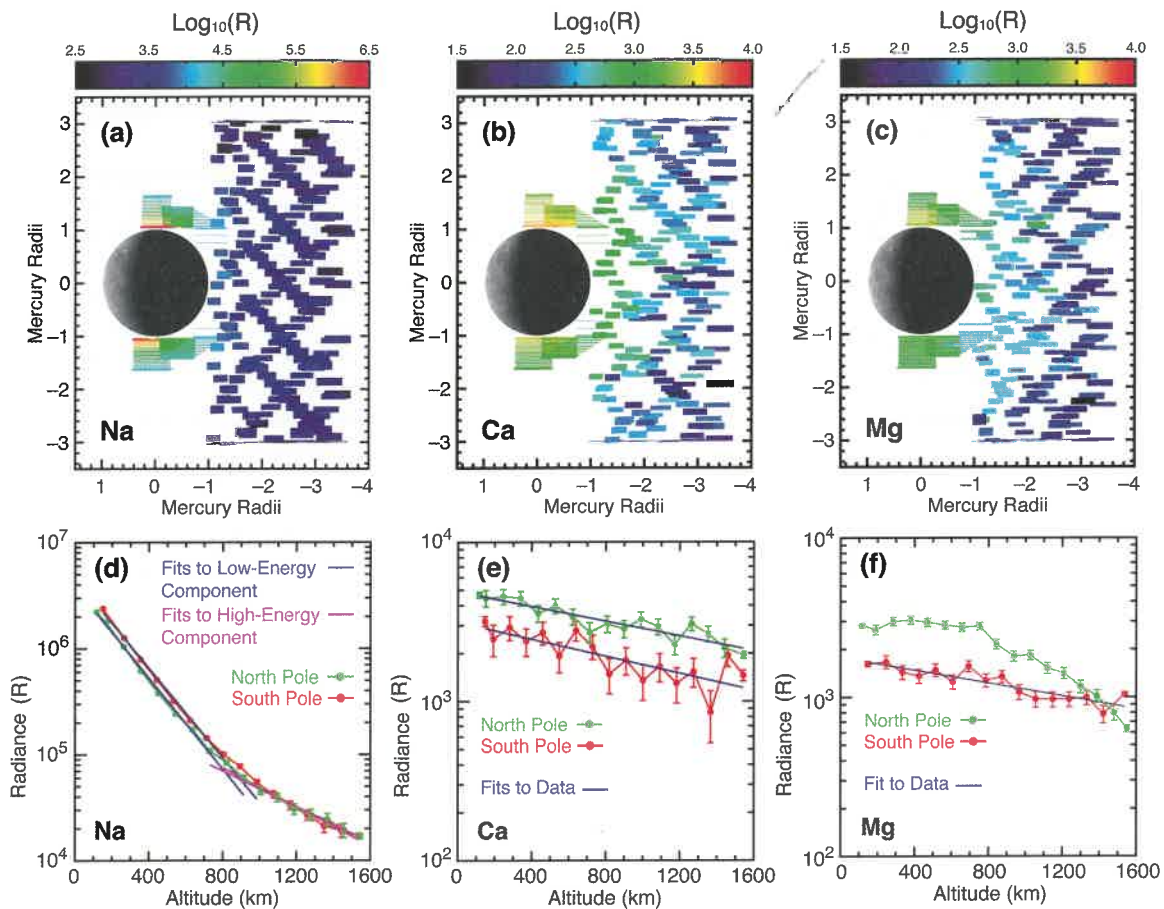
Figure 14.19. (a)–(c) Observations of sodium, calcium, and magnesium emission in the polar, nightside, and tail regions of the planet during MESSENGER's third flyby. Each observation is represented by the projection of the instrument's rectangular field of view onto the plane defined by the Sun–Mercury line and the spin axis of Mercury. The horizontal dimension of the filled rectangles indicates the length of the slit as projected onto the plane and becomes smaller as the spacecraft approaches Mercury; the vertical extent of the rectangles indicates the range over which the UVVS slit moved during the integration time (1.5–2.0 s), with shorter distances corresponding to slower rates of slewing by the spacecraft. Each observation is thus an average of the emission over the indicated region. Owing to the location of the spacecraft during these observations, the lines of sight are not perpendicular to the plane but are directed sunward by 5–10°. (d)–(f) Profiles of sodium, calcium, and magnesium emission with altitude over the north and south poles of the planet (shown with one-standard-deviation uncertainties). Exponential fits to the data indicating the general behavior of each species are also shown. The lone exception is magnesium over the north pole, which cannot be fit with such a simple model, as discussed in the text.
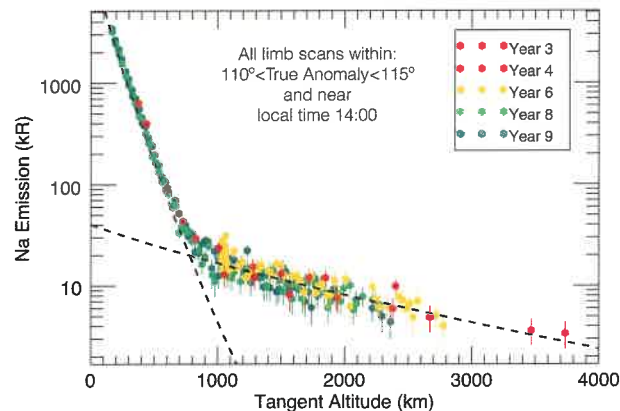

Figure 14.20. MESSENGER limb emission profiles of sodium in Mercury's exosphere taken from orbit (adapted from Cassidy et al., 2015) and associated Chamberlain models (dashed lines). This figure includes every limb emission profile within short ranges of true anomaly angles and local time (as labeled). Repeatable observation geometry during the mission permitted comparison among Mercury years. As is typical for dayside sodium limb emission profiles, there are two components at different temperatures; these profiles are well approximated by Chamberlain models at 1230 K and 20,000 K.
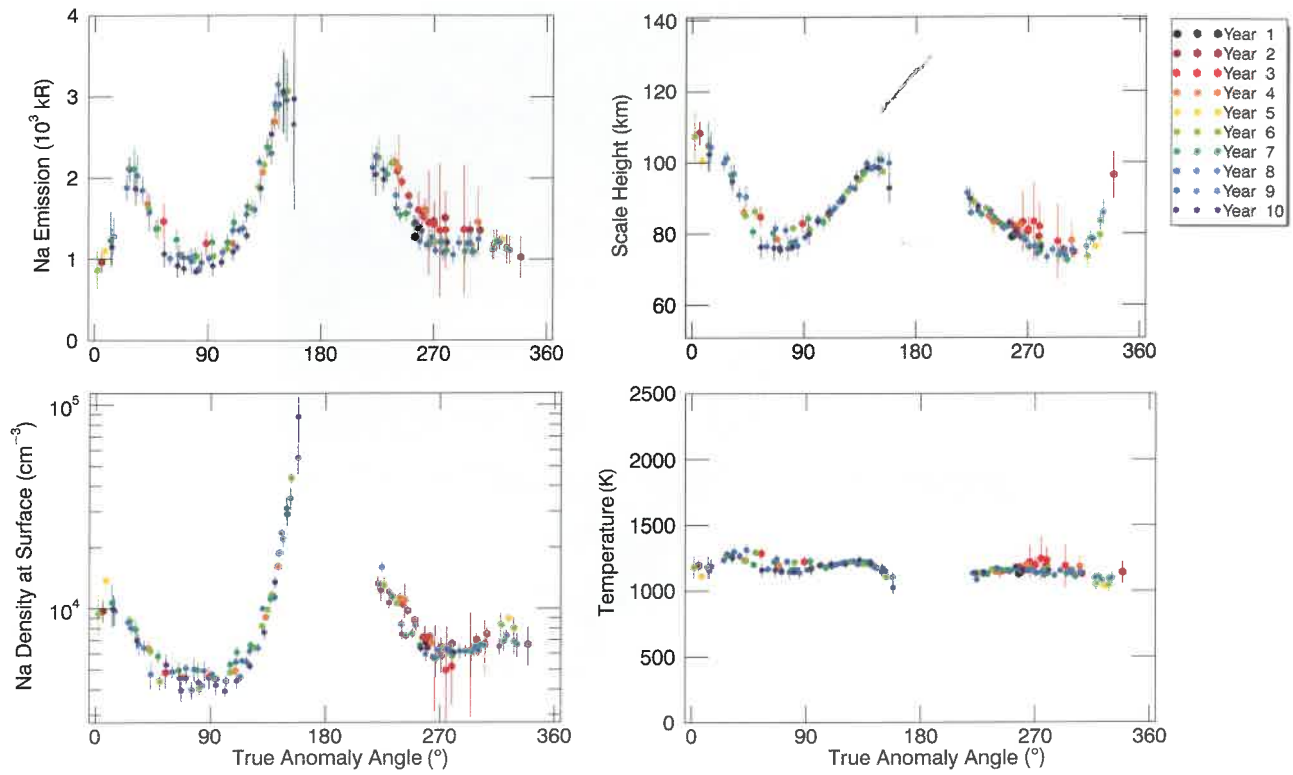
Figure 14.21. Properties of Mercury's sodium exosphere near the subsolar point as a function of true anomaly angle. (Top left) Radiance at 300-km altitude obtained by interpolation of the limb profiles. (Top right) Scale height of the dominant colder component. (Bottom left) Surface density. (Bottom right) Temperature of the colder component. Adapted from Cassidy et al. (2015).
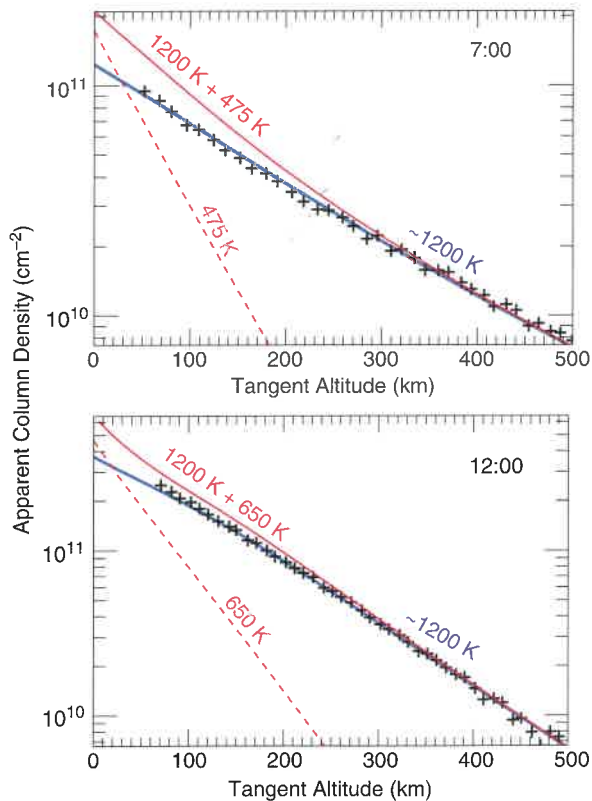

Figure 14.22. Cassidy et al. (2015) found no evidence for a substantial cold sodium exosphere that would indicate accommodation with the surface temperature. Examples of their search for a surface-temperature component are shown for early morning (07:00 local time) and the subsolar point (12:00). The solid red line shows a notional limb emission profile near the surface with the addition of a surface-temperature component added to the observed 1200 K component. For this example, it was assumed that the surface-temperature component has the same vertical column density as the 1200 K component.
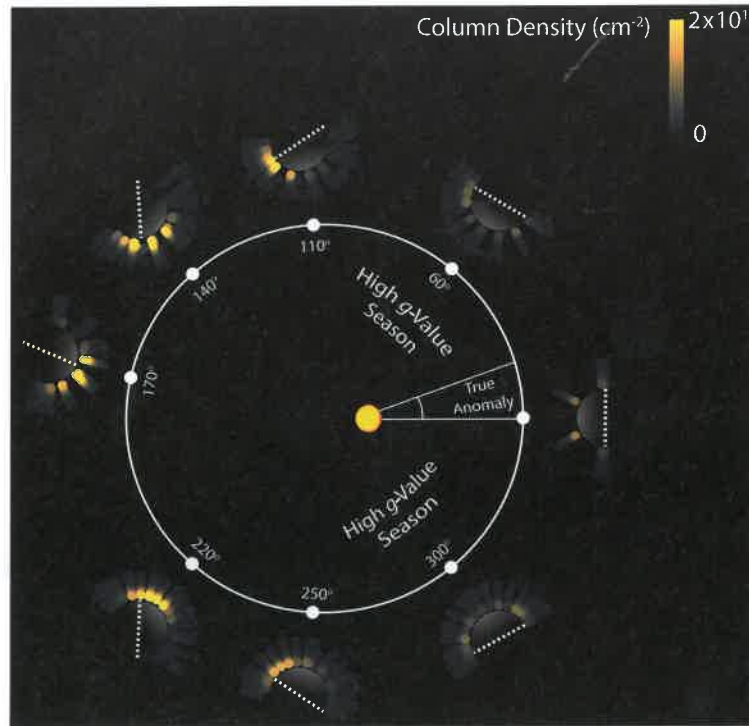
Figure 14.23. The distribution of dayside sodium column density over the course of one Mercury year as seen from above the north pole. Sodium emission is enhanced above one of the two "cold pole" longitudes (connected by dotted lines). As that surface rotates into the sunlight, it becomes a strong localized source of sodium. There is no persistent dawn–dusk asymmetry. Whereas dawn is brighter than dusk on the outbound leg from TAA = 60° to TAA = 180°, dusk is brighter than dawn on the inbound leg from TAA = 180° to TAA = 300°. Near perihelion the emission is approximately uniform over the dayside. To produce this figure, MESSENGER UVVS observations with low-latitude line-of-sight tangent points (<30° latitude) were projected onto the equatorial plane.

obvious but was not evident in the data. At the subsolar point (bottom panel), the difference was much more subtle. Although Cassidy et al. (2015) did not rule out the presence of a thermal component, they concluded that it is constrained to be much less abundant than the ~1200 K component in the dayside limb profiles.

Thermal desorption of sodium at dawn or in the morning has been one of the mechanisms invoked in the literature to explain dawn–dusk asymmetries in some of the ground-based observations of sodium emission (e.g., Leblanc and Johnson, 2003, 2010; Peplowski et al., 2014), as discussed above. MESSENGER observations show that changes in the dawn-to-dusk emission ratio do not necessarily imply a thermal desorption source but are rather the consequence of seasonal variations in solar radiation pressure and Mercury's orbital angular rate. Figure 14.23 illustrates the sodium column densities observed by MESSENGER throughout a Mercury year. Over the TAA range ~270° to ~90°, centered on perihelion, the planet's rotation rate is nearly equal to its orbital angular rate. During this time the terminators are nearly stationary and sit near the "cold poles" (geographical longitudes −90° and 90° E). At these times the sodium g-value reaches its maximum and anti-sunward transport is most robust (see Figure 14.1). As a consequence, the cold poles collect sodium atoms that migrate from the dayside to the nightside in response to solar radiation pressure. As Mercury's distance from the Sun increases, the planet's orbital angular rate slows and the dawn cold pole

rotates into sunlight, where the sodium sequestered on the surface is released into the exosphere. The release-enhanced emission over the cold pole declines slowly as Mercury progresses in its orbit, and it continues as the pole rotates toward the evening terminator. Thus, the morning is substantially brighter than the afternoon for most of the outbound portion of Mercury's orbit, and the afternoon is slightly brighter than morning during the inbound portion of Mercury's orbit (Cassidy et al., 2016).

This result is consistent with the ground-based observations shown in Figure 14.12. In Figure 14.24 the radiances observed by MESSENGER in the morning (local times 0600–1000) and afternoon (1400–1800) are ratioed to those at midday (1000–1400). Morning and afternoon correspond approximately to what Potter et al. (2006) refer to as the "dawn" and "dusk" terminators, as ground-based observations taken near the terminators will necessarily include emissions from much of the dayside as a result of smear from imperfect atmospheric seeing. The "limb" in the observations of Potter et al. (2006) was usually near midday. As in Figure 14.12, MESSENGER observations show a strong morning enhancement for much of the outbound leg (TAA < 180°) and no morning–afternoon asymmetry near perihelion. Unlike Figure 14.12, MESSENGER observations show that the afternoon is brighter than the morning for much of each outbound leg (180° < TAA < 300°). This TAA range is where Figure 14.12 has a gap in "dusk" observations.

A remarkable feature of the MESSENGER sodium limb profiles is their annual repeatability. For a given true anomaly and local time, observations change little over many Mercury years. It is unlikely that ion bombardment from the ever-changing space weather environment (Slavin et al., 2014) could produce the observed pattern. Although MESSENGER orbit and pointing constraints precluded low-altitude (<1000 km above the surface) limb scans directly above the cusp regions (Figure 14.8), the observations shown in Figure 14.21 were taken over portions of the surface that are bombarded by ions on the nightside (Winslow et al., 2014). No clear signature of this process can be seen in the MESSENGER data.

14.4.2 Potassium

Potassium in Mercury's exosphere can be observed with ground-based telescopes via emissions from its D lines located at 766.49-nm and 769.90-nm wavelength. It has been
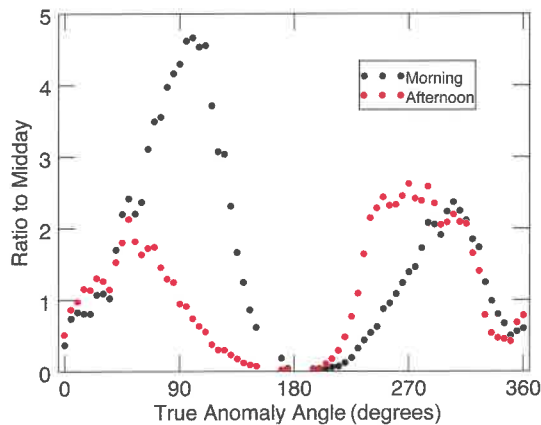

Figure 14.24. Morning–afternoon asymmetries in MESSENGER observations of exospheric sodium. These quantities, the ratio of morning or afternoon radiance to that at midday, are approximately comparable to the terminator-to-limb ratios shown in Figure 14.12. Both sets of observations show a pronounced morning enhancement during the outbound leg of Mercury's orbit, whereas the afternoon is brighter than the morning during the inbound leg, where Figure 14.12 has a gap in observations.
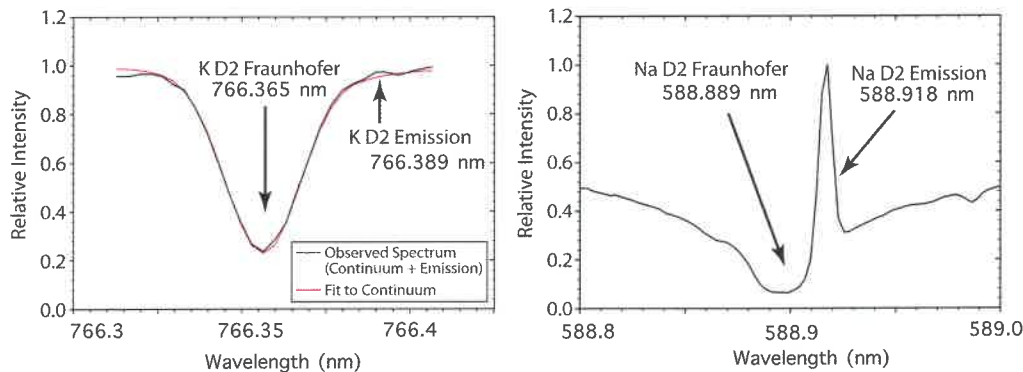
observed less frequently than sodium because of its lower abundance and because large Doppler shifts are required to avoid contamination from telluric molecular oxygen lines. Figure 14.25 compares sodium and potassium spectra obtained on 17 January 2008 at the McMath–Pierce Solar Telescope at the Kitt Peak National Observatory (Killen et al., 2010). Whereas sodium emission dominates the signal at 588.918 nm, the potassium signal is a weak feature superimposed on a much brighter spectrum of sunlight reflected from the planet's surface. Nonetheless, disk-averaged potassium data were published for 18 dates in 1988, 1990, 1998, and 1999 (Potter et al., 2002b). These show that the potassium column density varied over the range $(0.7–4) \times 10^9$ cm^{-2}. The sodium/potassium ratio was observed to be highly variable, between ~30 and ~140, and was highly correlated to Mercury sub-observer longitude and weakly correlated to radiation pressure acceleration.

Examples of disk-resolved observations of sodium and potassium are shown in Figure 14.26. The left panel shows disk images obtained by Killen et al. (2010) on 17 January 2008 near the time of the first MESSENGER flyby, and the right panel shows sodium/potassium ratios observed at several positions by Doressoundiram et al. (2010) on 17 and 19 June 2006. Killen et al. (2010) reported that the sodium/potassium ratio peaked at high latitudes on the dayside, at a value on the order of 100, and that the equatorial ratio was smaller than this value, at about 30. The sodium/potassium ratio varied with altitude above the limb, as expected, given that the sodium scale height is expected to far exceed that of heavier potassium. Their southern hemisphere potassium column density was 1.3×10^9 cm^{-2}, and their average potassium zenith column in the north, 8×10^8 cm^{-2}, was close to the detection limit of 6.8×10^8 cm^{-2}. Doressoundiram et al. (2010) also reported sodium/potassium column density ratios that varied over Mercury's surface, ranging from ~60 near the equator to ~400 at high latitudes on the dayside and up to 160 near the pole on the nightside. Their potassium column densities were reported to be between 6×10^8 and 1×10^{10} cm^{-2}.

The spectral range of the MESSENGER UVVS instrument was limited to wavelengths less than 610 nm, which is below the strong potassium D-line observations described above. Attempts to detect the potassium emission lines located at 404.48 nm and 404.52 nm, which have g-values that are

Figure 14.25. (Left) Observations of exospheric potassium on Mercury acquired at the McMath–Pierce Solar Telescope. The wavelength scale is given in Earth's rest frame, which is Doppler shifted by -0.101nm with respect to Mercury's rest frame. (Right) Sodium D$_2$ line emission, also plotted in Earth's reference frame for comparison, shows the relative difficulty of observing potassium. Adapted from Killen et al. (2010).
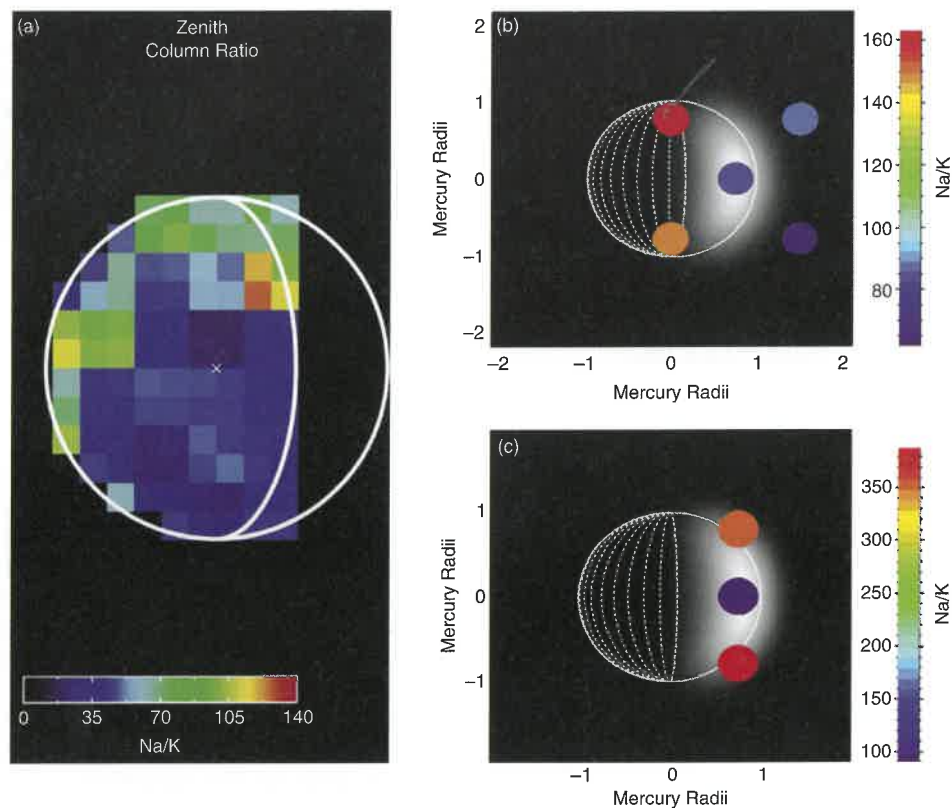
Figure 14.26. (a) Line-of-sight sodium/potassium ratio measured with the McMath–Pierce Solar Telescope. The ratio in the southern hemisphere (~36), which is close to the noise-equivalent column, is close to the smallest ratio found in the data sets considered by Potter et al. (2002a), whereas the ratio in the northern hemisphere (~74) is near the mid-value found previously (Killen et al., 2010). (b) Sodium/potassium ratios measured by Doressoundiram et al. (2010) from ~60 near the equator to ~400 at high latitudes on the dayside and up to 160 near the pole on the nightside.

approximately 1000 times smaller than those for the D lines, were not successful.

14.4.3 Calcium

14.4.3.1 Ground-Based Observations

Mercury's calcium exosphere was discovered with ground-based observations at the Keck Observatory by Bida et al. (2000); see Figure 14.27. From the observed line widths, it was clear that calcium is hot, with a temperature ~12,000 K. It was also determined that the calcium exosphere is much more tenuous than the sodium exosphere; the estimated calcium column density was more than three orders of magnitude lower than the sodium column density (e.g., Potter and Morgan, 1985). The observations described a calcium exosphere that varies both temporally and spatially. The spatial distribution of calcium was not well determined; emission was seen over the poles but was not observed over the subsolar point because scattering from the surface made detection over this point unreliable. Bida et al. (2000) considered three sources for the observed neutral calcium: photon-stimulated desorption, micrometeoroid impact vaporization, and ion sputtering, preferring the last because of the observed high energy of the calcium and the enhanced emission over the poles.

Killen et al. (2005) partially mapped the calcium around Mercury using observations acquired at the Keck Observatory

between 1997 and 2002. A gradual increase in radiance was seen during this period, although this increase can partly be explained by variations in the g-value, which increased over time for the nights analyzed. However, a small increase in calcium column density was observed over time, which may be consistent with the seasonal variability in calcium source rate found from MESSENGER data by Burger et al. (2014) and discussed below. Killen et al. (2005) also confirmed the presence of energetic calcium through measurements of the emission line width (consistent with temperatures between 12,000 K and 20,000 K) and the Doppler shift of the emission from the expected wavelength. The emission was found to be blueshifted by motion toward the observer at speeds of a few kilometers per second. As only the dawn hemisphere was observed by Killen et al. (2005), it was not clear whether this high-velocity calcium was present at dusk as well. Because of the high energy of the ejected calcium, the preferred ejection process was either ion sputtering or the photodissociation of calcium-bearing molecules (such as calcium oxide) resulting from micrometeoroid impact vapor.

14.4.3.2 MESSENGER Observations

MESSENGER observed calcium emission from Mercury's exosphere during all three flybys and on a near-daily basis once in orbit around the planet. During the first MESSENGER flyby, UVVS observed calcium in two regions. First, calcium was seen
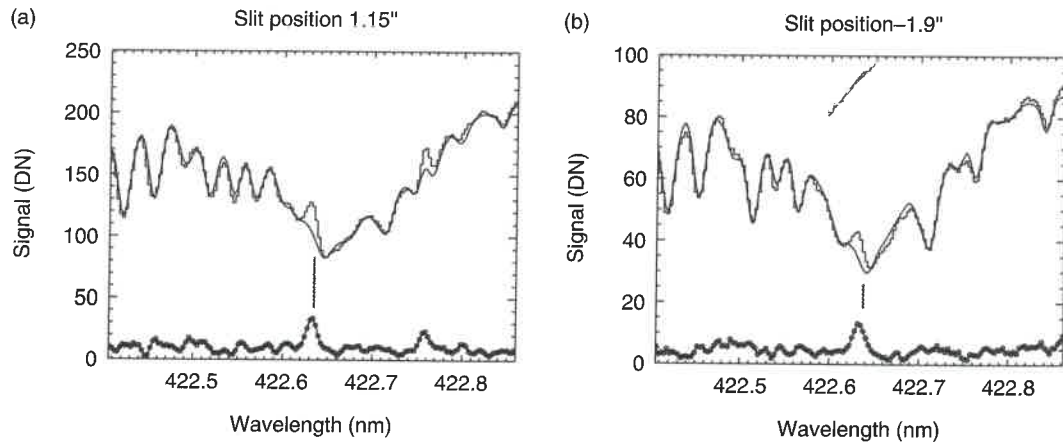
Figure 14.27. Samples of calcium emission spectra obtained at the W. M. Keck Observatory by Bida et al. (2000) on (a) 7 July 1998 and (b) 19 July 1998. The histogram plots show the observed spectra, and the solid lines are the fitted sky continuum. Differencing these two reveals the exosphere emission shown by the circle-symbol plots. The expected position of the Doppler-shifted calcium emission line is indicated by a vertical line. DN denotes digital number. Adapted from Bida et al. (2000).
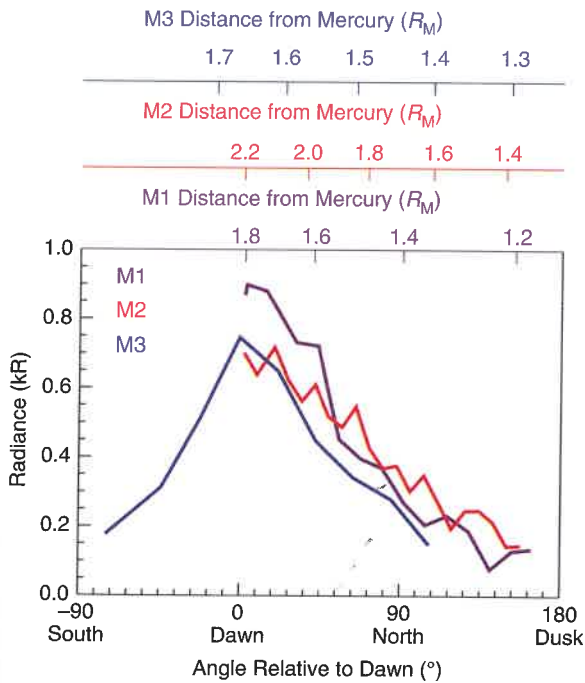

Figure 14.28. Calcium fantail measurements from each of the MESSENGER flybys of Mercury. The abscissa gives the direction of the MASCS boresight relative to the equatorial dawn direction, with positive values indicating that UVVS was pointing north of the equatorial plane and negative values indicating southward pointing. The top axes give the radial distance of MESSENGER from Mercury's center. These observations presented the first evidence that calcium is concentrated toward dawn.

during the fantail observations (Section 14.3.3.1), which occurred in Mercury's shadow near closest approach to the planet. As MESSENGER emerged from shadow, UVVS pointed toward the surface, measuring emission over the pre-dawn and dawn terminator regions where the sodium/calcium ratio was observed to increase from 10 at the end of the fantail
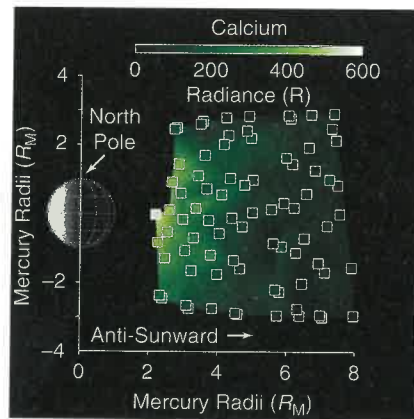

Figure 14.29. Observations of calcium emission from Mercury's tail acquired during M2. Individual observations (white squares) are overlaid on an image generated by projecting the observed line of sight onto the plane containing the spin axis and the Sun–Mercury line. Adapted from McClintock et al. (2009).

to 50 just before the UVVS line-of-sight crossed the terminator (McClintock et al., 2008). Similar fantail observations were made during the second and third flybys (McClintock et al., 2009; Vervack et al., 2010). Comparisons of the fantail measurements from the three flybys are shown in the middle panel of Figure 14.18 and in Figure 14.28. Flybys M2 and M3 also included observations in the tail over the nightside of the planet (Figure 14.29). During M3, UVVS also measured profiles of calcium emission versus altitude above the north and south poles (Figure 14.19b and 14.19e) which exhibited a single temperature component. Vervack et al. (2010) made exponential fits to these profiles and reported e-folding values of 1878 km in the north and 1621 km in the south as well as a north/south intensity ratio of 1.6 at the surface. Analysis by Burger et al. (2012) produced similar e-folding values (1840 ± 140 km and 1716 ± 200 km) and surface intensity ratio (1.4).

The flyby observations revealed several key features of the calcium exosphere, which indicated substantial differences from the sodium exosphere. First, the large scale heights over the poles (~1800 km) indicated an energetic calcium source, consistent with the ground-based observations. The tail observations are strikingly different from the sodium tail observations (Figures 14.5 and 14.17). Whereas sodium shows the brightest emission north and south of the equator, calcium was brightest in the equatorial region. Also, the calcium radiances measured in the tail region were approximately stable between the two flybys whereas sodium showed a large seasonal variation because of differences in the radiation pressure. Finally, the fantail observations indicated a large dawn–dusk asymmetry. During all three flybys, the peak radiance was measured when UVVS pointed toward dawn and decreased as the spacecraft rolled through north toward dusk. Burger et al. (2012) modeled this dawn–dusk asymmetry with a source located entirely on the dawn hemisphere.

A more complete view of the exosphere was derived from the orbital observations, which spanned a wide range of observing geometries, as described above. Burger et al. (2014) summarized observations of dayside limb scans from MESSENGER's primary and first extended missions. These data confirmed the dawn enhancement in the calcium emission. Figure 14.30 presents a visual representation of the limb profiles from three orbits at different true anomalies. Small-scale variations in the images are not real but are created by statistical variations in the radiances of the individual limb profiles. However, the large-scale trends seen in the data (in particular the dawn–dusk asymmetry) are real. Burger et al. (2014) cautioned that the images are intended as a qualitative visualization of the data, and the interpolated values should not be used in quantitative analysis.

Burger et al. (2014) also discovered a strong seasonal variation in the calcium emission. Figure 14.31 presents the results of their fits of exponential functions to limb profiles using the function

$$4\pi I(A, L) = 4\pi I_0(L)e^{-A/H} \tag{14.9}$$

where $4\pi I_0$ is the radiance at the surface at local time L, A is the altitude above the surface, and H is the e-folding width. Burger et al. (2014) pointed out that H is not a true scale height [equation (14.8)] because the e-folding width is strongly affected by ionization, and the calcium ionization rate is less than 1 h (Huebner and Mukherjee, 2015). Therefore, much of the calcium ejected from the surface is ionized within the first several thousand kilometers of leaving the surface. Several features are apparent from these plots. First, there is a strong seasonal variation in the surface radiance at dawn (Figure 14.31a). Second, there is very little year-to-year variability in the surface radiance, indicating that the exosphere is repeatable from one year to the next. Third, the e-folding width is approximately constant over a Mercury year, although the results are somewhat noisy (Figure 14.31b). There may be a small seasonal variation, with H peaking at aphelion and being minimized at perihelion, consistent with the inverse-square variation in calcium ionization rate with distance from the Sun. Much of the variation in the surface radiance can be explained by variations

in the g-value. Figure 14.31c shows the approximate surface column density derived from $N = 10^9\ 4\pi I/g$, where $4\pi I$ has units of kR, g is the g-value of an atom at rest relative to Mercury, and the column density at the surface, N, has units of cm^{-2}. Use of this equation introduces a systematic error because of the assumption that the atoms are at rest relative to Mercury. As discussed above, however, it is known that calcium is ejected energetically from Mercury. Killen et al. (2005) found temperatures up to 20,000 K; the models of Burger et al. (2012, 2014) suggest T values of ~50,000–70,000 K. The thermal speeds associated with these temperatures are 3–5 km s^{-1}. Speeds this high can result in significant differences in the g-value of such an atom from that for one at rest relative to Mercury, particularly at the subsolar point where atoms have a large component of their velocity along the Sun–Mercury line. This systematic error has the greatest impact on the plot of N in Figure 14.31c at perihelion and aphelion because the Mercury g-value is minimized and both positive and negative deviations in radial velocity tend to increase the true g-value. Use of the Mercury-at-rest g-value therefore underestimates the true g-value, and the derived value of N_0 is too large. This effect yields an overestimate of the peak at perihelion seen in Figure 14.31c and creates a pseudo-peak at aphelion. A correction for this systematic error would be both a strong function of local time and model dependent (it depends on both the assumed temperature and the spatial distribution of the source), and therefore it is not straightforward to remove the g-value bias in the data. A more complete understanding of the seasonal variation in the calcium data requires a model that takes into account the motion of calcium atoms relative to Mercury.

Release from the surface followed by molecular photodissociation, first proposed by Killen et al. (2005), is often suggested as a process that can lead to the observed high temperatures for calcium. More recently, Killen and Hahn (2015) and Christou et al. (2015) showed that the calcium source rate observed by MESSENGER is consistent with micrometeoroid impact vaporization by dust supplied by the interplanetary dust disk and by comet 2P/Encke, respectively (Chapter 15).

Killen et al. (2016) ruled out photodissociation as the source of the energetic calcium: new results from the Burger et al. (2014) model showed that part of the calcium source is in the region behind the terminator, where photons do not have access. Instead, Killen suggested that the energetic calcium can be produced directly by impact vaporization for sufficiently energetic impactors.

14.4.4 Magnesium

Magnesium was first detected by the UVVS during MESSENGER's second flyby of Mercury (M2) on 6 October 2008 (McClintock et al., 2009). Figure 14.32 shows the magnesium image of the nightside tail region that was acquired by UVVS during approach. The magnesium image is more consistent with a uniform distribution than either sodium (Figure 14.17) or calcium (Figure 14.29). Fantail observations of magnesium, shown in Figure 14.18c, also support a nearly uniform distribution during both M2 and M3.

During M3, UVVS also measured profiles of magnesium emission versus altitude above the north and south poles
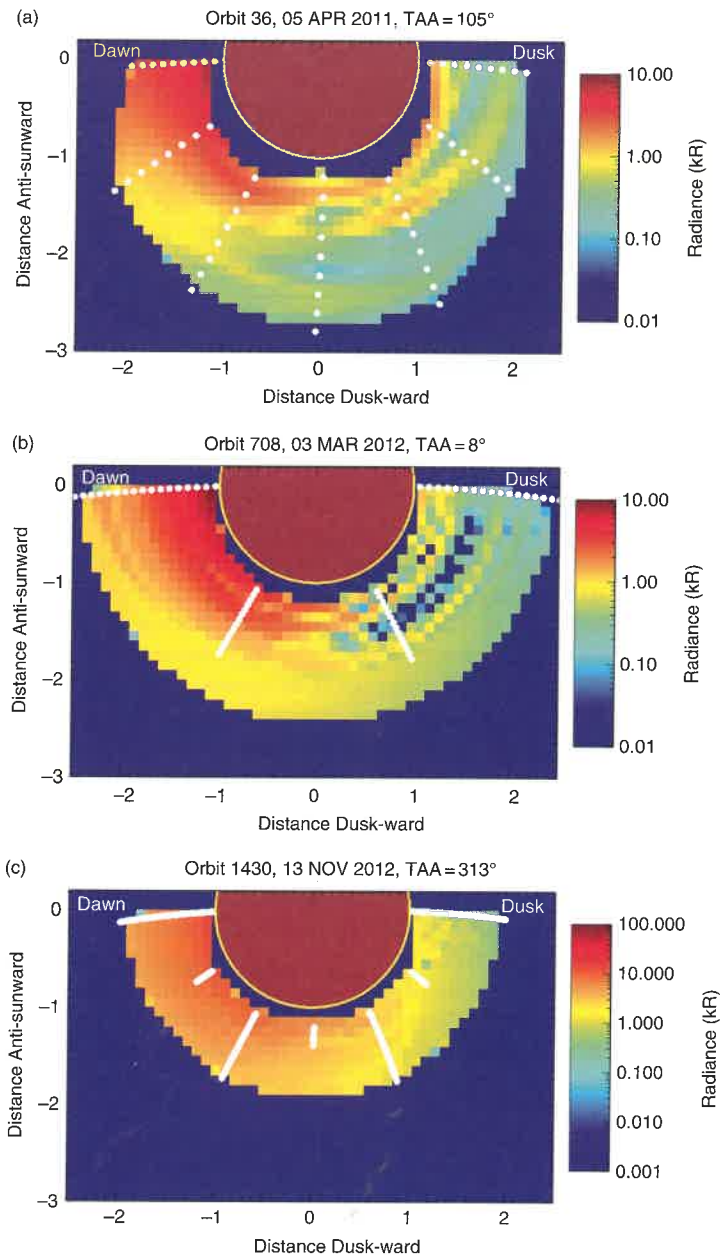
Figure 14.30. Images of calcium emission in Mercury's dayside equatorial plane at three epochs constructed by interpolating between MESSENGER limb emission profiles. The white circles show the projections of the line-of-sight tangent points in the equatorial plane. The color scale indicates the interpolated radiance. Mercury's sunlit hemisphere is shown. The dawn terminator is at the left side of the disk; the subsolar point is at the bottom. Adapted from Burger et al. (2014).

(Figures 14.19c and 14.19f). Vervack et al. (2010) fit an exponential function to the southern profile and reported an *e*-folding value of 2160 km. In the north, magnesium exhibited higher radiances, indicating larger release rates. Moreover, the magnesium profile above the north pole is strikingly different from a simple exponential. Vervack et al. (2010) suggested that this profile is indicative of additional source processes at work.

Chamberlain models fit to the flyby tail data (Killen et al., 2010; Sarantos et al., 2011) showed that the inferred magnesium density distribution could not be derived with a single source process. Rather, the combination of a hot source >20,000 K and a cooler source <5000 K was needed to adequately describe the magnesium distribution in the near and very far tail (Sarantos et al., 2011).

During the MESSENGER orbital phase, dayside limb scans of magnesium were observed at a systematic cadence. Merkel et al. (2017) analyzed a subset of these data from March 2013 to April 2015. Figure 14.33 illustrates their results for a typical sequence acquired on 12 August 2014 when Mercury's TAA was 77° (and when MESSENGER was in nearly a noon–midnight orbit).

The central image in Figure 14.33 summarizes the results, whereas separate plots represent the limb emission profiles and uncertainties at each local time. Maximum emission level decreased as the local time progressed toward dusk until the signal was near the noise level by local time 1800. The colored center figure represents the seven limb profiles projected onto the equatorial plane (viewed from the north) and interpolated to
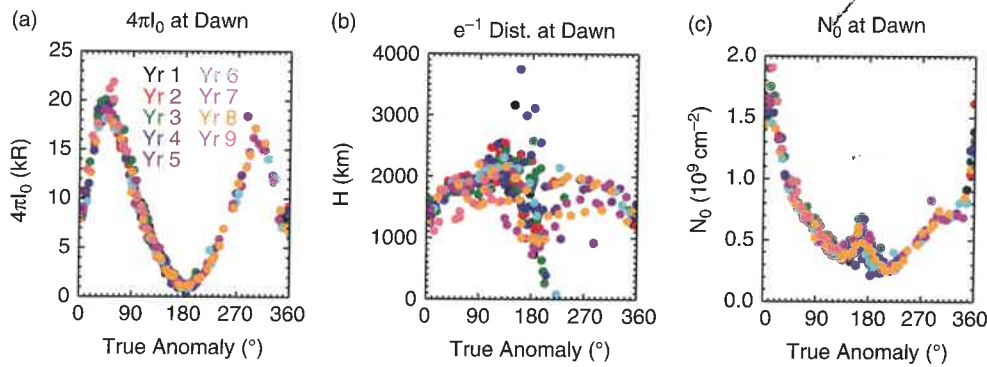
Figure 14.31. (a) Calcium 422.6-nm emission at the surface at Mercury dawn determined from exponential fits to the radial limb profiles. Different Mercury years are indicated by different colors. (b) The *e*-folding distance at dawn determined from the exponential fits. (c) Apparent tangent column density at dawn. A systematic error that creates the apparent peak near aphelion has been introduced by the assumption that all atoms are at rest relative to Mercury. Adapted from Burger et al. (2014).
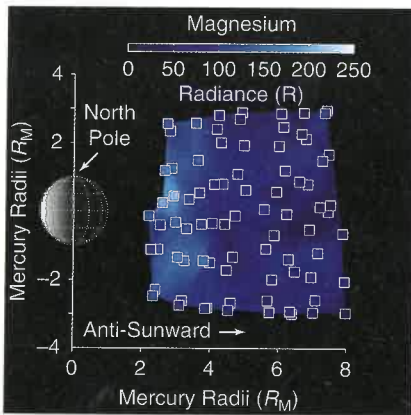

Figure 14.32. Emission from magnesium in Mercury's tail observed during M2. Individual observations (white squares) are overlaid on an image generated by projecting the observed line of sight onto the plane containing the spin axis and the Sun–Mercury line. Adapted from McClintock et al. (2009).

show the variation over local time, and it clearly shows an enhancement in emission in the morning.

Merkel et al. (2017) also investigated magnesium emission and column density as functions of local time and season (i.e., Mercury true anomaly). Figure 14.34a illustrates the distribution of dayside emission at a fixed altitude of 500 km versus true anomaly angle and local time. The data, which include observations acquired during approximately seven Mercury years, exhibit a prominent emission enhancement (maximum ~2.5 kR) on the dawn hemisphere near perihelion. Figure 14.34b illustrates the distinct seasonal pattern of the morning (0600–1000) enhancement in emission. Although there is some scatter, the seasonal pattern has a strong year-to-year repeatability. Figure 14.34c shows the distribution of column density at an altitude of 500 km versus true anomaly and local time. The seasonal variability has changed from that exhibited in the emission data, but the morning enhancement is maintained. Figure 14.34d shows that the peak in seasonal variability has shifted toward the inbound leg, which is related to the removal of the variation of the *g*-value over Mercury's orbit. The morning

dayside magnesium column density at 500 km ranged between 1×10^9 cm^{-2} and 8×10^9 cm^{-2}.

Merkel et al. (2017) fit Chamberlain models to the limb profile data in order to estimate the temperature and near-surface density of the magnesium exosphere. Example fits are shown in Figure 14.35. These examples represent the characteristic range of temperatures retrieved from data acquired during seven Mercury years. Retrieved temperature, temperature uncertainty, and χ^2 error for the fits are reported for each example. The blue dashed lines represent Chamberlain models with three different fixed temperature sources (5000, 10,000, and 20,000 K) as guides to compare with the data. Note that there is not much difference in slope between profiles for 10,000 K and 20,000 K. Because the hottest temperatures are difficult to constrain (Burger et al., 2014; Cassidy et al., 2015), Merkel et al. (2017) set an upper limit of 20,000 K. Although the flyby analysis (Sarantos et al., 2011) indicated the need for two distinct temperatures to characterize the data adequately, these examples show that the orbital-phase dayside limb profiles can be fit well with a only a single component.

The distributions of near-surface density and temperature versus Mercury's true anomaly angle and local time retrieved by Merkel et al. (2017) for the magnesium exosphere are shown in Figures 14.36a–14.36d. Figures 14.36b and 14.36d illustrate the seasonal variation of density and temperature for data taken between 0600 and 1000. Retrieved temperatures range between 3500 K and 20,000 K, with the average near ~6000 K at a small uncertainty. For ~15% of the time the temperatures are >10,000 K and typically occur near the terminators (e.g., Figure 14.35d). At the dawn terminator, the density and temperature solutions are robust; however, the data near 1800 local time are noisy and therefore less reliable. There is a small population of solutions that could not be constrained and are assigned the 20,000 K temperature limit. The majority of the retrieved temperatures are lower than 10,000 K and seem to be evenly distributed around all local times. There is little seasonal variation in temperature aside from a population of low temperatures near 90° TAA.

The distribution of the magnesium production rate versus true anomaly and local time is shown in Figures 14.36e and 14.36f. The production of magnesium is concentrated in the
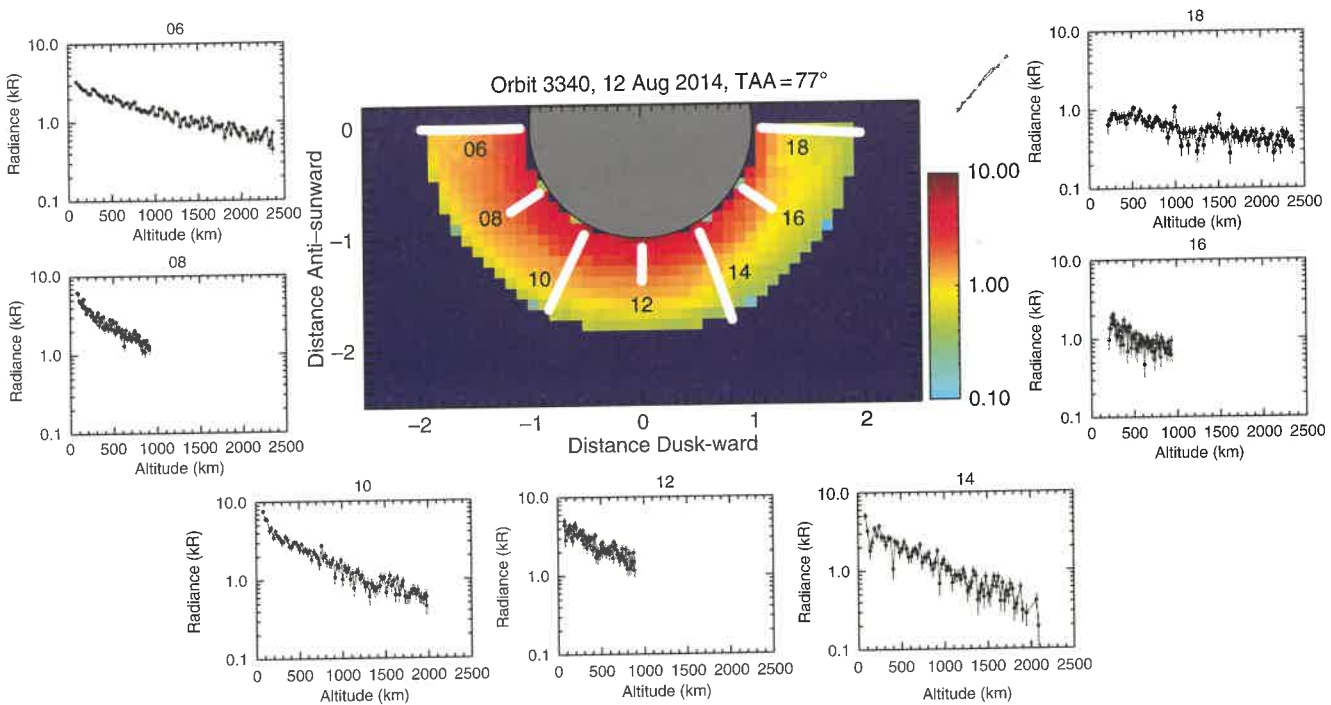
Figure 14.33. Example emission profiles for one orbit of the magnesium dayside limb-scan observations from MESSENGER. Seven local times were typically observed every third orbit throughout the orbit phase. The emission, in kR, is shown versus altitude at each local time on 12 August 2014, along with uncertainties. The color plot represents the limb emission profiles interpolated onto the equatorial plane (viewed from the north) and shows the local time variation over this orbit. The white lines represent the local time location and altitude range of each profile.
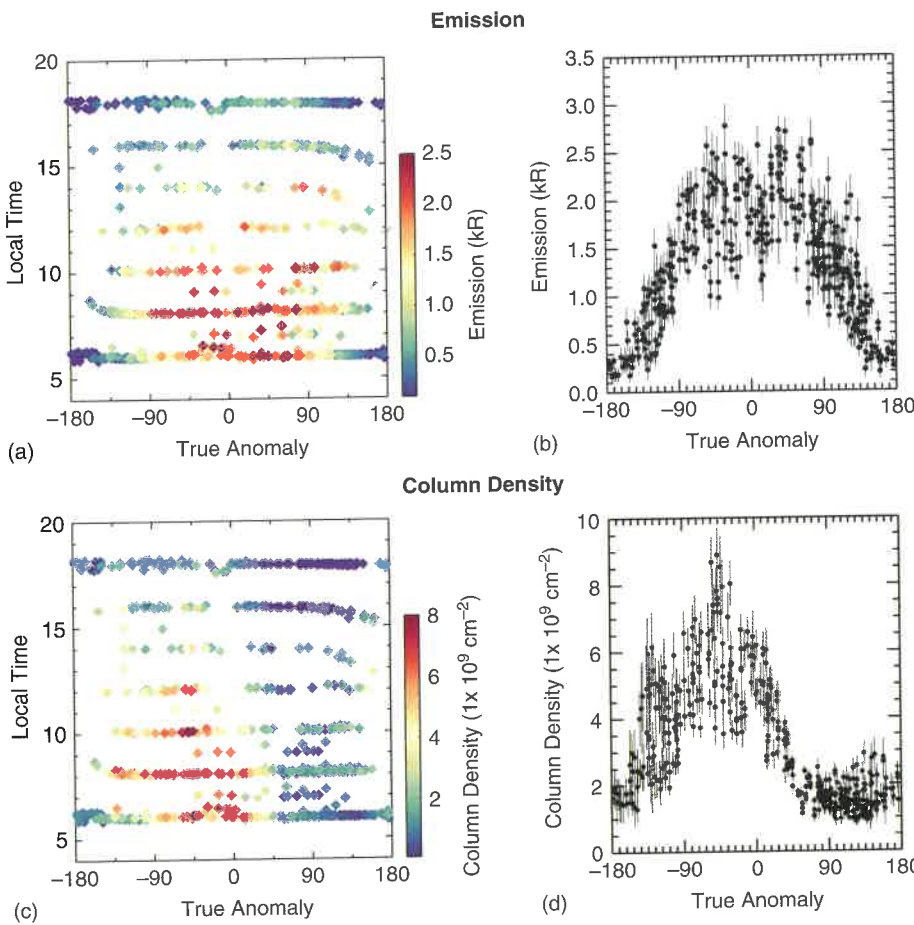

Figure 14.34. (a) and (c) Magnesium emission and column density, respectively, at 500-km altitude on the dayside as functions of Mercury true anomaly and local time (hours). The data encompass approximately seven Mercury years (March 2013–April 2015). (b) and (d) Plots of magnesium emission and column density, respectively, at local times 0600–1000 versus Mercury true anomaly illustrate the seasonal variation of the morning enhancement.
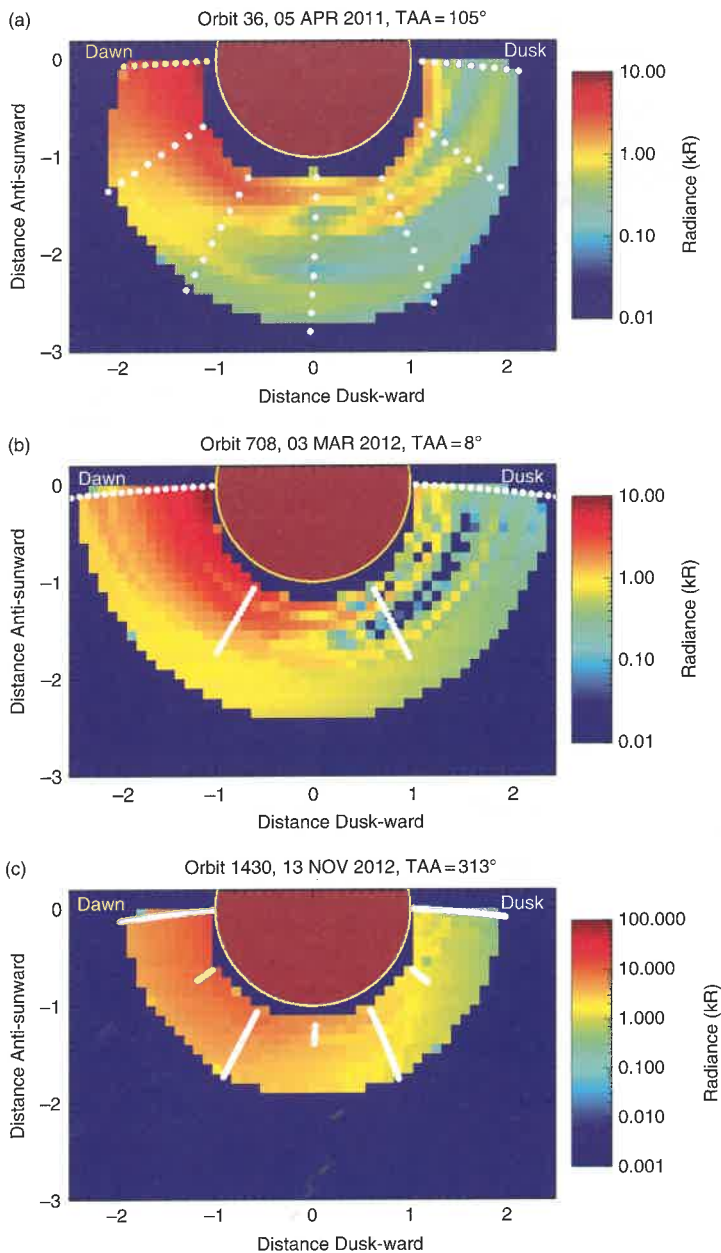
Figure 14.30. Images of calcium emission in Mercury's dayside equatorial plane at three epochs constructed by interpolating between MESSENGER limb emission profiles. The white circles show the projections of the line-of-sight tangent points in the equatorial plane. The color scale indicates the interpolated radiance. Mercury's sunlit hemisphere is shown. The dawn terminator is at the left side of the disk; the subsolar point is at the bottom. Adapted from Burger et al. (2014).

(Figures 14.19c and 14.19f). Vervack et al. (2010) fit an exponential function to the southern profile and reported an e-folding value of 2160 km. In the north, magnesium exhibited higher radiances, indicating larger release rates. Moreover, the magnesium profile above the north pole is strikingly different from a simple exponential. Vervack et al. (2010) suggested that this profile is indicative of additional source processes at work.

Chamberlain models fit to the flyby tail data (Killen et al., 2010; Sarantos et al., 2011) showed that the inferred magnesium density distribution could not be derived with a single source process. Rather, the combination of a hot source >20,000 K and a cooler source <5000 K was needed to adequately describe the magnesium distribution in the near and very far tail (Sarantos et al., 2011).

During the MESSENGER orbital phase, dayside limb scans of magnesium were observed at a systematic cadence. Merkel et al. (2017) analyzed a subset of these data from March 2013 to April 2015. Figure 14.33 illustrates their results for a typical sequence acquired on 12 August 2014 when Mercury's TAA was 77° (and when MESSENGER was in nearly a noon–midnight orbit).

The central image in Figure 14.33 summarizes the results, whereas separate plots represent the limb emission profiles and uncertainties at each local time. Maximum emission level decreased as the local time progressed toward dusk until the signal was near the noise level by local time 1800. The colored center figure represents the seven limb profiles projected onto the equatorial plane (viewed from the north) and interpolated to
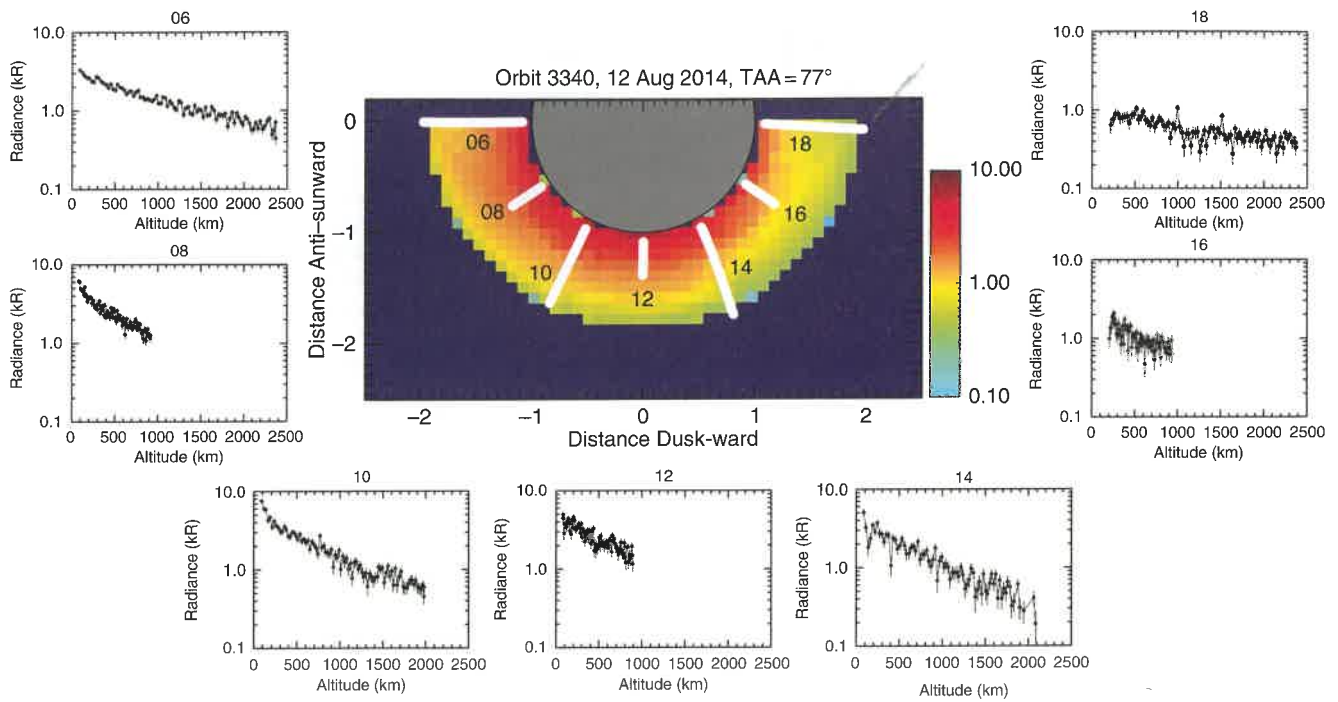
Figure 14.33. Example emission profiles for one orbit of the magnesium dayside limb-scan observations from MESSENGER. Seven local times were typically observed every third orbit throughout the orbit phase. The emission, in kR, is shown versus altitude at each local time on 12 August 2014, along with uncertainties. The color plot represents the limb emission profiles interpolated onto the equatorial plane (viewed from the north) and shows the local time variation over this orbit. The white lines represent the local time location and altitude range of each profile.

Figure 14.34. (a) and (c) Magnesium emission and column density, respectively, at 500-km altitude on the dayside as functions of Mercury true anomaly and local time (hours). The data encompass approximately seven Mercury years (March 2013–April 2015). (b) and (d) Plots of magnesium emission and column density, respectively, at local times 0600–1000 versus Mercury true anomaly illustrate the seasonal variation of the morning enhancement.
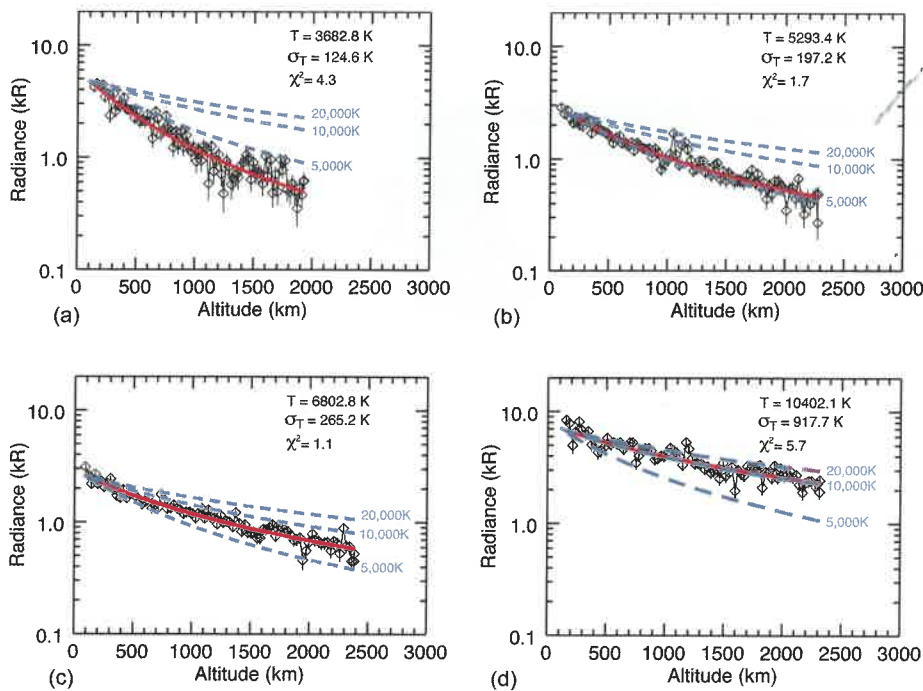
Figure 14.35. Examples of Chamberlain models fit to magnesium dayside limb profiles. The black diamonds are the emission data with one-standard-deviation uncertainties. The blue dashed lines represent Chamberlain models at three different fixed temperatures as guides to compare with the data. The red line gives the best fit in each case. The retrieved temperature, the temperature uncertainty σ_T, and the χ^2 error estimate are included in the right-hand corner of each panel.

morning and predominantly on the inbound leg of Mercury's orbit. Production is mostly influenced by surface density, as seen by the similarity between the seasonal variation in the two quantities shown in Figures 14.36b and 14.36e. The production of magnesium is enhanced in the morning, with the largest peak on the inbound leg (315°) and a smaller peak on the outbound leg (~140°) with rates ranging from 2×10^5 cm^{-2} s^{-1} to 8×10^5 cm^{-2} s^{-1}.

Whereas the analyses of MESSENGER's flyby data of the magnesium tail provided evidence for two sources – a lower-energy source with temperature < 5000 K and a higher energy source with temperature > 20,000 K (Sarantos et al., 2011) – Merkel et al. (2017) concluded that the observed enhanced production rate in the morning and mean temperatures near ~6000 K are most consistent with impact vaporization as the source of the dayside magnesium exosphere. However, they noted that a relatively high-energy source ($T > 10,000$ K) was retrieved 15% of the time near the dawn terminator, which is in agreement with the higher-energy source inferred from the MESSENGER flyby tail data (Killen et al., 2010; Sarantos et al., 2011). A hotter source at the dawn terminator is reminiscent of the hot dawn-enhanced calcium distribution described above. Contrary to the situation for calcium, there is no evidence so far for a comet stream as a possible source process, as discussed by Killen and Hahn (2015). However, Merkel et al. (2018) provided evidence that the production and distribution of magnesium in the exosphere is related to the distribution of magnesium on Mercury's surface.

14.4.5 Additional Species

Searches for additional species in Mercury's exosphere have been conducted from the ground, by Mariner 10, and by MESSENGER. These species are more difficult to observe than species such as sodium and calcium, because they either emit more weakly or are less abundant in Mercury's exosphere. Nevertheless, several such species have been detected in Mercury's exosphere and are discussed in this section.

14.4.5.1 Hydrogen

Mariner 10 Observations

Hydrogen in Mercury's exosphere was first detected by the UVS on Mariner 10 (Broadfoot et al., 1974; Shemansky and Broadfoot, 1977). These observations revealed two interesting features in Mercury's hydrogen exosphere distribution, which are illustrated in Figure 14.37. The first was a "bump" near 200-km altitude that may have been an instrumental artifact (Hunten et al., 1988). The second was the two-component nature of the distribution. A "warm" component had a scale height associated with dayside temperatures (420 K), whereas the other component was consistent with nightside temperatures (110 K) (Shemansky and Broadfoot, 1977). Unfortunately, the geometry of the Mariner 10 observations did not allow for measurement of the hydrogen profile at points other than normal to the subsolar longitude, so little else was learned about the distribution of hydrogen about the planet from that mission.

MESSENGER Observations

Measurements of the hydrogen distribution over the subsolar point during the first two MESSENGER flybys of Mercury, reported by Vervack et al. (2010), are compared with the most extended Mariner 10 hydrogen profile in Figure 14.38. In general, the UVVS and Mariner 10 profiles are quite similar in structure, but the UVVS radiances are uniformly higher than the Mariner 10 values. These overall higher hydrogen radiances
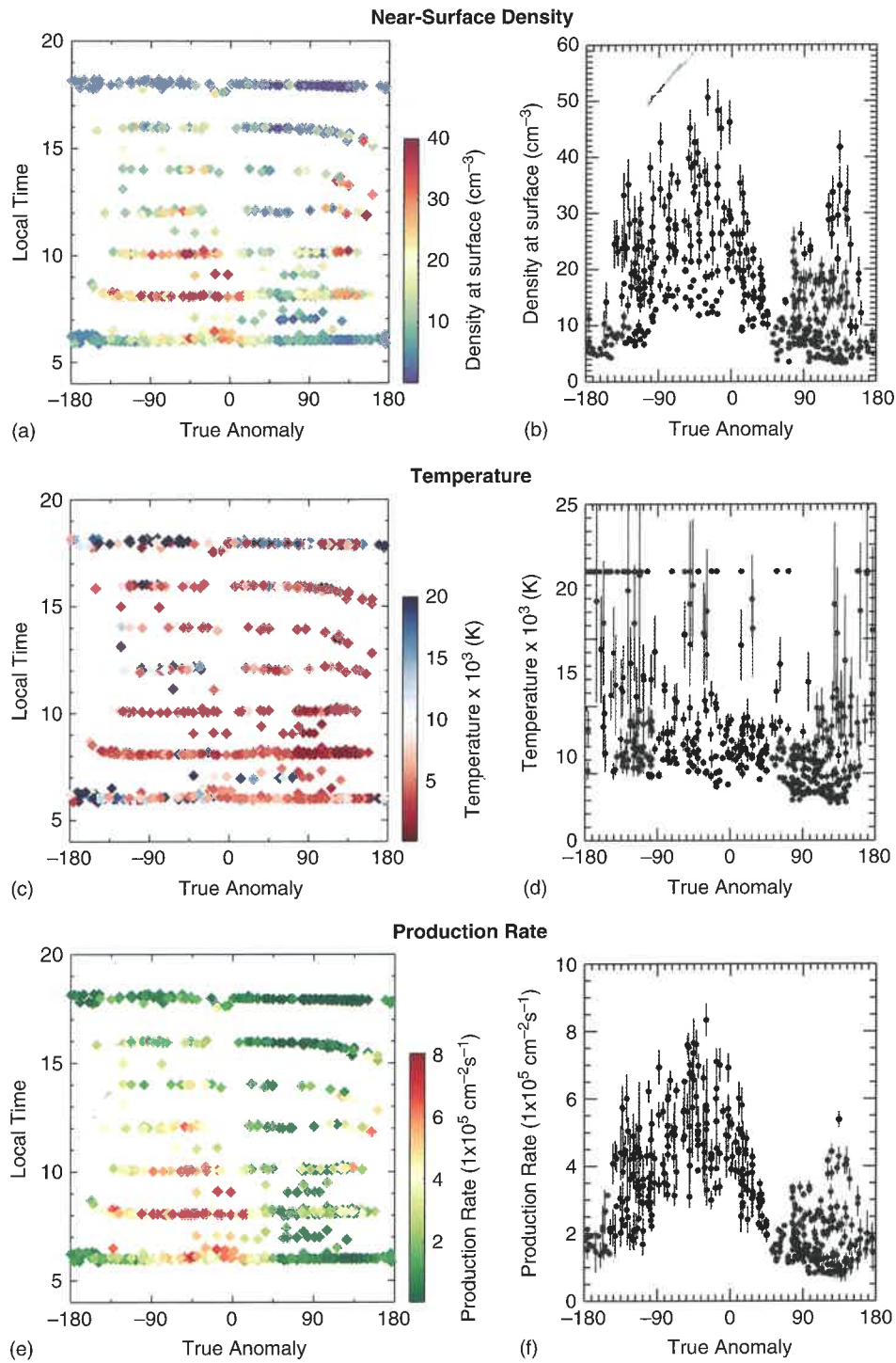
Figure 14.36. (a) and (b) Magnesium near-surface density, (c) and (d) temperature, and (e) and (f) production rate as functions of Mercury true anomaly and local time (hours). The data encompass approximately seven Mercury years (March 2013–April 2015). The right panels show the seasonal variation of the results for morning local times (0600–1000).

observed by UVVS relative to the Mariner 10 data may have several causes, including differences in viewing geometry (the Mariner 10 UVS slit subtended a much larger range of latitudes than did the UVVS), instrument calibration, incident solar flux, removal of the background interplanetary hydrogen component, and exospheric hydrogen density. Adopting a range of 100–300

rayleighs as the maximum profile radiance results in a near-surface line-of-sight column density between $\sim 8 \times 10^9 \, \text{cm}^{-2}$ and $\sim 2.4 \times 10^{10} \, \text{cm}^{-2}$ for $g \sim 1.25 \times 10^{-2}$ photons atom^{-1} s^{-1} (Killen et al., 2009).

Vervack et al. (2009) fit a range of Chamberlain models to the UVVS data (Figure 14.38). Their resulting values of

temperature and surface density, n_0, are shown for each flyby. Vervack et al. (2009) also noted that relatively large radiance values were measured during M2 at high latitude in the altitude range between 2500 and 3500 km. They postulated that these could have resulted from larger hydrogen densities there, possibly as a result of magnetospheric influences. Alternatively, they argued that the equatorial region may be depleted in hydrogen because of greater desorption near the subsolar point.

The flyby data were not suitable for searching for the cold component observed by Mariner 10. Instead, Vervack et al. (2011) used profiles measured during the orbital phase of the 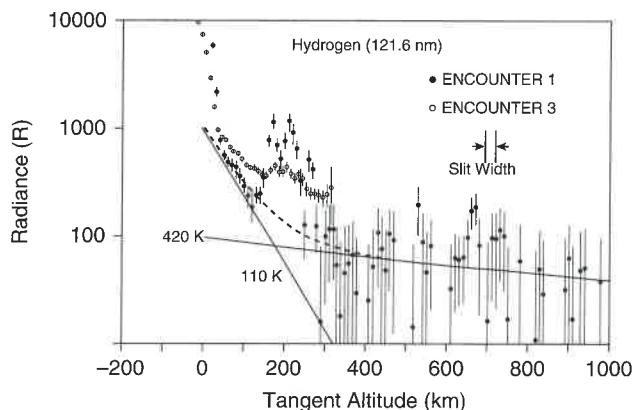MESSENGER mission, which have much better spatial resolution, to further investigate this feature of the Mariner 10 distribution. Figure 14.39 illustrates the better altitude resolution of the orbital profiles, and it suggests that there may in fact be a "cold" component to the distribution. Vervack et al. (2011) pointed out that sunlight scattered into the UVVS telescope from the planet's surface can mimic a cold component, and any possible artifact resulting from this effect had not been removed from their data. Thus the existence of a cold component has not been conclusively verified with MESSENGER observations. To date, no evidence has been found in the UVVS data that matches the bump in the Mariner 10 profiles.

14.4.5.2 Helium

Helium is the exospheric species best measured by Mariner 10. Numerous scans across the disk and above the limb were carried out for the helium 58.4-nm emission, an example of which is shown in the left panel of Figure 14.5. Attempts to model the distribution (left panel), which led to predictions of an antisolar/subsolar density ratio near 200 depending on the source velocity (e.g., Smith et al., 1978), failed to match the observed value of 50 inferred from the terminator region.

Also measured was the profile of emission above the subsolar point (Figure 14.40). Unlike the case for hydrogen, the helium distribution appears to correspond to a single component exhibiting dayside temperatures. The near-surface line-of-sight column density inferred from the maximum 100 rayleigh signal is ~2.5×10^{12} cm^{-2} for $g \sim 4 \times 10^{-5}$ photons atom^{-1} s^{-1} (Killen et al., 2009). UVVS did not cover the wavelengths of helium emission. However, models of the He$^+$ distribution measured by FIPS may eventually provide constraints on the distribution of neutral He.

Figure 14.37. Profile of the H Lyman α emission measured normal to the subsolar point during two of the Mariner 10 flybys. The profile is fit with a two-component model, one with a temperature close to the dayside temperature (420 K) and one with a temperature close to that of the nightside (110 K). The bump near 200 km is a mystery. Adapted from Hunten et al. (1988).
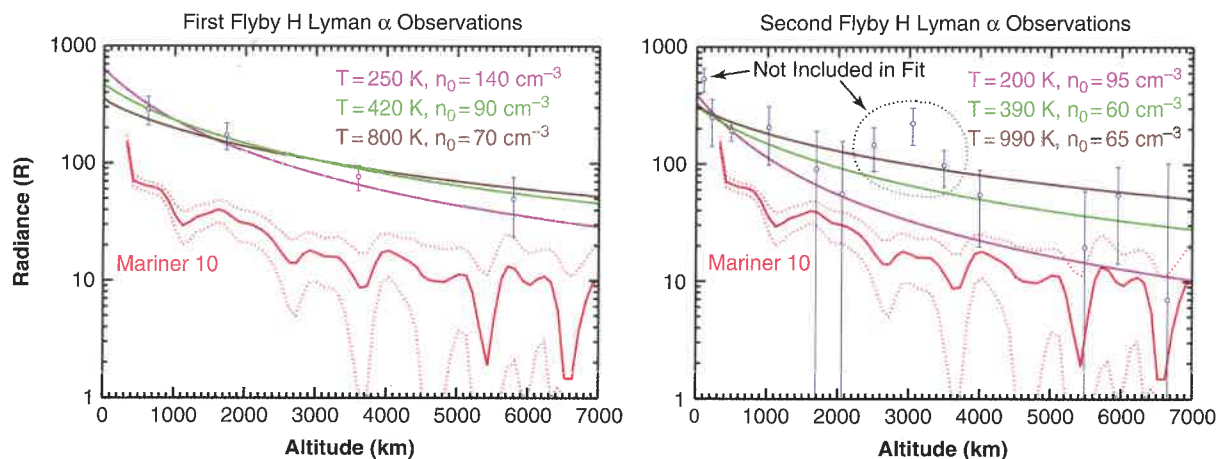

Figure 14.38. Hydrogen Lyman α radiances (corrected for background interplanetary H emission) measured by the MESSENGER UVVS (Vervack et al., 2009) compared with radiances obtained during the first Mariner 10 flyby (Broadfoot et al., 1976). The UVVS data have been binned in altitude (averages over 0–1000 km, 1000–2500 km, 2500–4500 km, and >4500 km for M1 and averages centered on multiples of 500 km for M2). Chamberlain models fit to the data are shown for both M1 and M2. The green curves are "nominal" models. For M2, this is the best fit to the data. The sparseness of the altitude sampling and large bin sizes for M1 rendered the fits unreliable, and a 420 K model is shown as representative. The magenta and brown curves are visually estimated limiting cases. Three points between 2500- and 3500-km altitude were excluded from the fit for M2 because they were obtained during times when the spacecraft pointed to high latitudes for operational reasons.
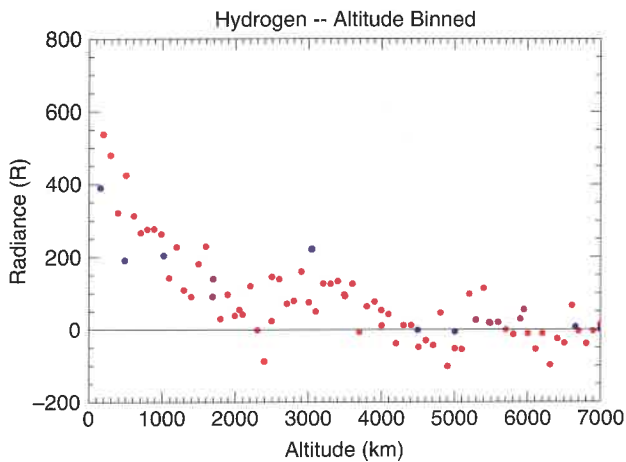
Figure 14.39. Comparison of the H distribution measured during MESSENGER's second Mercury flyby and binned in altitude to multiples of 500 km (blue circles) with a typical H profile measured over the subsolar point during the MESSENGER orbital phase (red circles). The orbital profile has been binned into 100-km-wide altitude bins.
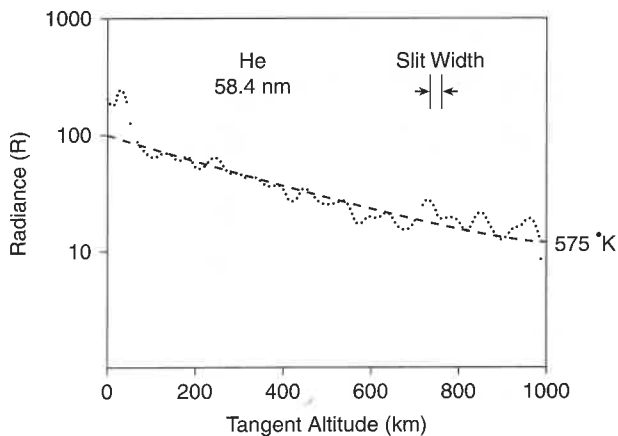

Figure 14.40. Altitude profile of helium 58.4 nm emission above the subsolar point from Mariner 10. Dots indicate measured radiance values, and the dashed line is a single-temperature Monte Carlo model. Adapted from Broadfoot et al. (1976).

14.4.5.3 Oxygen

During the third Mariner 10 flyby, a detection of 130.4-nm oxygen emission was reported (Broadfoot et al., 1976). However, high noise levels precluded measurement of a profile, and the actual level of the detection was uncertain (63–200 rayleighs) (Broadfoot et al., 1976; Hunten et al., 1988). The inferred Mariner 10 oxygen column density ($\sim 3 \times 10^{11}$ cm^{-2}) in the exosphere is comparable to that of sodium ($\sim 2 \times 10^{11}$ cm^{-2}).

Searches for oxygen 130.4-nm emission with UVVS were regularly conducted throughout the orbital phase, but no convincing detection was found. Vervack et al. (2016) reported that levels of oxygen emission consistent with those reported for Mariner 10 would have easily been seen by UVVS. A typical example of a dayside spectrum, taken from Vervack et al. (2016), is illustrated in Figure 14.41.
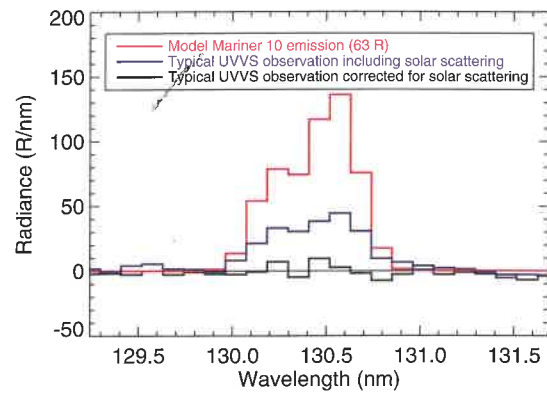

Figure 14.41. Example of a typical MESSENGER observation of the O 130.4-nm emission region. The blue line denotes the observed spectrum, which includes a solar scattered component from the surface. The black line is this spectrum after removal of the solar scattering. For this spectrum, the one-standard-deviation upper limit for emission is 2 R. The red line is a model spectrum of 130.4-nm emission corresponding to 63 R, which is the lower bound of the Mariner 10 detections. Thus, the UVVS upper limits are typically a factor of 30 less than the reported Mariner 10 detection.

They estimated that the one-standard-deviation upper limit for oxygen emission in the example observation is 2 rayleighs, which corresponds to a tangent column density of 2×10^{10} cm^{-2} and is an order of magnitude less than a typical sodium value.

14.4.5.4 Aluminum

From observations of the 396.152-nm emission line for aluminum acquired at the New Technology Telescope at La Silla, Chile, Doressoundiram et al. (2009) reported an upper limit for aluminum in Mercury's exosphere of 7.8×10^9 cm^{-2} (but they referred to this limit as a "tentative detection"); their observations are shown in Figure 14.42. Observations of aluminum made with the HIRES spectrometer on the Keck I telescope were reported by Bida and Killen (2011, 2016), who claimed measurements of the aluminum 396.152-nm emission at a four-to-five-standard-deviation level during runs in 2008 and 2013. Bida and Killen (2016) reported tangent columns of $(2.5–5.1) \times 10^7$ cm^{-2} over altitudes 860–2100 km, significantly lower than the figure reported by Doressoundiram et al. (2009). The scale height of the aluminum gas is consistent with a kinetic temperature of 4800–6900 K.

Searches for minor species conducted by the MESSENGER UVVS during dayside limb scans and nightside tail sweeps were unsuccessful. Nonetheless, aluminum (as well as ionized calcium and manganese; see below) was detected in the pre-dawn nightside region of the planet (0200–0500) over the TAA range 0°–70° during ride-along observations with FIPS (Vervack et al., 2016) that used the specialized viewing geometry illustrated in Figure 14.43. Similar geometries at other times in the orbital phase of MESSENGER did not reveal these species, so there may be substantial variability in their distributions both spatially and/or temporally.
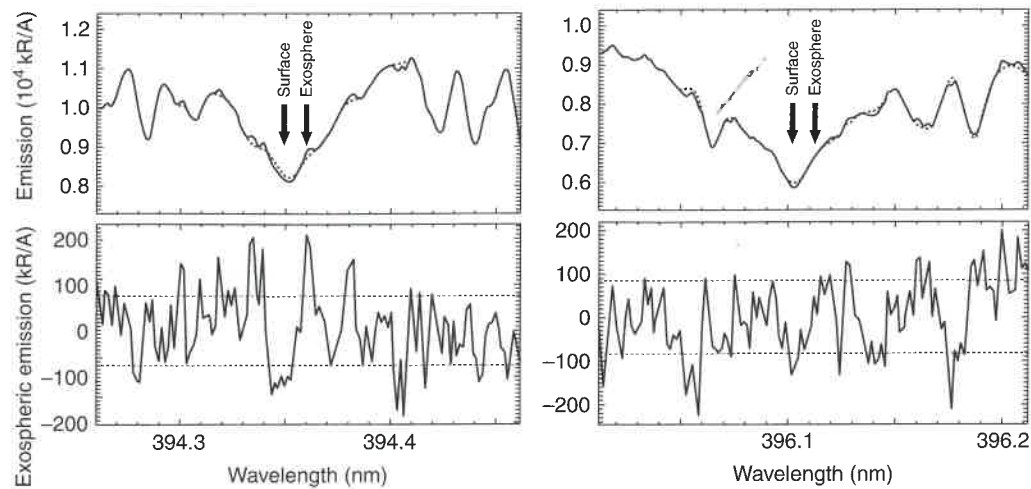
Figure 14.42. Spectra of the Al 394.4 nm (left upper panel) and 396.1 nm (right upper panel) resonant emission lines as measured in Mercury's exosphere. The positions of the exospheric line and of the solar absorption line reflected at Mercury's surface as expected from the planetary ephemeris are also indicated. A solar spectrum has been reduced in resolution, scaled to the measured spectra, and plotted as a dotted line. Left and right lower panels are differences between the measured spectra and the modified solar spectra in the panels above. The dashed horizontal lines on the lower panels indicate the one-standard-deviation level. From Doressoundiram et al. (2009).
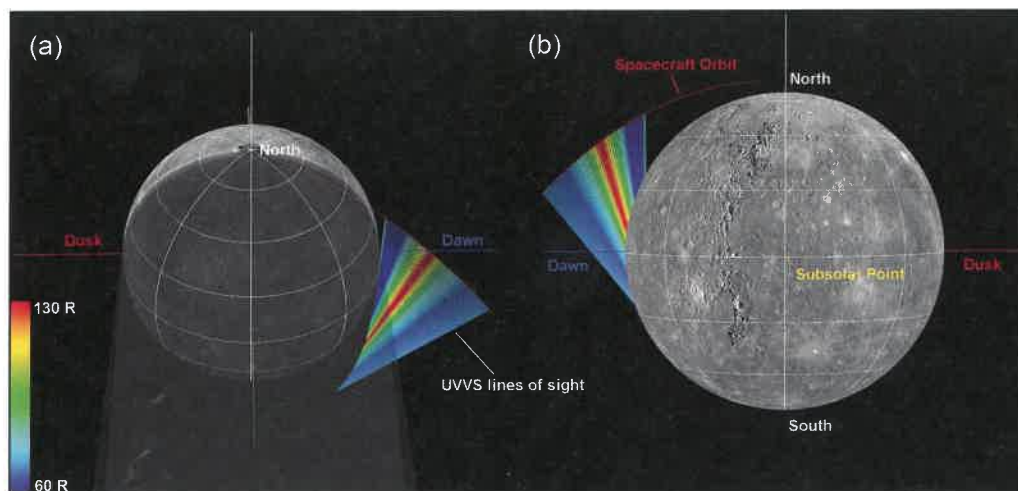

Figure 14.43. MESSENGER observation geometry for the aluminum, ionized calcium, and manganese observations. North is up in these panels, and the observations were made on the dawn side of the planet. The red arc represents the spacecraft orbit, and the spacecraft motion was from north to south (moving away from the planet). The colored lines from the spacecraft positions represent the UVVS line of sight for each spectrum, with the color scale indicating the radiance of the ionized calcium 393.48-nm line. These lines terminate at the line-of-sight tangent point for each observation. The left panel illustrates that the line of sight started in a north–south orientation (looking south) and then rotated during the observational sequence to end up pointing in a direction that is more oriented in the tail direction. The right panel illustrates that a portion of the lines of sight were in Mercury's shadow during most of the observation.

An example of one such observation displaying emissions from two lines of aluminum and two lines of ionized calcium (discussed below) is shown in Figure 14.44. The high signal-to-noise ratio of the UVVS measurements and the observation of two lines provide definitive confirmation of the presence of aluminum in Mercury's exosphere. Figure 14.45 shows the radiance in the two aluminum lines observed by UVVS as a function of tangent altitude. The

Chamberlain formalism cannot be reliably applied to these data because the UVVS line of sight was in constant motion owing to spacecraft maneuvers so that it skirted Mercury's shadow rather than drifting in altitude. Vervack et al. (2016) converted their average radiance value to column density to provide an approximate estimate of 7.7×10^7 cm^{-2}, in reasonable agreement with the line-of-sight column densities reported by Bida and Killen (2016).
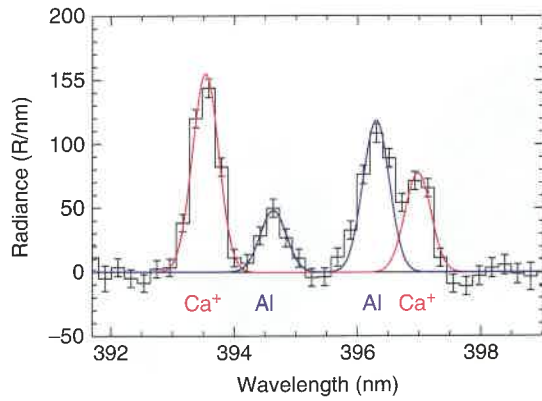
Figure 14.44. A MESSENGER spectrum of an observation of aluminum and ionized calcium with one-standard-deviation errors. The background-subtracted spectrum has been averaged over the altitude range 200–700 km to enhance the signal-to-noise ratio. That the two lines of each species are in the ratios expected provides clear evidence that these species have been detected.
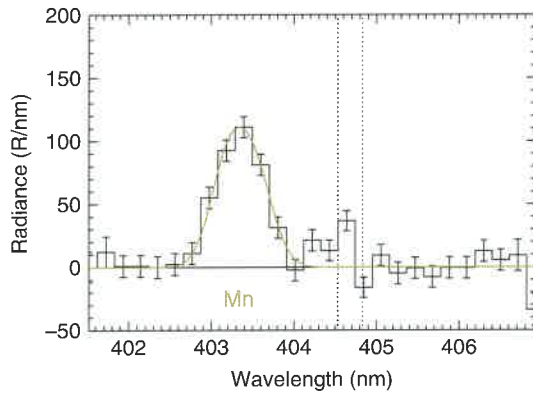

Figure 14.46. A MESSENGER spectrum for one of the observations of manganese, which has been averaged over the altitude range 200–320 km and background-subtracted, is shown with one-standard-deviation error bars. The three lines of the triplet are not individually resolved but sum to produce a "line" that is wider than the standard UVVS line shape. The evidence for potassium emission near 404–405 nm (vertical dotted lines) is not conclusive.

14.4.5.5 Ionized Calcium

Emission from ionized calcium was first detected in Mercury's exosphere during the third MESSENGER flyby (Vervack et al., 2010). The ions were observed at approximately $(1–2)\,R_M$ tailward of the planet and mostly near the equatorial plane. Because velocities for ionized calcium are generally much larger than those for neutral calcium and the line-of-sight column density estimates for ionized calcium and neutral calcium $(1–2)\,R_M$ downtail were of the same order of magnitude, it was determined that local production of ionized calcium from calcium was unlikely to yield the observed ionized calcium distribution. Instead, Vervack et al. (2010) concluded that a combination of magnetospheric convection and centrifugal acceleration, channeling ionized calcium produced elsewhere into the tail region, was required to account for the distribution (Gershman et al., 2014).
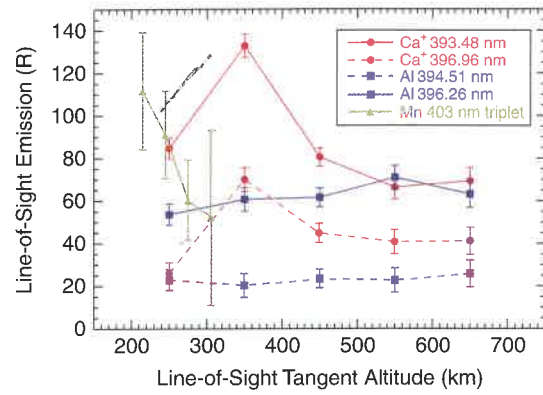

Figure 14.45. Profiles of aluminum, ionized calcium, and manganese radiance as functions of tangent altitude from one observation sequence. The different curves for aluminum and ionized calcium are for the two lines detected. The profile for manganese is the sum over the three lines of the triplet.

Vervack et al. (2016) also observed two lines of ionized calcium during the same observations from which aluminum was detected by UVVS (Figure 14.44). These later observations confirmed the presence of detectable ionized calcium emission from Mercury's exosphere. Figure 14.45 shows the radiance profiles for the ionized calcium lines as a function of tangent altitude. These profiles exhibit different altitude distributions from those of aluminum over the same observation geometries, suggesting differences in their source and loss processes. Vervack et al. (2016) reported an average line-of-sight column density of 3.1×10^7 cm^{-2} for the viewing geometry shown in Figure 14.43.

Although the wavelengths of the two ionized calcium lines detected by UVVS can be observed from the ground, attempts to do so have thus far yielded only upper limits. Bida and Killen (2016) reported three-standard-deviation upper limits near Mercury's equatorial antisolar limb, from which a column density limit of 3.9×10^6 cm^{-2} at 1630-km altitude was derived.

14.4.5.6 Manganese

Manganese was an unexpected constituent of the exosphere that was also detected during near-dawn observations reported by Vervack et al. (2016). It was added to the UVVS search list because it has a high neutron absorption cross section, so its presence on the surface could influence the interpretation of MESSENGER Gamma-Ray and Neutron Spectrometer data (Evans et al., 2012). MESSENGER X-Ray Spectrometer data also revealed Mn to be present on Mercury's surface (Nittler et al., 2011; Chapter 2). Figure 14.46 shows an average spectrum of the manganese triplet near 403 nm. This robust detection is clear evidence for manganese in Mercury's exosphere. The radiance profile as a function of altitude, shown in Figure 14.45, exhibits distinct differences from the profiles for aluminum and ionized calcium. These differences suggest that different processes control manganese, aluminum, and ionized calcium in Mercury's exosphere (Chapter 15). Vervack et al. (2016) reported a value of 4.9×10^7 cm^{-2} for the average
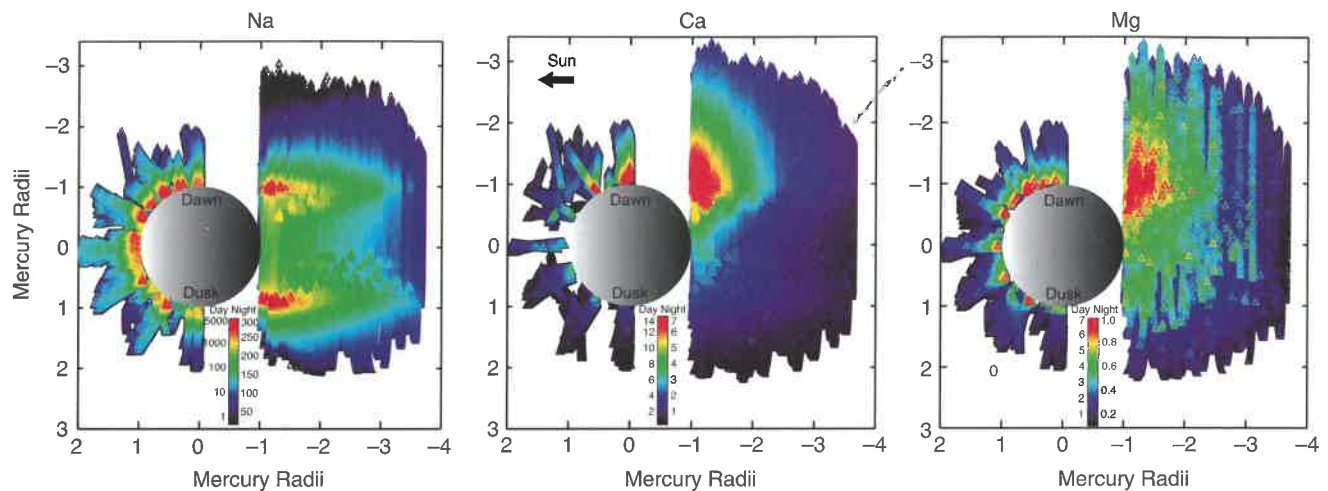
Figure 14.47. Geometrical representation of emission (in kR) from sodium, calcium, and magnesium during the orbital phase of the MESSENGER mission. These plots illustrate the two types of systematic observations (as shown in Figure 14.8) used to measure these constituents on Mercury's dayside and nightside. The color scaling is specific to each species, and scaling for daytime observations is different from that for nighttime observations. Each species has a different region of localized enhanced brightness.

column density with a viewing geometry similar to that shown in Figure 14.43.

14.4.5.7 Other Species

A number of other species have been sought in Mercury's exosphere. Doressoundiram et al. (2009) reported upper limits for iron, lithium, and silicon of 1×10^{11} cm^{-2}, 4×10^7 cm^{-2}, and 5×10^{10} cm^{-2}, respectively, on the basis of averages of observations acquired during the nights of 30–31 October 2005. Bida and Killen (2016) reported a single three-standard-deviation detection of iron from HIRES observations at the Keck I Observatory in 2009. With the same simple model as that employed for their aluminum observations, they found a zenith column density of 8.2×10^8 cm^{-2}. The scale height of the iron gas is consistent with a kinetic temperature of 5000–13,000 K. Although sought on numerous occasions, including in concert with the observations that yielded detections of aluminum and ionized calcium, iron was not observed by UVVS.

14.5 SUMMARY

Mercury's exosphere was discovered in 1974 when the UVS experiment on the Mariner 10 spacecraft detected hydrogen and helium about the planet. This result was followed by the first measurements of Mercury's sodium and potassium exospheres by Potter and Morgan (1985, 1986) and by the detection of calcium by Bida et al. (2000). Several groups have imaged the sodium exosphere with ground-based telescopes equipped with high-resolution spectrographs. These images have revealed a dynamic exosphere with localized enhancements in intensity (by tens of percent) at high latitudes that appear and disappear on timescales of hours. These variations are thought to result from the impact of solar-wind ions that penetrate Mercury's magnetosphere at its cusps. However, attempts to correlate such variations with interplanetary magnetic field

measurements at Mercury made by the MESSENGER Magnetometer have been inconclusive (Section 14.4.1.1). Although ground-based observers can observe localized changes (analogous to weather patterns on Earth) in global-scale images of Mercury's exosphere, Mercury orbits too close to the Sun to allow ground-based synoptic studies of exospheric behavior as a function of TAA or to allow simultaneous observations of both terminators. Moreover, detailed ground-based studies of Mercury's exosphere have been limited primarily to sodium. Only a few potassium images have been acquired, and calcium observations are limited to a small number of long-slit spectra acquired at the Keck Observatory.

During its orbital phase, MESSENGER provided the first high-spatial-resolution synoptic measurements of Mercury's sodium, calcium, and magnesium exospheres. These observations revealed three distinct spatial distributions, each with its own characteristic temperature structure. Figure 14.47 illustrates the spatial distributions of sodium, calcium, and magnesium about the planet made by superimposing all the observations of these species made between March 2014 and March 2015 in the TAA range 0°–90°. Whereas sodium is more or less uniformly distributed over the dayside and symmetric about Mercury's shadow at night, calcium emission exhibits a strong dawn–dusk asymmetry. The magnesium distribution is similar to that of calcium, except that the dayside emission is distributed over a larger range of local time (0600–1000) and the dawn–dusk contrast is less pronounced.

MESSENGER's orbit allowed the UVVS to monitor the seasonal variation in Mercury's exosphere (analogous to seasonal climate variations on Earth). From nearly 12 Mercury years in orbit, UVVS measurements of intensity distributions of sodium and calcium as functions of TAA remained constant within the errors of the measurements (Figures 14.20 and 14.28). This constancy was also true for magnesium, but the data were limited to only the last seven years in orbit (Figure 14.31). Individual temperature distributions for each species

showed little variation with TAA and were also stable from year to year. Whereas sodium temperature values were near 1200 K, suggesting that photon-stimulated desorption is a dominant surface release process (Cassidy et al., 2015), and magnesium temperatures of 6000 K are consistent with impact vaporization, calcium's more extreme temperature, near 50,000 K, suggests that more complex processes contribute to the calcium exosphere.

In general, MESSENGER sodium measurements are consistent with and complementary to ground-based observations. Although there is no evidence for short time variations in the MESSENGER data, this result is most likely due to limitations on the observation geometry imposed by the spacecraft orbit and pointing constraints. These constraints generally restricted observations to occur near orbit apoapsis (Figure 14.8) and limited the latitude of the tangent point to lie within ±30° of the equator (Figure 14.9). In this configuration, the line of sight passed above the magnetospheric cusps at very high altitudes, where the local densities are vanishingly small. Further, UVVS observed a small number of discrete local times with a cadence of 12 h before apoapsis was lowered and MESSENGER's orbital period was reduced to 8 h. In both orbits, changes in observed intensity were aliased with changes in viewing geometry. On the other hand, the lack of a cold sodium component (Figure 14.22) agues that thermal desorption, thought to be an important release mechanism on the basis of pre-MESSENGER work (Killen et al., 2007; Leblanc and Johnson, 2010; Mura et al., 2009), is not an important surface-release process.

Several weakly emitting species have now been identified about Mercury. Tentative ground-based identifications of aluminum have been confirmed by MESSENGER observations. Manganese and ionized calcium have also been discovered by MESSENGER. The limited number of detections suggests that their spatial distributions and dependence on TAA are different from those of routinely observed species and are possibly highly time-variable, but there are too few measurements to make definitive conclusions. Both Mariner 10 and MESSENGER observed hydrogen about Mercury. Whereas both investigations measured similar temperature distributions, the inferred hydrogen column densities by MESSENGER are about a factor of 4 larger than those by Mariner 10. MESSENGER did not confirm the tentative identification of oxygen by Mariner 10.

The total inventory of confirmed exospheric neutral species is nine. Of these, helium and sodium dominate, exhibiting near-surface line-of-sight column densities in the range 10^{11} cm^{-2}–10^{12} cm^{-2}. Magnesium and hydrogen are about a factor of 10 less abundant, potassium and calcium are about a factor of 100 less abundant, and the minor species aluminum and manganese are less abundant by factors near 10,000. The MESSENGER upper limit for oxygen places it with magnesium and hydrogen; however, this limit is not particularly strong because oxygen resonance lines occur near 130 nm and have very small *g*-values. This situation also holds for sulfur, an element that is abundant in Mercury's surface material (Chapter 2). Placing the observations of ionized species of calcium (UVVS) and sodium and oxygen (FIPS) in context with the neutral species is not straightforward because the transport of ions is dominated by the morphology of the planet's magnetic field.

The combination of modern ground-based observing tools coupled with the first orbital observations have markedly increased our understanding of Mercury's exospheric composition and structure relative to the flyby observations made by Mariner 10, which detected only those species delivered to the planet by the solar wind. Advances in ground-based observing techniques, particularly improvements in spatial resolution, which is currently limited by atmospheric seeing, will certainly provide additional insights into the workings of the system. The next breakthrough will occur when the BepiColombo Mercury Planetary Orbiter and Mercury Magnetospheric Orbiter spacecraft (Benkhoff et al., 2010, Chapter 20) are inserted into orbit around the planet, an event currently scheduled for 2025. On those spacecraft will be a number of instruments designed to make detailed studies of the exosphere. These include the following investigations:

- Probing of Hermean Exosphere by Ultraviolet Spectroscopy (PHEBUS), an ultraviolet spectrometer covering the wavelength range 55–315 nm;
- Search for Exosphere Refilling and Emitted Neutral Abundances (SERENA), a suite of in situ neutral and ionized particle detectors;
- Mercury Sodium Atmospheric Spectral Imager (MSASI), a Fabry–Perot imaging system designed to produce full-disk images of the sodium exosphere;
- Mercury Dust Monitor (MDM), which will provide measurements of dust impacts to the planet's surface; and
- Mercury Plasma Particle Experiment (MPPE), which will provide measurements of exospheric ions.

BepiColombo will provide the first near-global high-resolution images of Mercury's sodium exosphere, a comprehensive inventory of exospheric species (both ionized and neutral), and key measurements of the inputs to Mercury's surface from the space environment. These observations will substantially advance our understanding of Mercury's coupled surface–exosphere–space environment system.

REFERENCES

Anderson, B. J., Acuña, M. H., Lohr, D. A., Scheifele, J., Raval, A., Korth, H. and Slavin, J. A. (2007). The Magnetometer instrument on MESSENGER. *Space Sci. Rev.*, **131**, 417–450, doi:10.1007/s11214-007-9246-7.

Anderson, B. J., Johnson, C. L., Korth, H., Purucker, M. E., Winslow, R. M., Slavin, J. A., Solomon, S. C., McNutt, R. L., Jr., Raines, J. M. and Zurbuchen, T. H. (2011). The global magnetic field of Mercury from MESSENGER orbital observations. *Science*, **333**, 1859–1862, doi:10.1126/science.1211001.

Andrews, G. B., Zurbuchen, T. H., Mauk, B. H., Malcom, H., Fisk, L. A., Gloeckler, G., Ho, G. C., Kelley, J. S., Koehn, P. L., Lefevere, T. W., Livi, S. S., Lundgren, R. A. and Raines, J. M. (2007). The Energetic Particle and Plasma Spectrometer instrument on the MESSENGER spacecraft. *Space Sci. Rev.*, **131**, 523–556, doi:10.1007/s11214-007-9272-5.

Baker, D. N., Poh, G., Odstrcil, D., Arge, C. N., Benna, M., Johnson, C. L., Korth, H., Gershman, D. J., Ho, G. C., McClintock, W. E., Cassidy, T. A., Merkel, A., Raines, J. M., Schriver, D., Slavin, J. A., Solomon, S. C., Travnicek, P. M., Winslow, R. M. and

Zurbuchen, T. H. (2013). Solar wind forcing at Mercury: WSA-ENLIL model results. *J. Geophys. Res. Space Physics*, **118**, 45–57, doi:10.1029/2012JA018064.

Baumgardner, J., Wilson, J. K. and Mendillo, M. (2008). Imaging the sources and full extent of the sodium tail of the planet Mercury. *Geophys. Res. Lett.*, **35**, L03201, doi:10.1029/2007GL032337.

Benkhoff, J., van Casteren, J., Hayakawa, H., Fujimoto, M., Laakso, H., Novara, M., Ferri, P., Middleton, H. R. and Ziethe, R. (2010). BepiColombo – Comprehensive exploration of Mercury: Mission overview and science goals. *Planet. Space Sci.*, **58**, 2–20, doi:10.1016/j.pss.2009.09.020.

Bida, T. A. and Killen, R. M. (2011). Observations of Al, Fe, and Ca⁺ in Mercury's exosphere. *EPSC-DPS Joint Meeting Abstracts and Program*, **6**, abstract EPSC-DPS2011-1621. European Planetary Science Congress – Division for Planetary Sciences Joint Meeting, Nantes, France, 2–7 October. Available at http://adsabs.harvard.edu/abs/2011epsc.conf.1621B.

Bida, T. A. and Killen, R. M. (2016). Observations of the minor species Al, Fe, and Ca⁺ in Mercury's exosphere. *Icarus*, **268**, 32–36, doi:10.1016/j.icarus.2016.10.019.

Bida, T. A., Killen, R. M. and Morgan, T. H. (2000). Discovery of calcium in Mercury's atmosphere. *Nature*, **404**, 159–161, doi:10.1038/35004521.

Bishop, J. and Chamberlain, J. W. (1989). Radiation pressure dynamics in planetary exospheres: A "natural" framework. *Icarus*, **81**, 145–163, doi:10.1016/0019-1035(89)90131-0.

Borin, P., Bruno, M., Cremonese, G. and Marzari, F. (2010). Estimate of the neutral atoms' contribution to the Mercury exosphere caused by a new flux of micrometeoroids. *Astron. Astrophys.*, **517**, A89, doi:10.1051/0004-6361/201014312.

Borland, D. and Taylor, R. M. (2007). Rainbow color map (still) considered harmful. *IEEE Comput. Graph. Appl.*, **27**, 14–17.

Broadfoot, A. L., Kumar, S., Belton, M. J. S. and McElroy, M. B. (1974). Mercury's atmosphere from Mariner 10: Preliminary results. *Science*, **185**, 166–169, doi:10.1126/science.185.4146.166.

Broadfoot, A. L., Shemansky, D. E. and Kumar, S. (1976). Mariner 10: Mercury atmosphere. *Geophys. Res. Lett.*, **3**, 577–580, doi:10.1029/GL003i010p00577.

Burger, M. H., Killen, R. M., Yervack, R. J., Jr., Bradley, E. T., McClintock, W. E., Sarantos, M., Benna, M. and Mouawad, N. (2010). Monte Carlo modeling of sodium in Mercury's exosphere during the first two MESSENGER flybys. *Icarus*, **209**, 63–74, doi:10.1016/j.icarus.2010.05.007.

Burger, M. H., Killen, R. M., McClintock, W. E., Vervack, R. J., Jr., Merkel, A. W., Sprague, A. L. and Sarantos, M. (2012). Modeling MESSENGER observations of calcium in Mercury's exosphere. *J. Geophys. Res.*, **117**, E00L11, doi:10.1029/2012JE004158.

Burger, M. H., Killen, R. M., McClintock, W. E., Merkel, A. W., Vervack, R. J., Cassidy, T. A. and Sarantos, M. (2014). Seasonal variations in Mercury's dayside calcium exosphere. *Icarus*, **238**, 51–58, doi:10.1016/j.icarus.2014.04.049.

Cassidy, T. A., Merkel, A. W., Burger, M. H., Sarantos, M., Killen, R. M., McClintock, W. E. and Vervack, R. J., Jr. (2015). Mercury's seasonal sodium exosphere: MESSENGER orbital observations. *Icarus*, **248**, 547–559, doi:10.1016/j.icarus.2014.10.037.

Cassidy, T. A., McClintock, W. E., Killen, R. M., Sarantos, M., Merkel, A. W., Vervack, R. J., Jr. and Burger, M. H. (2016). A cold-pole enhancement in Mercury's sodium exosphere. *Geophys. Res. Lett.*, **43**, 11,121–11,128, doi:10.1002/2016GL071071.

Chamberlain, J. W. (1961). *Physics of the Aurora and Airglow*. New York: Academic Press. Available at: http://onlinelibrary.wiley.com/doi/10.1002/9781118668047.fmatter/summary.

Chamberlain, J. W. (1963). Planetary coronae and atmospheric evaporation. *Planet. Space Sci.*, **11**, 901–960, doi:10.1016/0032-0633(63)90122-3.

Chamberlain, J. W. and Hunten, D. M. (1987). *Theory of Planetary Atmospheres. An Introduction to Their Physics and Chemistry*. International Geophysics Series, Vol. 36. Orlando, FL: Academic Press.

Christou, A. A., Killen, R. M. and Burger, M. H. (2015). The meteoroid stream of comet Encke at Mercury: Implications for MErcury Surface, Space ENvironment, GEochemistry, and Ranging observations of the exosphere. *Geophys. Res. Lett.*, **42**, 7311–7318, doi:10.1002/2015GL065361.

DiBraccio, G. A., Slavin, J. A., Boardsen, S. A., Anderson, B. J., Korth, H., Zurbuchen, T. H., Raines, J. M., Baker, D. N., McNutt, R. L., Jr. and Solomon, S. C. (2013). MESSENGER observations of magnetopause structure and dynamics at Mercury. *J. Geophys. Res. Space Physics*, **118**, 997–1008, doi:10.1002/jgra.50123.

Domingue, D. L., Koehn, P. L., Killen, R. M., Sprague, A. L., Sarantos, M., Cheng, A. F., Bradley, E. T. and McClintock, W. E. (2007). Mercury's atmosphere: A surface-bounded exosphere. *Space Sci. Rev.*, **131**, 161–186, doi:10.1007/s11214-007-9260-9.

Doressoundiram, A., Leblanc, F., Foellmi, C. and Erard, S. (2009). Metallic species in Mercury's exosphere: EMMI/New Technology Telescope observations. *Astron. J.*, **137**, 3859–3863, doi:10.1088/0004-6256/137/4/3859.

Doressoundiram, A., Leblanc, F., Foellmi, C., Gicquel, A., Cremonese, G., Donati, J.-F. and Veillet, C. (2010). Spatial variations of the sodium/potassium ratio in Mercury's exosphere uncovered by high-resolution spectroscopy. *Icarus*, **207**, 1–8, doi:10.1016/j.icarus.2009.11.020.

Evans, L. G., Peplowski, P. N., Rhodes, E. A., Lawrence, D. J., McCoy, T. J., Nittler, L. R., Solomon, S. C., Sprague, A. L., Stockstill-Cahill, K. R., Starr, R. D., Weider, S. Z., Boynton, W. V., Hamara, D. K. and Goldsten, J. O. (2012). Major-element abundances on the surface of Mercury: Results from the MESSENGER Gamma-Ray Spectrometer. *J. Geophys. Res.*, **117**, E00L07, doi:10.1029/2012JE004178.

Fink, U., Larson, H. P. and Poppen, R. F. (1974). A new upper limit for an atmosphere of CO₂, CO on Mercury. *Astrophys. J.*, **187**, 407–416, doi:10.1086/152647.

Gershman, D. J., Slavin, J. A., Raines, J. M., Zurbuchen, T. H., Anderson, B. J., Korth, H., Baker, D. N. and Solomon, S. C. (2014). Ion kinetic properties in Mercury's pre-midnight plasma sheet. *Geophys. Res. Lett.*, **41**, 5740–5747, doi:10.1002/2014GL060468.

Huebner, W. F. and Mukherjee, J. (2015). Photoionization and photodissociation rates in solar and blackbody radiation fields. *Planet. Space Sci.*, **106**, 11–45, doi:10.1016/j.pss.2014.11.022.

Hunten, D. M., Roach, F. E. and Chamberlain, J. W. (1956). A photometric unit for the airglow and aurora. *J. Atmos. Terr. Phys.*, **8**, 345–346.

Hunten, D. M., Shemansky, D. E. and Morgan, T. H. (1988). The Mercury atmosphere. In *Mercury*, ed. F. Vilas, C. R. Chapman and M. S. Matthews. Tucson, AZ: University of Arizona Press, pp. 562–612.

Ip, W. H. (1986). The sodium exosphere and magnetosphere of Mercury. *Geophys. Res. Lett.*, **13**, 423–426, doi:10.1029/GL013i005p00423.

Johnson, R. E., Leblanc, F., Yakshinskiy, B. V. and Madey, T. E. (2002). Energy distributions for desorption of sodium and potassium from ice: The Na/K ratio at Europa. *Icarus*, **156**, 136–142, doi:10.1006/icar.2001.6763.

Killen, R. M. (2006). Curve-of-growth model for sodium D2 emission at Mercury. *Publ. Astron. Soc. Pac.*, **118**, 1344–1350, doi:10.1086/508070.

Killen, R. M. (2016). Pathways for energization of Ca in Mercury's exosphere. *Icarus*, **268**, 32–36, doi:10.1016/j.icarus.2015.12.035.

Killen, R. M. and Hahn, J. M. (2015). Impact vaporization as a possible source of Mercury's calcium exosphere. *Icarus*, **250**, 230–237, doi:10.1016/j.icarus.2014.11.035.

Killen, R. M., Potter, A., Fitzsimmons, A. and Morgan, T. H. (1999). Sodium D2 line profiles: Clues to the temperature structure of Mercury's exosphere. *Planet. Space Sci.*, **47**, 1449–1458, doi:10.1016/S0032-0633(99)00071–9.

Killen, R. M., Sarantos, M., Potter, A. E. and Reiff, P. (2004). Source rates and ion recycling rates for Na and K in Mercury's atmosphere. *Icarus*, **171**, 1–19, doi:10.1016/j.icarus.2004.04.007.

Killen, R. M., Bida, T. A. and Morgan, T. H. (2005). The calcium exosphere of Mercury. *Icarus*, **173**, 300–311, doi:10.1016/j.icarus.2004.08.022.

Killen, R., Cremonese, G., Lammer, H., Orsini, S., Potter, A. E., Sprague, A. L., Wurz, P., Khodachenko, M. L., Lichtenegger, H. I. M., Milillo, A. and Mura, A. (2007). Processes that promote and deplete the exosphere of Mercury. *Space Sci. Rev.*, **132**, 433–509, doi:10.1007/s11214-007-9232-0.

Killen, R. M., Mouawad, N. and Shemansky, D. E. (2009). Expected emission from Mercury's exospheric species, and their ultraviolet-visible signatures. *Astrophys. J. Suppl. Ser.*, **181**, 351–359.

Killen, R. M., Potter, A. E., Vervack, R. J., Bradley, E. T., McClintock, W. E., Anderson, C. M. and Burger, M. H. (2010). Observations of metallic species in Mercury's exosphere. *Icarus*, **209**, 75–87, doi:10.1016/j.icarus.2010.02.018.

Leblanc, F. and Johnson, R. E. (2003). Mercury's sodium exosphere. *Icarus*, **164**, 261–281, doi:10.1016/S0019-1035(03)00147–7.

Leblanc, F. and Johnson, R. E. (2010). Mercury exosphere I. Global circulation model of its sodium component. *Icarus*, **209**, 280–300, doi:10.1016/j.icarus.2010.04.020.

Leblanc, F., Barbieri, C., Cremonese, G., Verani, S., Cosentino, R., Mendillo, M., Sprague, A. and Hunten, D. (2006). Observations of Mercury's exosphere: Spatial distributions and variations of its Na component during August 8, 9 and 10, 2003. *Icarus*, **185**, 395–402, doi:10.1016/j.icarus.2006.08.006.

Leblanc, F., Doressoundiram, A., Schneider, N., Mangano, V., López Ariste, A., Lemen, C., Gelly, B., Barbieri, C. and Cremonese, G. (2008). High latitude peaks in Mercury's sodium exosphere: Spectral signature using THEMIS solar telescope. *Geophys. Res. Lett.*, **35**, L18204, doi:10.1029/2008GL035322.

Leblanc, F., Doressoundiram, A., Schneider, N. M., Massetti, S., Wedlund, M., Lopez Ariste, A., Barbieri, C., Mangano, V. and Cremonese, G. (2009). Short-term variations of Mercury's Na exosphere observed with very high spectral resolution. *Geophys. Res. Lett.*, **36**, L07201, doi:10.1029/2009GL038089.

Leblanc, F., Chaufray, J. Y., Doressoundiram, A., Berthelier, J. J., Mangano, V., Lopez-Ariste, A. and Borin, P. (2013). Mercury exosphere. III: Energetic characterization of its sodium component. *Icarus*, **223**, 963–974, doi:10.1016/j.icarus.2012.08.025.

Mangano, V., Leblanc, F., Barbieri, C., Massetti, S., Milillo, A., Cremonese, G. and Grava, C. (2009). Detection of a southern peak in Mercury's sodium exosphere with the TNG in 2005. *Icarus*, **201**, 424–431, doi:10.1016/j.icarus.2009.01.016.

Mangano, V., Massetti, S., Milillo, A., Mura, A., Orsini, S. and Leblanc, F. (2013). Dynamical evolution of sodium anisotropies in the exosphere of Mercury. *Planet. Space Sci.*, **82–83**, 1–10, doi:10.1016/j.pss.2013.03.002.

Mangano, V., Massetti, S., Milillo, A., Plainaki, C., Orsini, S., Rispoli, R. and Leblanc, F. (2015). THEMIS Na exosphere observations of Mercury and their correlation with in-situ magnetic field measurements by MESSENGER. *Planet. Space Sci.*, **115**, 102–109, doi:10.1016/j.pss.2015.04.001.

McClintock, W. E. and Lankton, M. R. (2007). The Mercury Atmospheric and Surface Composition Spectrometer for the MESSENGER mission. *Space Sci. Rev.*, **131**, 481–521, doi:10.1007/s11214-007-9264-5.

McClintock, W. E., Bradley, E. T., Vervack, R. J., Jr., Killen, R. M., Sprague, A. L., Izenberg, N. R. and Solomon, S. C. (2008). Mercury's exosphere: Observations during MESSENGER's first Mercury flyby. *Science*, **321**, 92–94.

McClintock, W. E., Vervack, R. J., Bradley, E. T., Killen, R. M., Mouawad, N., Sprague, A. L., Burger, M. H., Solomon, S. C. and Izenberg, N. R. (2009). MESSENGER observations of Mercury's exosphere: Detection of magnesium and distribution of constituents. *Science*, **324**, 610–613, doi:10.1126/science.1172525.

McGrath, M. A., Johnson, R. E. and Lanzerotti, L. J. (1986). Sputtering of sodium on the planet Mercury. *Nature*, **323**, 694–696, doi:10.1038/323694a0.

Merkel, A. W., Cassidy, T. A., Vervack, R. J., McClintock, W. E., Sarantos, M., Burger, M. H. and Killen, R. M. (2017). Seasonal variations of Mercury's magnesium dayside exosphere from MESSENGER observations. *Icarus*, **281**, 46–54, doi:10.1016/j.icarus.2016.08.032.

Merkel, A. W., Vervack, R. J., Jr., Killen, R. M., Cassidy, T. A., McClintock, W. E., Nittler, L. R. and Burger, M. H. (2018). Evidence connecting Mercury's magnesium exosphere to its magnesium-rich surface terrane. *Geophys. Res. Lett.*, **45**, 6790-6797 doi:10.1029/2018GL078407.

Morgan, T. H., Zook, H. A. and Potter, A. E. (1988). Impact-driven supply of sodium and potassium to the atmosphere of Mercury. *Icarus*, **75**, 156–170, doi:10.1016/0019–1035(88)90134–0.

Mouawad, N., Burger, M. H., Killen, R. M., Potter, A. E., McClintock, W. E., Vervack, R. J., Jr., Bradley, E. T., Benna, M. and Naidu, S. (2011). Constraints on Mercury's Na exosphere: Combined MESSENGER and ground-based data. *Icarus*, **211**, 21–36, doi:10.1016/j.icarus.2010.10.019.

Mura, A., Wurz, P., Lichtenegger, H. I. M., Schleicher, H., Lammer, H., Delcourt, D., Milillo, A., Orsini, S., Massetti, S. and Khodachenko, M. L. (2009). The sodium exosphere of Mercury: Comparison between observations during Mercury's transit and model results. *Icarus*, **200**, 1–11, doi:10.1016/j.icarus.2008.11.014.

Nittler, L. R., Starr, R. D., Weider, S. Z., McCoy, T. J., Boynton, W. V., Ebel, D. S., Ernst, C. M., Evans, L. G., Goldsten, J. O., Hamara, D. K., Lawrence, D. J., McNutt, R. L., Schlemm, C. E., Solomon, S. C. and Sprague, A. L. (2011). The major-element composition of Mercury's surface from MESSENGER X-ray spectrometry. *Science*, **333**, 1847–1850, doi:10.1126/science.1211567.

Peplowski, P. N., Evans, L. G., Stockstill-Cahill, K. R., Lawrence, D. J., Goldsten, J. O., McCoy, T. J., Nittler, L. R., Solomon, S. C., Sprague, A. L., Starr, R. D. and Weider, S. Z. (2014). Enhanced sodium abundance in Mercury's north polar region revealed by the MESSENGER Gamma-Ray Spectrometer. *Icarus*, **228**, 86–95.

Pierce, A. K. (1965). Construction of a Bowen image slicer. *Publ. Astron. Soc. Pac.*, **77**, 216–217, doi:10.1086/128199.

Potter, A. E. (1995). Chemical sputtering could produce sodium vapor and ice on Mercury. *Geophys. Res. Lett.*, **22**, 3289–3292, doi:10.1029/95GL03181.

Potter, A. E. and Killen, R. M. (2008). Observations of the sodium tail of Mercury. *Icarus*, **194**, 1–12, doi:10.1016/j.icarus.2007.09.023.

Potter, A. E. and Morgan, T. H. (1985). Discovery of sodium in the atmosphere of Mercury. *Science*, **229**, 651–653, doi:10.1126/science.229.4714.651.

Potter, A. E. and Morgan, T. H. (1986). Potassium in the atmosphere of Mercury. *Icarus*, **67**, 336–340, doi:10.1016/0019–1035(86)90113–2.

Potter, A. E. and Morgan, T. H. (1990). Evidence for magnetospheric effects on the sodium atmosphere of Mercury. *Science*, **248**, 835–838, doi:10.1126/science.248.4957.835.

Potter, A. E., Killen, R. M. and Morgan, T. H. (1999). Rapid changes in the sodium exosphere of Mercury. *Planet. Space Sci.*, **47**, 1441–1448, doi:10.1016/S0032-0633(99)00070-7.

Potter, A. E., Killen, R. M. and Morgan, T. H. (2002a). The sodium tail of Mercury. *Meteorit. Planet. Sci.*, **37**, 1165–1172, doi:10.1111/j.1945-5100.2002.tb00886.x.

Potter, A. E., Anderson, C. M., Killen, R. M. and Morgan, T. H. (2002b). Ratio of sodium to potassium in the Mercury exosphere. *J. Geophys. Res.*, **107**, 5040, doi:10.1029/2000JE001493.

Potter, A. E., Killen, R. M. and Sarantos, M. (2006). Spatial distribution of sodium on Mercury. *Icarus*, **181**, 1–12, doi:10.1016/j.icarus.2005.10.026.

Potter, A. E., Morgan, T. H. and Killen, R. M. (2009). Sodium winds on Mercury. *Icarus*, **204**, 355–367, doi:10.1016/j.icarus.2009.06.028.

Potter, A. E., Killen, R. M., Reardon, K. P. and Bida, T. A. (2013). Observation of neutral sodium above Mercury during the transit of November 8, 2006. *Icarus*, **226**, 172–185, doi:10.1016/j.icarus.2013.05.029.

Raines, J. M., Gershman, D. J., Zurbuchen, T. H., Sarantos, M., Slavin, J. A., Gilbert, J. A., Korth, H., Anderson, B. J., Gloeckler, G., Krimigis, S. M., Baker, D. N., McNutt, R. L. and Solomon, S. C. (2013). Distribution and compositional variations of plasma ions in Mercury's space environment: The first three Mercury years of MESSENGER observations. *J. Geophys. Res. Space Physics*, **118**, 1604–1619, doi:10.1029/2012JA018073.

Sarantos, M., Killen, R. M., Sharma, A. S. and Slavin, J. A. (2008). Influence of plasma ions on source rates for the lunar exosphere during passage through the Earth's magnetosphere. *Geophys. Res. Lett.*, **35**, L04105, doi:10.1029/2007GL032310.

Sarantos, M., Killen, R. M., McClintock, W. E., Todd Bradley, E., Vervack, R. J., Benna, M. and Slavin, J. A. (2011). Limits to Mercury's magnesium exosphere from MESSENGER second flyby observations. *Planet. Space Sci.*, **59**, 1992–2003, doi:10.1016/j.pss.2011.05.002.

Schleicher, H., Wiedemann, G., Wohl, H., Berkefeld, T. and Soltau, D. (2004). Detection of neutral sodium above Mercury during the transit on 2003 May 7. *Astron. Astrophys.*, **425**, 1119–1124, doi:10.1051/0004–6361:20040477.

Schmidt, C. A. (2013). Monte Carlo modeling of north–south asymmetries in Mercury's sodium exosphere. *J. Geophys. Res. Space Physics*, **118**, 4564–4571, doi:10.1002/jgra.50396.

Schmidt, C. A., Wilson, J. K., Baumgardner, J. and Mendillo, M. (2010). Orbital effects on Mercury's escaping sodium exosphere. *Icarus*, **207**, 9–16, doi:10.1016/j.icarus.2009.10.017.

Schmidt, C. A., Baumgardner, J., Mendillo, M. and Wilson, J. K. (2012). Escape rates and variability constraints for high-energy sodium sources at Mercury. *J. Geophys. Res.*, **117**, A03301, doi:10.1029/2011JA017217.

Shemansky, D. E. and Broadfoot, A. L. (1977). Interaction of the surfaces of the moon and Mercury with their exospheric atmospheres. *Rev. Geophys. Space Phys.*, **15**, 491–499, doi:10.1029/RG015i004p00491.

Slavin, J. A., DiBraccio, G. A., Gershman, D. J., Imber, S. M., Poh, G. K., Raines, J. M., Zurbuchen, T. H., Jia, X., Baker, D. N., Glassmeier, K.-H., Livi, S. A., Boardsen, S. A., Cassidy, T. A., Sarantos, M., Sundberg, T., Masters, A., Johnson, C. L., Winslow, R. M., Anderson, B. J., Korth, H., McNutt, R. L. and Solomon, S. C. (2014). MESSENGER observations of Mercury's dayside magnetosphere under extreme solar wind conditions. *J. Geophys. Res. Space Physics*, **119**, 8087–8116, doi:10.1002/2014JA020319.

Smith, G. R., Shemansky, D. E., Broadfoot, A. L. and Wallace, L. (1978). Monte Carlo modeling of exospheric bodies: Mercury. *J. Geophys. Res.*, **83**, 3783–3790, doi:10.1029/JA083iA08p03783.

Smyth, W. H. (1986). Nature and variability of Mercury's sodium atmosphere. *Nature*, **323**, 696–699, doi:10.1038/323696a0.

Smyth, W. H. and Marconi, M. L. (1995). Theoretical overview and modeling of the sodium and potassium atmospheres of Mercury. *Astrophys. J.*, **441**, 839–864, doi:10.1086/175407.

Sprague, A. L., Kozlowski, R. W. H., Hunten, D. M., Schneider, N. M., Domingue, D. L., Wells, W. K., Schmitt, W. and Fink, U. (1997). Distribution and abundance of sodium in Mercury's atmosphere, 1985–1988. *Icarus*, **129**, 506–527, doi:10.1006/icar.1997.5784.

Vervack, R. J., Jr., McClintock, W. E., Bradley, E. T., Killen, R. M., Sprague, A. L., Mouawad, N., Izenberg, N. R., Kochte, M. C. and Lankton, M. R. (2009). MESSENGER observations of Mercury's exosphere: Discoveries and surprises from the first two flybys. *Lunar Planet. Sci.*, **40**, abstract 2220.

Vervack, R. J., Jr., McClintock, W. E., Killen, R. M., Sprague, A. L., Anderson, B. J., Burger, M. H., Bradley, E. T., Mouawad, N., Solomon, S. C. and Izenberg, N. R. (2010). Mercury's complex exosphere: Results from MESSENGER's third flyby. *Science*, **329**, 672–675, doi:10.1126/science.1188572.

Vervack, R. J., Jr., Killen, R. M., Sprague, A. L., Burger, M. H., Merkel, A. W. and Sarantos, M. (2011). Early MESSENGER results for less abundant or weakly emitting species in Mercury's exosphere. *EPSC-DPS Joint Meeting Abstracts and Program*, **6**, abstract EPSC-DPS2011-1131. European Planetary Science Congress – Division for Planetary Sciences Joint Meeting, Nantes, France, 2–7 October. Available at http://adsabs.harvard.edu/abs/2011epsc.conf.1131V.

Vervack, R. J., Jr., Killen, R. M., McClintock, W. E., Merkel, A. W., Burger, M. H., Cassidy, T. A. and Sarantos, M. (2016). New discoveries from MESSENGER and insights into Mercury's exosphere. *Geophys. Res. Lett.*, **43**, 11,545–11,551, doi:10.1002/2016GL071284.

Winslow, R. M., Johnson, C. L., Anderson, B. J., Korth, H., Slavin, J. A., Purucker, M. E. and Solomon, S. C. (2012). Observations of Mercury's northern cusp region with MESSENGER's Magnetometer. *Geophys. Res. Lett.*, **39**, L08112, doi:10.1029/2012GL051472.

Winslow, R. M., Johnson, C. L., Anderson, B. J., Gershman, D. J., Raines, J. M., Lillis, R. J., Korth, H., Slavin, J. A., Solomon, S. C., Zurbuchen, T. H. and Zuber, M. T. (2014). Mercury's surface magnetic field determined from proton-reflection magnetometry. *Geophys. Res. Lett.*, **41**, 4463–4470, doi:10.1002/2014GL060258.

Yakshinskiy, B. V. and Madey, T. E. (2005). Temperature-dependent DIET of alkalis from SiO_2 films: Comparison with a lunar sample. *Surf. Sci.*, **593**, 202–209, doi:10.1016/j.susc.2005.06.062.

Yan, N., Chassefire, E., Leblanc, F. and Sarkissian, A. (2006). Thermal model of Mercury's surface and subsurface: Impact of subsurface physical heterogeneities on the surface temperature. *Adv. Space Res.*, **38**, 583–588, doi:10.1016/j.asr.2005.11.010.

Yoshikawa, I., Ono, J., Yoshioka, K., Murakami, G., Ezawa, F., Kameda, S. and Ueno, S. (2008). Observation of Mercury's sodium exosphere during the transit on November 9, 2006. *Planet. Space Sci.*, **56**, 1676–1680.

Potter, A. E. and Morgan, T. H. (1990). Evidence for magnetospheric effects on the sodium atmosphere of Mercury. *Science*, **248**, 835–838, doi:10.1126/science.248.4957.835.

Potter, A. E., Killen, R. M. and Morgan, T. H. (1999). Rapid changes in the sodium exosphere of Mercury. *Planet. Space Sci.*, **47**, 1441–1448, doi:10.1016/S0032-0633(99)00070-7.

Potter, A. E., Killen, R. M. and Morgan, T. H. (2002a). The sodium tail of Mercury. *Meteorit. Planet. Sci.*, **37**, 1165–1172, doi:10.1111/j.1945-5100.2002.tb00886.x.

Potter, A. E., Anderson, C. M., Killen, R. M. and Morgan, T. H. (2002b). Ratio of sodium to potassium in the Mercury exosphere. *J. Geophys. Res.*, **107**, 5040, doi:10.1029/2000JE001493.

Potter, A. E., Killen, R. M. and Sarantos, M. (2006). Spatial distribution of sodium on Mercury. *Icarus*, **181**, 1–12, doi:10.1016/j.icarus.2005.10.026.

Potter, A. E., Morgan, T. H. and Killen, R. M. (2009). Sodium winds on Mercury. *Icarus*, **204**, 355–367, doi:10.1016/j.icarus.2009.06.028.

Potter, A. E., Killen, R. M., Reardon, K. P. and Bida, T. A. (2013). Observation of neutral sodium above Mercury during the transit of November 8, 2006. *Icarus*, **226**, 172–185, doi:10.1016/j.icarus.2013.05.029.

Raines, J. M., Gershman, D. J., Zurbuchen, T. H., Sarantos, M., Slavin, J. A., Gilbert, J. A., Korth, H., Anderson, B. J., Gloeckler, G., Krimigis, S. M., Baker, D. N., McNutt, R. L. and Solomon, S. C. (2013). Distribution and compositional variations of plasma ions in Mercury's space environment: The first three Mercury years of MESSENGER observations. *J. Geophys. Res. Space Physics*, **118**, 1604–1619, doi:10.1029/2012JA018073.

Sarantos, M., Killen, R. M., Sharma, A. S. and Slavin, J. A. (2008). Influence of plasma ions on source rates for the lunar exosphere during passage through the Earth's magnetosphere. *Geophys. Res. Lett.*, **35**, L04105, doi:10.1029/2007GL032310.

Sarantos, M., Killen, R. M., McClintock, W. E., Todd Bradley, E., Vervack, R. J., Benna, M. and Slavin, J. A. (2011). Limits to Mercury's magnesium exosphere from MESSENGER second flyby observations. *Planet. Space Sci.*, **59**, 1992–2003, doi:10.1016/j.pss.2011.05.002.

Schleicher, H., Wiedemann, G., Wöhl, H., Berkefeld, T. and Soltau, D. (2004). Detection of neutral sodium above Mercury during the transit on 2003 May 7. *Astron. Astrophys.*, **425**, 1119–1124, doi:10.1051/0004-6361:20040477.

Schmidt, C. A. (2013). Monte Carlo modeling of north–south asymmetries in Mercury's sodium exosphere. *J. Geophys. Res. Space Physics*, **118**, 4564–4571, doi:10.1002/jgra.50396.

Schmidt, C. A., Wilson, J. K., Baumgardner, J. and Mendillo, M. (2010). Orbital effects on Mercury's escaping sodium exosphere. *Icarus*, **207**, 9–16, doi:10.1016/j.icarus.2009.10.017.

Schmidt, C. A., Baumgardner, J., Mendillo, M. and Wilson, J. K. (2012). Escape rates and variability constraints for high-energy sodium sources at Mercury. *J. Geophys. Res.*, **117**, A03301, doi:10.1029/2011JA017217.

Shemansky, D. E. and Broadfoot, A. L. (1977). Interaction of the surfaces of the moon and Mercury with their exospheric atmospheres. *Rev. Geophys. Space Phys.*, **15**, 491–499, doi:10.1029/RG015i004p00491.

Slavin, J. A., DiBraccio, G. A., Gershman, D. J., Imber, S. M., Poh, G. K., Raines, J. M., Zurbuchen, T. H., Jia, X., Baker, D. N., Glassmeier, K.-H., Livi, S. A., Boardsen, S. A., Cassidy, T. A., Sarantos, M., Sundberg, T., Masters, A., Johnson, C. L., Winslow, R. M., Anderson, B. J., Korth, H., McNutt, R. L. and Solomon, S. C. (2014). MESSENGER observations of Mercury's dayside magnetosphere under extreme solar wind conditions. *J. Geophys. Res. Space Physics*, **119**, 8087–8116, doi:10.1002/2014JA020319.

Smith, G. R., Shemansky, D. E., Broadfoot, A. L. and Wallace, L. (1978). Monte Carlo modeling of exospheric bodies: Mercury. *J. Geophys. Res.*, **83**, 3783–3790, doi:10.1029/JA083iA08p03783.

Smyth, W. H. (1986). Nature and variability of Mercury's sodium atmosphere. *Nature*, **323**, 696–699, doi:10.1038/323696a0.

Smyth, W. H. and Marconi, M. L. (1995). Theoretical overview and modeling of the sodium and potassium atmospheres of Mercury. *Astrophys. J.*, **441**, 839–864, doi:10.1086/175407.

Sprague, A. L., Kozlowski, R. W. H., Hunten, D. M., Schneider, N. M., Domingue, D. L., Wells, W. K., Schmitt, W. and Fink, U. (1997). Distribution and abundance of sodium in Mercury's atmosphere, 1985–1988. *Icarus*, **129**, 506–527, doi:10.1006/icar.1997.5784.

Vervack, R. J., Jr., McClintock, W. E., Bradley, E. T., Killen, R. M., Sprague, A. L., Mouawad, N., Izenberg, N. R., Kochte, M. C. and Lankton, M. R. (2009). MESSENGER observations of Mercury's exosphere: Discoveries and surprises from the first two flybys. *Lunar Planet. Sci.*, **40**, abstract 2220.

Vervack, R. J., Jr., McClintock, W. E., Killen, R. M., Sprague, A. L., Anderson, B. J., Burger, M. H., Bradley, E. T., Mouawad, N., Solomon, S. C. and Izenberg, N. R. (2010). Mercury's complex exosphere: Results from MESSENGER's third flyby. *Science*, **329**, 672–675, doi:10.1126/science.1188572.

Vervack, R. J., Jr., Killen, R. M., Sprague, A. L., Burger, M. H., Merkel, A. W. and Sarantos, M. (2011). Early MESSENGER results for less abundant or weakly emitting species in Mercury's exosphere. *EPSC-DPS Joint Meeting Abstracts and Program*, **6**, abstract EPSC-DPS2011-1131. European Planetary Science Congress – Division for Planetary Sciences Joint Meeting, Nantes, France, 2–7 October. Available at http://adsabs.harvard.edu/abs/2011epsc.conf.1131V.

Vervack, R. J., Jr., Killen, R. M., McClintock, W. E., Merkel, A. W., Burger, M. H., Cassidy, T. A. and Sarantos, M. (2016). New discoveries from MESSENGER and insights into Mercury's exosphere. *Geophys. Res. Lett.*, **43**, 11,545–11,551, doi:10.1002/2016GL071284.

Winslow, R. M., Johnson, C. L., Anderson, B. J., Korth, H., Slavin, J. A., Purucker, M. E. and Solomon, S. C. (2012). Observations of Mercury's northern cusp region with MESSENGER's Magnetometer. *Geophys. Res. Lett.*, **39**, L08112, doi:10.1029/2012GL051472.

Winslow, R. M., Johnson, C. L., Anderson, B. J., Gershman, D. J., Raines, J. M., Lillis, R. J., Korth, H., Slavin, J. A., Solomon, S. C., Zurbuchen, T. H. and Zuber, M. T. (2014). Mercury's surface magnetic field determined from proton-reflection magnetometry. *Geophys. Res. Lett.*, **41**, 4463–4470, doi:10.1002/2014GL060258.

Yakshinskiy, B. V. and Madey, T. E. (2005). Temperature-dependent DIET of alkalis from SiO$_2$ films: Comparison with a lunar sample. *Surf. Sci.*, **593**, 202–209, doi:10.1016/j.susc.2005.06.062.

Yan, N., Chassefire, E., Leblanc, F. and Sarkissian, A. (2006). Thermal model of Mercury's surface and subsurface: Impact of subsurface physical heterogeneities on the surface temperature. *Adv. Space Res.*, **38**, 583–588, doi:10.1016/j.asr.2005.11.010.

Yoshikawa, I., Ono, J., Yoshioka, K., Murakami, G., Ezawa, F., Kameda, S. and Ueno, S. (2008). Observation of Mercury's sodium exosphere during the transit on November 9, 2006. *Planet. Space Sci.*, 56, 1676–1680.